Università degli Studi di Torino
Doctoral School of Sciences and Innovative Technologies
PhD Programme in Chemical and Material Sciences XXX Cycle

Semiconducting oxides modification for photocatalytic applications.

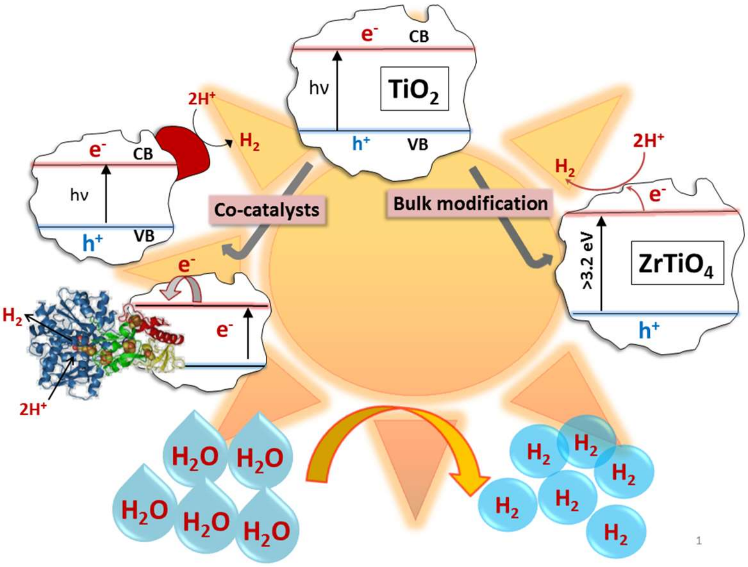

Valeria Polliotto

Supervisor:
Prof. Elio Giamello
Co-Supervisor:
Dr. Stefano Livraghi

Università degli Studi di Torino

Doctoral School of Sciences and Innovative Technologies

PhD Programme in Chemical and Material Sciences XXX cycle

Semiconducting oxides modification for photocatalytic applications.

Candidate: **Valeria Polliotto**

Supervisor: Prof. **Elio Giamello**

Co-Supervisor: Dr. **Stefano Livraghi**

Jury Members: Prof. **Adriana Zaleska-Medynska**
University of Gdansk
Faculty of Chemistry, Department of Environmental Technology

Prof. **Elena Selli**
Universita degli Studi di Milano
Dipartimento di Chimica

Prof. **Maria Cristina Paganini**
Universita degli Studi di Torino
Dipartimento di Chimica

Head of the Doctoral School: Prof. Massimo Maffei
PhD Programme Coordinator: Prof. Mario Chiesa

Torino, 2017

Index

Introduction

Materials and Methods

Results and discussion

Conclusions

Introduction

Introduction

The use of light in chemical process is one of the most important targets in the last decades. In particular, the interest in the use of sunlight for solar fuel production (hydrogen from water or CO_2 reduction), pollutants abatement and novel chemical synthesis is progressively increasing.

To this purpose the various strategies adopted are based on the use of semiconductors which are often modified in various ways to increase their photoactivity. Since 1972, with the discovery of the Honda-Fujishima effect, used for the photoassisted electrolysis of H_2O,[1] titanium dioxide, or titania, is one of the most employed semiconductors. Because of its high photocatalytic reactivity combined with chemical and thermal stability, non toxicity and cheapness,[2] TiO_2 became a system of reference in the area of photochemical and photo-electrochemical applications and is utilised, nowadays, in processes for pollutants abatement,[3] as biocide,[4-5] in odour control[6] and in self-cleaning of glasses or of external surfaces.[7]

Despite its strong advantages, titania shows some serious drawbacks: the first one is the large value of the band gap (around 3.2 eV for the anatase polymorph) that implicate the use of UV photons to perform the excitation of electrons from the valence band to the conduction band limiting therefore the use of sun light (poor of UV components at the earth surface) in photochemical applications of titanium dioxide.

The second drawback is the electrochemical potential of the conduction band electrons which is only slightly more negative than the H^+/H_2 potential thus limiting the reductive capability of photoexcited electrons (Figure 1).

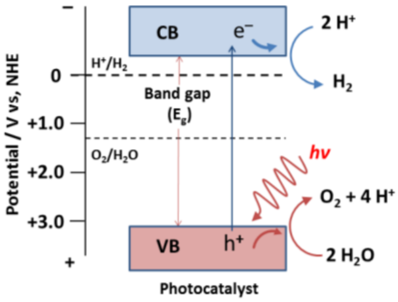

Figure 1. Schematic representation of the conduction and valence bands of titania in comparison with the H^+/H_2 and O_2/H_2O electrochemical potentials.

The need of overcoming these two serious constraints are at the origin of a long activity aiming either to modify the solid in order to improve its performances or to search for other semiconductors with new and different properties.

In the recent past, a lot of work has been done to overcome the first limit, in particular trying to adjust the photochemical properties of titania in order to extend to the visible range its optical absorption. The most successful approach, at least in the field of photovoltaic applications, consists in anchoring dye molecules on TiO_2 surface: the visible light excites the photo-sensitizer, which injects electrons into the TiO_2 conduction band. Ruthenium-based complexes are the most employed dyes in photovoltaic applications (Graetzel cells)[8] at least till the advent of the new systems based on complex perovskites (organometal halide).[9] A possible alternative, in particular for the area of photocatalysis, consists in the doping of the solid with various dopants. In fact, it has been shown that, in some case, the presence of alioelements defects in the lattice of the oxide generates intra band gap energetic levels capable to allow the excitation of the electrons of the valence band to the conduction band under visible light.[10-11] In the latter case the most interesting case is that of doping with non-metals. In particular doping with nitrogen[10,12-13] or with combination of elements including nitrogen[14-15] has been the object of intense research activity and of warmly debated results. As a matter of fact, nitrogen doped titania is now currently used in photocatalytic applications employing visible light.[16-17]

On the other hand, the modifications of TiO_2 to overcome the second drawback, concerning the electrochemical potential of the titania conduction band and, thus, the limit in the reductive potential of the oxide, are still less explored.

This PhD thesis falls within this latest research topic. In particular two approaches have been used for this purpose:

- Modifications of the TiO_2 matrix in order to modulate the band energies and, in particular, the reductive potential of the conduction band.
- Anchoring of co-catalysts on the titania surface in order to favor reductive reactions (i.e. H_2 evolution). In this case, besides the classic co-catalyst such as platinum, I have focused my attention on an alternative type of enzymatic co-catalyst, the [Fe-Fe] hydrogenase.[18]

  In addition to the use of co-catalyst I have investigated the effect of the deposition of different type of copper species on the oxide surface. This type of modification has been found to improve the Hydrogen Evolution Reaction (HER) activity. [19-24]

  The surface deposition of copper on TiO_2 has been recently described in the literature but the interaction mechanism between various components and the photochemistry of the whole system are still unclear.

Concerning the modifications of the TiO_2 matrix, the present project is focused on the investigation of the relatively unknown zirconium titanate $ZrTiO_4$, an oxide which is halfway between the parent oxides TiO_2 and ZrO_2. This material presents, indeed, a structure similar to that of titania polymorphs but it contains both titanium and zirconium tetravalent ions in equivalent amount. Moreover, like in the case of ZrO_2, this oxide exhibits the conduction band potential slightly higher than that of TiO_2

and it could, thus, have, in principle, superior reductive properties. However, because of its high band gap, the limits previously described for TiO_2 remain also in this case and the doping of the $ZrTiO_4$ with alioelements is mandatory in order to have photoactivity in the visible range.

The work illustrated in this thesis is not directly planned to obtain significant yields in H_2 production or in the photocatalytic reactions. Rather, the approach of my research group aims to explore new materials and, possibly, to individuate new ideas and concepts in the field.

The characterization of all systems studied in this thesis was performed mainly using the following techniques:

- X-Ray powder Diffraction (XRD) for the structural analysis of the oxides.
- UV-Vis Diffuse Reflectance Spectroscopy (DRS) to evaluate the optical absorption of the samples.
- Electron Paramagnetic Resonance spectroscopy (EPR) to characterize the defects in oxides, the photo-formation of charge carriers and their transfer.

The thesis is organized as follows: the first part is devoted to the presentation of the state of the art regarding the peculiar properties of TiO_2, ZrO_2 and mixed oxides. Furthermore literature data concerning the use of co-catalysts, especially a description of the [Fe-Fe] hydrogenase enzyme, will be provided. The second part is devoted to the experimental work; the employed methods are illustrated and then the results obtained for each system are presented and discussed.

Finally, the conclusions and the future perspectives are reported.

1. Oxide of the IV group elements.

1.1. Titanium oxide TiO_2.

1.1.1. Structure.

Titanium dioxide exists in three different polymorphs: anatase, rutile and brookite. Anatase and rutile exhibit tetragonal crystalline structures, brookite an orthorhombic one. The structures can be described in terms of TiO_6 octahedra connected by corner and edge sharing. All oxygen are surrounded by three Ti ions (OTi_3). The three polymorphs differ one from each other in the way the polyhedra are connected as shown in Figure 2.

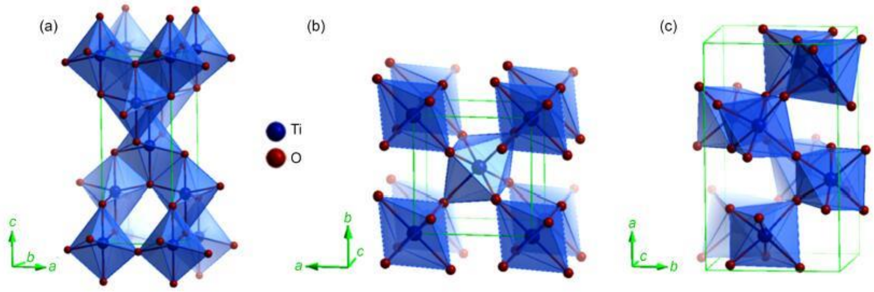

Figure 2. Crystallographic unit cells of a) anatase, b) rutile, c) brookite

The two main polymorphs, rutile and anatase, also differ for the more stable exposed crystal faces which are (110) in the case of rutile and (101) in the case of anatase. The relatively small difference between anatase and rutile however strongly influences their behavior. In particular rutile is the most thermodynamically stable polymorph, but anatase is most active in photocatalytic terms. For this reason this polymorph has been more considered in applied photocatalysis studies. Actually, the maximum photocatalytic activity is nearly always observed in the case of the commercial P25, a mixed phase system produced by Degussa (prepared by oxidation of metallic titanium and containing both rutile, almost 20%, and anatase, 80%, partially connected by a specific interface). Its huge photoactivity could be due to the interface between anatase and rutile phases which would favor the spatial separation of the photo-generated charges.[25-26]

1.1.2. Optical properties.

Titanium dioxide is usually considered a n-type semiconducting oxide. This electronic behavior is due to the presence of relating shallow donor state in the band gap.

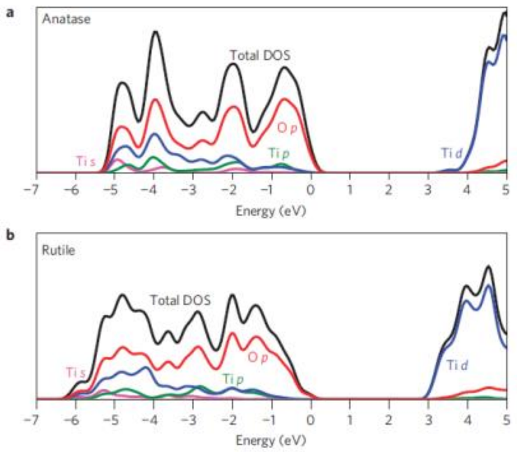

Figure 3. Calculated Electronic structure of anatase and rutile TiO_2. Comparison of the total and atom-decomposed electronic density of states of anatase (a) and rutile (b) TiO_2.[27]

Figure 3 shows the electronic density of states for rutile and anatase. The valence band edge of both materials is predominantly formed by O 2p orbitals, and the conduction band edge is dominated by Ti 3d orbitals.[27]

Anatase has an indirect band gap, which energy is about 3.2 eV. Rutile has a direct band gap, which energy is about 3.05 eV. Both of them are in the UV region of light making bare titania not suitable for visible light applications.

1.1.3. Paramagnetic defects.

Since TiO_2 is important in photocatalytic processes, the study of the mechanisms of charge transport, stabilization, recombination, and reactivity is fundamental to understand the properties of this oxide and to develop strategies to control these properties.

The photocatalytic process starts with the UV irradiation of the oxide that entails a charge separation. This leads to the promotion of an electron (e^-) from the valence band (VB) to the conduction band (CB) and the formation of an electron hole (or hole, h^+) in the valence band (eqn 1).[28]

$$TiO_2 + h\nu \rightarrow e^-_{(CB)} + h^+_{(VB)} \qquad (1)$$

The photo-separation is followed by a charge migration to the surface, charge trapping and, eventually, charge transfer to molecules adsorbed on the surface.[29] If the charge carriers (e^-, h^+) are not transfered to other molecules or neither recombine, the electrons are trapped by Ti^{4+} forming Ti^{3+} and the holes are stabilized on O^{2-} forming O^- (eqn 2).

$$Ti^{4+} + e^-_{(CB)} \rightarrow Ti^{3+} \qquad (2a)$$

$$O^{2-} + h^+_{(VB)} \rightarrow O^- \qquad (2b)$$

These two species (Ti^{3+} and O^-) are paramagnetic, therefore EPR spectroscopy is one of the most suitable techniques that can be adopted to investigate their features and, similarly, those of the radical intermediates formed at solid surfaces after their reactions. In particular, EPR is highly sensitive and provides information about the symmetry of the paramagnetic center and the spin distribution.

Titanium dioxide is also a reducible oxide since it loses O_2 from the lattice when the oxygen partial pressure is decreased even at moderate temperatures.[26] This causes the simultaneous formation of oxygen vacancies and excess electrons which are trapped in the solid as Ti^{3+}, according to the following equation:

$$O^{2-} + 2Ti^{4+} \rightarrow ½\, O_2 + V_o^{\bullet\bullet} + 2Ti^{3+} \qquad (3)$$

where the empty oxygen vacancy is indicated using the Kröger and Vink notation and the excess electrons are stabilized under the form of paramagnetic Ti^{3+} ions.

In anatase two main paramagnetic species amenable to Ti^{3+} ions were identified via EPR. The former is an axial signal with $g_{//} = 1.962$ and $g_{\perp} = 1.992$ and has been assigned to reduced Ti^{3+} centers in regular lattice sites of the anatase matrix; the second is a broad line centered at $g = 1.93$ and is assigned to a collection of slightly different Ti^{3+} centers located at the surface, or in the subsurface region, that arise especially upon UV irradiation.[30]

In rutile three are the paramagnetic species belonging to Ti^{3+} ions. (i) A rhombic signal with $g_1 = 1.970$, $g_2 = 1.961$ and $g_3 = 1.948$ identified with Ti^{3+} centers at the surface or near the surface of crystals with a dehydrated surface (in the case of a hydrated surface the signal presents a slightly different value of g_1 ($g_1 = 1.973$)). (ii) A signal with rhombic symmetry with g values $g_1 = 1.966$, $g_2 = 1.961$ and $g_3 = 1.948$ that is assigned to Ti^{3+} centers at the regular (i.e. non-interstitial) cationic sites of the bulk rutile structure. (iii) A signal due to interstitial Ti^{3+} in rutile crystals with g values $g_1 = 1.978$, $g_2 = 1.975$ and $g_3 = 1.942$.[31]

In the case of brookite the signal resulting from Ti^{3+} ions in bulk lattice site is a signal with axial symmetry and g values $g_{//} = 1.989$ and $g_{\perp} = 1.960$. A broad signal centered at $g = 1.93$ is assigned to surface Ti^{3+} sites because of surface heterogeneity.[31]

As far as the formation of trapped hole centers ($O^{\bullet -}$) photogenerated by UV irradiation of polycrystalline anatase is concerned, two families of $O^{\bullet -}$ species have been observed in anatase, the former with g value $g_1 = 2.016$, $g_2 = 2.011$ and $g_3 = 2.005$ is present on both hydrated and dehydrated surfaces and is O_2 insensitive. For this reason it has been assigned to a $O^{\bullet-}$ species located under the surface (or in immediate surroundings of the surface) as a three-coordinated (bulk) center. The second $O^{\bullet-}$ species is characterized by a more anisotropic **g** tensor (g_1 = 2.029, g_2 = 2.017 and g_3 = 2.004) and is observed on hydrated surfaces only and its EPR signal vanishes upon O_2 physisorption. This species is, thus, more exposed at the surface of the oxide than the first one and has been assigned to a two-coordinated oxygen.[32]

Two types of photogenerated holes in rutile have also been observed: holes trapped at the lattice oxygen atoms located in the subsurface layer with g values g_1 = 2.019, g_2 = 2.014 and g_3 = 2.002 and holes trapped on the surface bridging oxygen atoms with g values g_1 = 2.026, g_2 = 2.017 and g_3 = 2.008.[33]

1.1.4. Applications.

Titanium dioxide has a wide range of application fields also because its low cost, chemical stability and non toxicity. From the industrial point of view it is used as a white pigment, in the textiles sector, in food as coloring and in pharmaceuticals field (for example in toothpastes and as UV absorber in sunscreen cream).[34] It can be used also in many optical devices, biomaterials and as catalyst or catalysts support in many reactions.[34-35]

Nevertheless the main property that makes titania and titania-based materials so widely studied is their photoactivity. Since the report of Fujishima and Honda in the early 1970's,[1] a lot of papers have been published about heterogeneous photochemistry, photocatalytic water splitting and hydrogen production, dye sensitization and solar energy conversion and removal of pollutants.[35] However the main problem that hampers the use of titania in industrial photochemistry application, i.e.

its low solar energy absorption, has not yet completely solved. This has stimulate the research aiming to the identification of new systems of suitable modification of the TiO_2 matrix.

1.2. Zirconium oxide ZrO_2

1.2.1. Structure.

Zirconium dioxide exists in three main polymorphs: cubic, tetragonal and monoclinic (Figure 4) as pointed out by the thermodynamic phase diagram.[36]

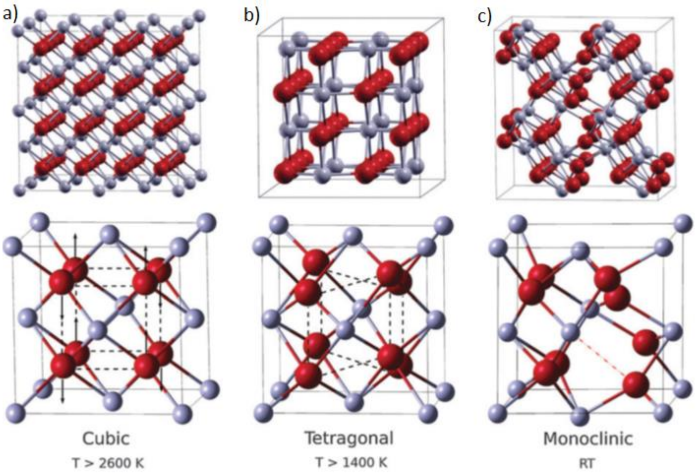

Figure 4. Crystallographic unit cells of a) cubic, b) tetragonal and c) monoclinic ZrO_2, red spheres are O ions, blue spheres are Zr ions.[37]

Below 1170 °C the monoclinic phase (baddeleyte) is thermodynamically stable. Between 1170 °C and 2370 °C ZrO_2 presents a tetragonal structure, while above 2370 °C ZrO_2 is in cubic structure, until it reaches its melting point around 2706 °C.[36,38] In literature an additional metastable tetragonal phase up to 650°C is also reported.[39]

The cubic phase shows the fluorite structure (symmetry Fm3m), which consists of a fcc pattern of Zr atoms with octahedral symmetry surrounded by eight oxygen atoms, the oxygen atoms have tetrahedral symmetry and are surrounded by four Zr atoms.

The other two phases derive from progressive distortions of the cubic one. In the tetragonal zirconia Zr atoms continue to be surrounded by eight O atoms and the O coordinated to four Zr atoms, but the symmetry decreases. The monoclinic phase presents Zr atoms coordinated to 7 O atoms with distorted symmetry and oxygen atoms can be tetra-coordinated or tri-coordinated.

The monoclinic polymorph is stable at low temperature (up to 1170°C) but exhibits a large volume and an anisotropic thermal expansion that can cause the cracking of manufacts during the tetragonal to monoclinic transition. For this reason the monoclinic polymorph has scarce applications in ceramic technologies. On the contrary, the other two polymorphs, cubic and tetragonal, are stable at high and intermediate temperature respectively and have excellent mechanical, thermal and dielectric properties.

1.2.2. Optical properties.

All ZrO_2 polymorphs can be considered as wide band gap oxides, since their band gap energy is around 5eV.[40]

The valence band is formed prevalently by the 2p states of oxygen ions, the conduction band is dominated by the 4d states of Zr^{4+} (Figure 5).[41]

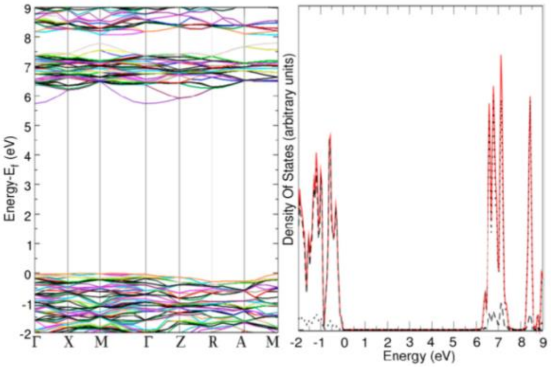

Figure 5. Band structure (left) and Density Of States (DOS) for bulk tetragonal ZrO_2. The total DOS is given in red, the DOS projected over the Zr d states is given by the dotted line, the DOS projected over the O sp states is given by the dashed line.[41]

1.2.3. Paramagnetic defects.

Various paramagnetic defects have been observed in zirconium dioxide. In particular three different EPR signals belonging to Zr^{3+} ions have been detected. The first corresponds to an axial signal with $g_{//} = 1.9768$ and $g_{\perp} = 1.9589$ assigned to Zr^{3+} bulk species (sometimes already present in the bare ZrO_2 prepared via sol-gel method).[42] The other two signals have the same perpendicular g value ($g_{\perp} = 1.978$) and differ in the parallel component ($g_{//} = 1.9288$ and $g_{//} = 1.906$) and are assigned to surface Zr^{3+} species formed upon irradiation in H_2 atmosphere.[41] Upon thermal annealing another EPR symmetric signal, at $g = 2.003$, arises. It represents only a very minor fraction of the overall reduced states observed via EPR. The assignment of this signal is still uncertain but, so far, it is associated with some trapped electrons present in line defects or in grain boundaries of the solid. A similar signal is, sometimes, present also in titanium dioxide upon thermal annealing.[30,41]
After irradiation of ZrO_2 in vacuum the photogenerated hole ($O^{\bullet -}$) species, with $g_1 = 2.0196$, $g_2 = 2.0101$, and $g_3 = 2.0045$, was observed,[43] which is formed in parallel to electron trapping sites (Zr^{3+})$^{.}$

1.2.4. Applications.

Zirconium dioxide is used in protective coatings, high dielectric materials and chemically inert refractory materials.[44] ZrO_2 is also important in heterogeneous catalysis. Due to thermal stability and presence of surface acid and basic sites, ZrO_2 has found applications in a series of catalytic reactions including hydrogenation, dehydration and isomerization of hydrocarbons.[39] The interest of ZrO_2 in photocatalysis is limited by both the high value of the band gap energy (around 5 eV) and the weak activity in photo-oxidation. However, the high negative value of the conduction band edge represents an advantage in terms of reductive potential. For this reason ZrO_2 has been tested in water photosplitting for hydrogen production[45-46] and in the photoactivation of carbon dioxide.[47-48]

1.3. ZrO_2-TiO_2 mixed oxide.

ZrO_2–TiO_2 mixed oxides were studied in recent years because they show original properties with respect to the bare ZrO_2 and TiO_2 oxides.[49-51]

As it can be seen from the phase diagram reported in Figure 6, ZrO_2 and TiO_2 can form solid solutions in a relative wide composition range. Until 1700°C Ti atoms, with a molar ratio between 2.5% and 18%, can enter in the tetragonal or monoclinic structure of ZrO_2 to form a solid solution, vice versa TiO_2 with a molar ratio up to 20% of Zr form a solid solution with rutile or anatase structure. From 20% to 40% molar ratio of Ti in ZrO_2 or Zr in TiO_2 a new stable intermediate compound named zirconium titanate with stoichiometry $Zr_{1-x}Ti_xO_4$ is formed beside the pure oxide ZrO_2 and TiO_2 solid solution. Between 45% and 55% molar ration only $Zr_{1-x}Ti_xO_4$ compound is formed.[52-54]

Zirconium titanate $Zr_{1-x}Ti_xO_4$ is a solid solution that can have compositions $x_{Ti}=0.42–0.67$ [x_{Ti} = molar Ti/(Ti+Zr)]. It includes the mineral $ZrTi_2O_6$ called srilankite and the synthetic compound $ZrTiO_4$.

All the $Zr_{1-x}Ti_xO_4$ compounds present the same orthorhombic α-PbO_2 (scrutinyite) structure with a *Pbcn* space group. The structure of scrutinyite is somehow similar to those shown by TiO_2 polymorphs being based on linked (MeO_6) octahedra. Over 1200°C $ZrTiO_4$ is in a "disordered" form since the metal ions are randomly distributed in the octahedral sites. Below 1200°C all $Zr_{1-x}Ti_xO_4$ undergo a continuous phase transformation that induce an order in the Zr-Ti distribution.[55-56]

For $ZrTi_2O_6$ (srilankite) compositions the ordered structure has one Zr layer every three Ti octahedral layers. In the case of $ZrTiO_4$ the structure corresponding to Zr-Ti order is more complicated. Christoffersen et al. found an "ordered" $ZrTiO_4$ compound formed by the alternation of two distorted Zr layers (8 coordinate) and two Ti layers (6 coordinate).[57] However the crystallization of $ZrTiO_4$ in the metastable 'high temperature' form (disordered) occurred around 700°C through sol-gel synthesis.[58]

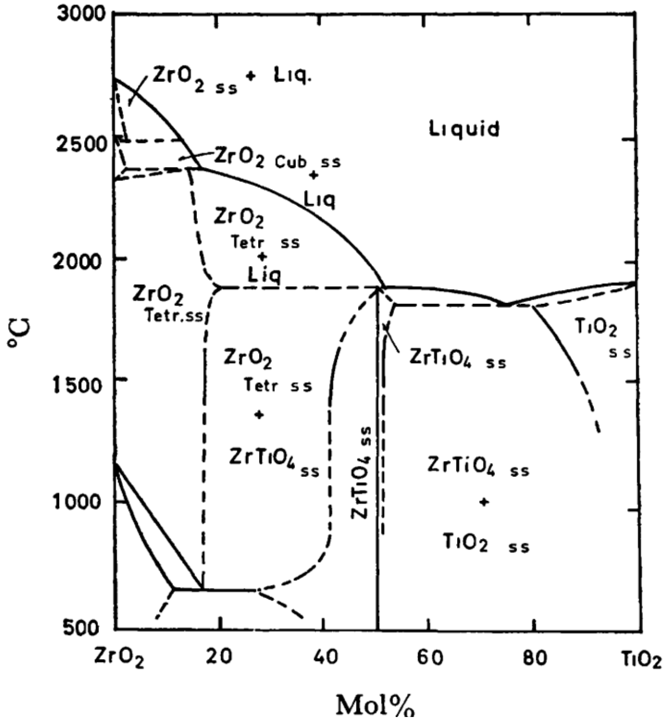

Figure 6. Phase diagram of ZrO_2-TiO_2 system.[53,55]

A relatively large number of studies have been devoted to the preparation and characterization of ZrO_2–TiO_2 mixed materials especially at the two extreme sides of the phase diagram, that is, in the region of high contents of Ti or Zr. These materials, indeed, show different optical and surface properties from that of the bare ZrO_2 and TiO_2 oxide.

The insertion of Ti atoms in ZrO_2 oxide has shown the capability of titanium impurities to modify the electronic structure of zirconia causing a net reduction of its band gap, in addition insertion of Ti favors oxygen deficiency, increases the thermal stability and modifies the surface acidity properties.[37,49,51,59-61] These features are responsible for the enhanced catalytic activity. Titanium modified ZrO_2 material are, therefore, used as catalysts and catalyst supports for various catalytic reactions such as dehydrogenation,[62-63] isomerisation[64-65] and photocatalytic applications.[66-68]

On the other hand the incorporation of Zr in the TiO_2 lattice influence (i) the thermal stability during sintering of the structure, inhibiting the conversion from anatase to rutile, (iii) the formation of photocatalytically active sites with increased surface area, (iii) the optical properties, (iv) the number (increased) of acids site on the surface.[69-72]

In both cases (Ti in ZrO_2 and Zr in TiO_2) the feature of the main oxide are modified by those of the counterpart forming materials with intermediate properties. For this reason it is interesting to explore a system whose stoichiometry is exactly midway between the two oxides: the zirconium titanate, $ZrTiO_4$, system.

1.3.1. Zirconium Titanate $ZrTiO_4$.

As previously described, zirconium titanate, $ZrTiO_4$, has a structure (orthorhombic Pbcn) which is very similar to those of all TiO_2 polymorphs being based on MeO_6 octahedra linked by three-coordinated oxygen (the scrutinyite structure, Figure 7). Remarkably the $ZrTiO_4$ phase is stable also over 1200 °C.[52,55,73]

In the structure shown in Figure 7, titanium and zirconium ions are randomly distributed on equivalent octahedral sites and are surrounded by six oxygen atoms. The oxygen atoms are connected to three metals ions.[74]

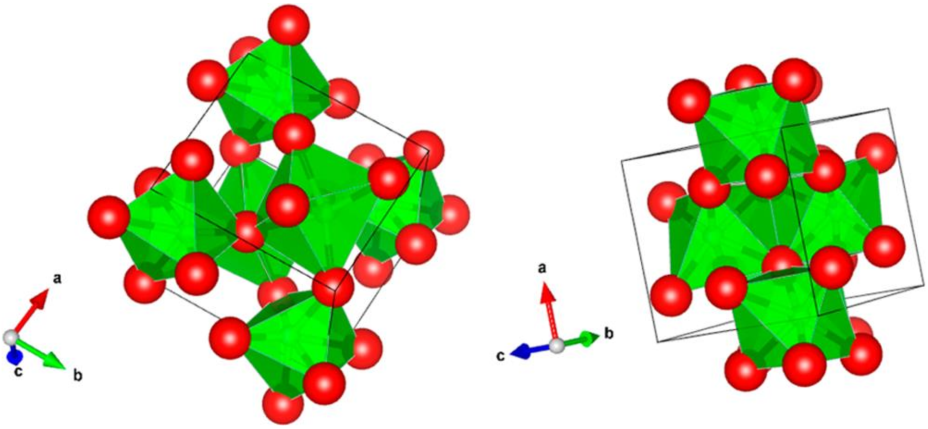

Figure 7. Structure of $ZrTiO_4$. The titanium or zirconium ions are located inside the octahedral constituted by the oxygen ions (red spheres).

$ZrTiO_4$ exhibits many attractive properties including excellent dielectric constant, high corrosion resistance, high permittivity at microwave frequencies, and excellent temperature stability.[75-78] For these reasons this material is widely used in technological application, such as in microwave telecommunications (as capacitor, dielectric resonator in filters, and oscillator),[79-80] optical devices,[81] memory devices (ReRAM),[82] and humidity sensors,[83] in the manufacture of high temperature pigments,[84] as structural ceramics,[78] and more recently, as biomaterial for medical applications.[85] However, the photochemical/photophysical and redox properties, of $ZrTiO_4$ remain poorly investigated.[86-89]

TiO_2 has proven to be the most effective photoactive oxide due to its many unique properties as previously described. However it has not a strong reductive capability as its conduction band potential is slightly negative with respect to NHE (0 V). On the other hand ZrO_2 has a more negative conduction band, but its band gap is too high to allow a large use in the field of photocatalysis. $ZrTiO_4$, that has a chemical composition exactly midway between TiO_2 and ZrO_2 could, hypothetically, have promising potential applications as photocatalytic material. In order to understand its potentiality, a preliminary study on its redox and photochemical properties is required.

2. Oxide doping.

Doping, i.e. the intentional introduction of impurities into a material, influences its properties, and is, thus, used in many technologies. Impurities can, indeed, strongly modify electronic, optical, and magnetic properties also in the case of semiconducting oxides.

If the impurity has one more electron than the atom that it replaces, it donates an extra electron to the material. This type of doping is called n-type doping (negative doping) and, in many case, the extra electrons lie in shallow energy levels just below the conduction band of the semiconductor. On the contrary, an impurity with one less electron provides an extra hole that lies in energy level just above the valence band of the oxide. This type of doping is called p-type doping (positive doping). These electrons or holes are then available as carriers of electrical current.

The infra band gap energy levels created by the dopants can also strongly influence the optical behavior of the oxide, since they can either accept electrons from the valence band or donate electrons to the conduction band allowing the absorption of photons with lower energy than the band gap. In some case thus the visible light becomes sufficient to permit the electron transitions.[90] For this reason a possible use of doped-oxides is for photocatalytic applications.

For instance, a way followed to increase the photochemical properties of TiO_2, which are restricted to the UV radiation without any modification, was the doping with transition metal ions like Cr^{3+}, Fe^{3+}, Mo^{5+}, V^{4+}.[91-92] Metal doping, indeed, can affect the light absorption properties, the adsorption capacity of adsorbed molecules, but also modify the charge carriers recombination rate always favoring their recombination. More recently a great deal of research points to insert non metallic elements like carbon[93], sulfur[94] or nitrogen[95] in the matrix of TiO_2 in order to increase the light absorption in the visible region. In particular N was found to be the most attractive and promising dopant in modifying the properties of several oxides.[10,12-13]

The metallic or non-metallic doping has been extensively studied, but, since the study conducted by Xu et al.,[96] the rare-earth metal doping has shown great interest. It was demonstrated, indeed, that a red-shift occurred in the band gap transition of rare-earth metal doped-TiO_2, allowing, thus, the absorption of visible light. Another property of lanthanides that attracts the attention of many scientists is that they could form complexes with Lewis bases such us organic acids, amines, aldehydes and alcohols, through the interaction of the functional groups with their f-orbital. This feature has made these materials interesting for the photodegradation of pollutants.[96-97]

In the following section a brief description of nitrogen and cerium doping of oxides will be provided.

2.1. Nitrogen doping of metal oxides.

The incorporation of nitrogen impurities into oxides is becoming an important topic in several contexts of materials chemistry research spanning from photocatalysis[98] to optoelectronics[99] and spintronics.[100] The insertion of nitrogen in the oxide lattice, indeed, represents a strategy to modulate the optical, magnetic and photochemical properties of the material.

Concerning the field of photocatalysis the aim of doping was to extend the photoactivity of these materials, which usually are activated by the UV component of light, to the visible range. In most metal oxides the N impurities usually form intra-band gap states just above the valence band, from which the electron can be promoted in the conduction band by visible light (Figure 8).[10,98,101]

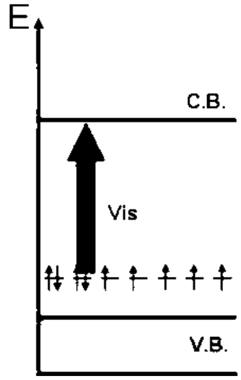

Figure 8. Electronic structure of N-TiO_2.[11]

Incorporation of N atoms into an oxide lattice has also been proposed to be an effective way to achieve p-type doping in oxide materials, which is fundamental for optoelectronic applications. In semiconducting oxides the N substitution for O creates an electron deficiency that means the introduction of one hole in the N states situated just above the valence band.[102] Doping of nitrogen into tantalum pentoxide (Ta_2O_5), for instance, has been recently reported to have a dual effect. The former is the visible light sensitization of this material for photoelectrochemical hydrogen production by water splitting and the second is a change in electronic structure that turns the material from n-type to p-type.[103]

In the case on SnO_2, for which the possibility to obtain a stable p-type form would have a huge impact on the fabrication of various kinds of optoelectronic devices, the doped material is still rich in excess electrons as a result of its higher propensity to lose oxygen that is, in turn, determined by the presence of N in the oxide. This evidence suggests that the chance to prepare a p-type form of tin oxide, at least via nitrogen doping, is extremely low.[104]

Several researchers have explored the effects of dilute doping of magnetic impurities on the physical properties of various oxides.[105] In these materials, nitrogen incorporation has been predicted to promote the onset of magnetic moments and ferromagnetic ordering at room temperature.[106] Once more, such effect is related to the substitution of nitrogen for oxygen leading to holes in N 2p states, which form local magnetic moments.

The nitrogen can become part of the crystalline lattice of oxides as substitutional nitrogen or interstitial nitrogen. In the first case nitrogen takes the place of a lattice oxygen atom assuming, in principle, a charge -2. Its electronic configuration is $1s^22s^22p^5$, where an electron belonging to a p orbital is unpaired, and the orbital itself carries a hole. In the second case, the interstitial nitrogen is intimately linked to a reticulated oxygen ion and thus can be described as a NO^{2-} species. In this case the unpaired electron lies on a π^* orbital. By XPS and coupling DFT and EPR investigation, it is possible to assign the paramagnetic nitrogen impurity to a defect involving an interstitial or substitutional form of nitrogen.

On the basis of the examples available in the literature, it seems that the nitrogen incorporation is easier in materials containing low coordinated oxygen ions. The more popular examples of N doping are in fact found for oxides having 3- or 4-coordinated oxygen ions as ZnO,[107-108] TiO_2 rutile and anatase,[12,109] WO_3 [110-111] and SnO_2.[112-113] In cases of N-ZnO or N-SnO_2 materials, substitutional impurities are reported. As far as TiO_2 is concerned, both forms of nitrogen, interstitial and substitutional, have been described. In case of ZrO_2 several studies on nitrogen doped ZrO_2 are reported in the literature.[114-116]

2.2. Cerium doping of metal oxides.

Insertion of Ce^{4+} cations into the lattice of several oxides, like TiO_2, is a questioned point in the literature.

TiO_2 and CeO_2 are basically immiscible due to the different crystal structure and to the different cationic size (Ce^{4+} 0.92-0.97 Å; Ce^{3+} 1.14 Å, Ti^{4+} 0.61-0.68 Å). The combination of these two oxides lead to the formation, at their interface, of small domains of mixed phases of cerium titanate ($Ce_2Ti_2O_7$, pyrochlore structure).[117]

The mixed materials exhibit a red shift of the band gap transition with respect to the pure oxides which causes an absorption in the visible range. This is due to the presence of Ce^{3+} (that has partially populated

4f levels) in the titanate which absorbs in the visible.[117-119] For this reason mixed Ti-Ce oxide materials were tested in the photodegradation of a variety of model pollutants, such as Rhodamine B[120] and formaldehyde.[121] This mixed oxide, moreover, was found to be able to form superoxide species reversibly adsorbed onto Ce^{4+} ions by simple contact with oxygen.[122] This feature make this material a good candidate for oxygen storage (and release) in heterogeneous catalysis.

In the case of ZrO_2, it has been reported that the dispersion of small amounts of cerium ions in the ZrO_2 lattice makes this oxide photosensitive to visible light. This photosensitivity has been ascribed to intra-band gap Ce 4f empty states, which should act as a bridge between the valence band and the conduction band of the oxide, allowing low-energy photons to excite electrons from one band to the other (Figure 9).[11,123]

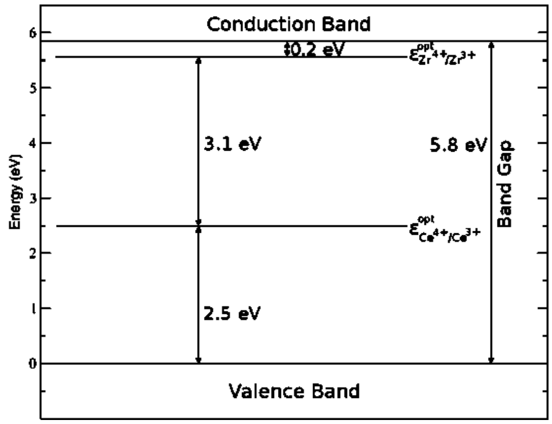

Figure 9. Optical transition levels for ZrO_2 doped with Cerium. [123]

3. The use of co-catalysts in water photo-splitting reactions.

In the past several decades, a lot of studies have been devoted to develop photocatalysts with improved solar energy absorption. The most employed strategies used to enhance the light absorption were doping, dye sensitization and the formation of heterojunctions. Furthermore, in the field of water photospitting, the use of co-catalyst to favor the release of gaseous H_2 and O_2 was adopted.[124] This is essential in particular in the case of the oxygen evolution reaction (OER) which is a four electron process, very difficult in absence of a specific co-catalyst, but is also extremely useful for HER (hydrogen evolution reaction). Currently, the most used photocatalyst systems are formed with noble-metal co-catalysts to achieve high photocatalytic activity. For example, Ru,[125] Pd,[126] Pt,[127] Au,[128] and Ag[129] have been extensively investigated as efficient co-catalysts for photocatalytic hydrogen evolution (HER). Among them, Pt is the most effective one. However, the drawback of these noble-metal based co-catalysts is that they are too expensive to be used for large-scale energy production. Therefore, it is crucial to find a valid alternative to these noble-metal co-catalysts. In recent years, several co-catalysts from cheap and earth-abundant elements have been developed. For example, copper oxide has been utilized as efficient co-catalyst for enhance the photocatalytic activity of TiO_2, especially for H_2 photoevolution.[24,130-131] A particularly interesting alternative approach is the use of a biocatalyst as co-catalyst. In particular, the [Fe-Fe] hydrogenase enzyme is known to catalyse the reversible reduction of H^+ ions to H_2. Quite recently hydrogenase-TiO_2 nanohybryds have been prepared and tested in photocatalytic process for hydrogen production based on solar light conversion.[18,132-136]

In photocatalytic water splitting, in particular for HER, an ideal co-catalyst plays three different roles: (i) it has to reduce the activation energy (or overpotential) for H_2 evolution reactions on the surface of semiconductors. (ii) it has to be capable of reduce the electron-hole recombination. (iii) it should increase the stability of the semiconductor photocatalysts. This latter property is important especially for the sulfides that are susceptible to oxidation by photogenerated holes, resulting in their self-decomposition.[137]

3.1. [Fe-Fe] Hydrogenase as co-catalyst for H_2 evolution.

Hydrogenase is an enzyme able to catalyze the reduction of protons to form H_2; the active site, called H-cluster, is composed by two subclusters, an iron sulphur cubane [4Fe-4S] cluster and a [2Fe] subcluster (Figure 10). The latter is based on an iron pair coordinated by two bridging sulphur atoms belonging to an organic ligand containing an amine group and by various non-protein ligands, namely three CO and two CN-groups; this binuclear cluster has two iron atoms: proximal iron (Fe_p) and distal iron (Fe_d), the latter has an open coordination site where the hydride can be coordinated during the catalytic cycle.

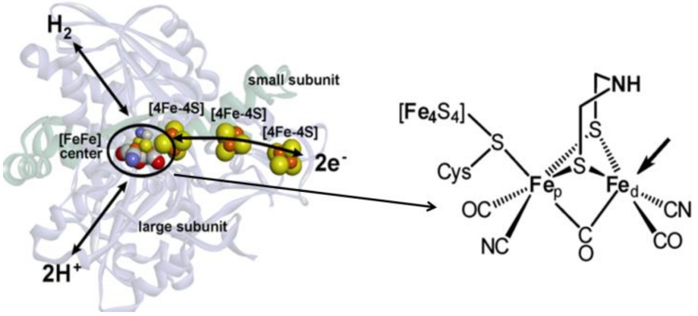

Figure 10. On the left the structure of the [Fe-Fe] hydrogenase is reported. Schematically the electron transfer chain (via iron−sulfur centers), and pathways for the hydrogen and the H^+ transfer are indicated by arrows. On the right, the geometrical structure of the active site of hydrogenases is shown; the arrow indicates the open metal coordination site.

Furthermore, the protein contains several chains of [FeS] clusters, with suitable redox potentials allowing the electron transfer from an external electron donor to the H-cluster, where the electrons combine with protons to form dihydrogen molecules (Figure 10).[138-141]

The structure and the catalytic mechanism of [Fe-Fe] hydrogenases have been largely studied in the literature.[141-143] Both the cubane and the binuclear part of the H-cluster are redox active.

The H-cluster, thus, can exists in different oxidation states, some of this are EPR active. Therefore the EPR technique has been widely used in recent years to investigate the paramagnetic states of the active site of hydrogenases.[144-147]

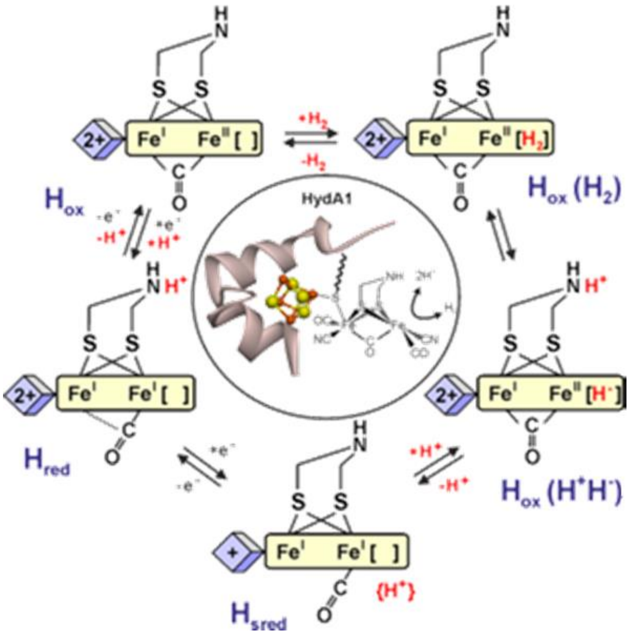

Figure 11. Proposed catalytic mechanism of [FeFe] hydrogenase.[139,142]

At the beginning of the catalytic cycle illustrated in Figure 11, the protein is in an "active oxidized" (H_{ox}) state in which one iron is Fe(I) and one Fe(II) and the cubane is oxidized. The distal iron presents a free coordination site. This state of the protein is paramagnetic and has a rhombic EPR spectrum that is typical of the H-cluster and is important for understanding the enzymatic mechanism. One-electron reduction generates an EPR silent "active reduced state" (H_{red}) in which both irons are Fe(I). In this situation a proton from the water solution can bind with the bridge amine group. Another one-electron reduction produces the "super-reduced state" (H_{sred}).[143] Here, the conversion between hydride and proton occurs: the protonated H_{sred} state can generate a hydride bound to the Fe_d which can then combine with a second proton available at the amine group to form H_2 reestablishing thus the H_{ox} state.[139]

The enzymatic activity can be inhibited by CO which binds to the open coordination site. The (H_{ox}-CO) state has the same electronic configuration as the (H_{ox}) state and shows a characteristic axial EPR spectrum.

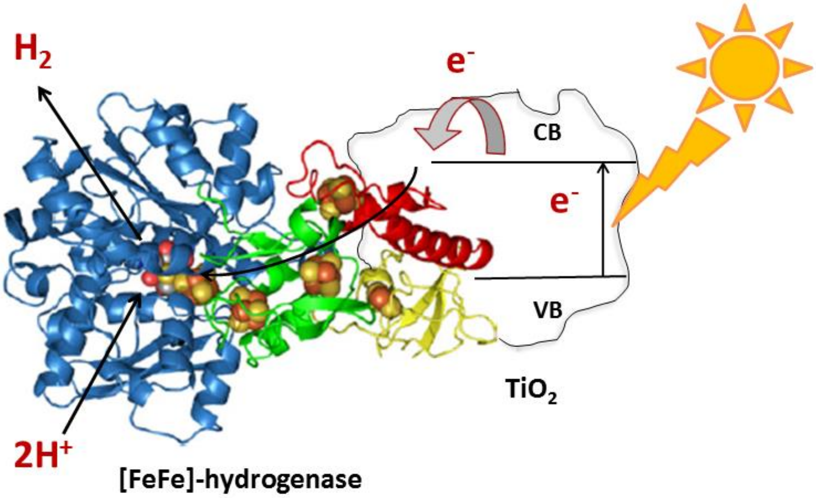

Figure 12. Representation of the mechanism for the H_2 evolution of the TiO_2-hydrogenase hybrid system.

Quite recently TiO_2-hydrogenase nanohybrids have been prepared and tested in photocatalytic process for hydrogen production based on solar light conversion.[18,132-136] The TiO_2-hydrogenase devices, indeed, are found to be able to produce hydrogen from water in the presence of a sacrificial electron donor as TEOA (triethanolamine).[18] The electrons generated by irradiation are transferred from TiO_2 to the active site of the enzyme where the reduction of water protons into molecular hydrogen occurs. Simultaneously, electrons are transferred from TEOA to TiO_2 giving rise to charge recombination (Figure 12). The protein in this hybrid system, thus, acts as a co-catalyst for H_2 photoevolution.

3.2. Noble metal nanoparticles as co-catalysts for H_2 evolution.

Noble metals, such as Pt, are used as the co-catalysts since are able to avoid the semiconductors charge recombination attracting the photoelectrons out to the surface. Furthermore noble metals are real proton reductions sites hence facilitate the proton reduction in the HER.[148]

The proton reduction depends from both the capability of the co-catalyst of trapping electrons from the semiconductor and the combination of surface hydrogen atoms into molecular hydrogen. The trapping ability is determined by the work functions of the noble metals, which are usually greater than those of semiconductors. For example, TiO_2 forms a junction with metals that produces a Schottky barrier and that facilitate the electron transfer to the metal (Figure 13). Photogenerated electrons are accumulated on metal nanoparticles without recombining with holes.[149] This causes a significant enhancement of the photocatalytic activity in H_2 production.

Noble metals with larger work function exhibits a lower Fermi level and, thus, they should be better electrons trap reducing the over-potential for H_2 production. For this reason, Pt, which exhibits the largest work function among many metals, is the best candidate co-catalyst for H_2 evolution.[150-151] Moreover, based on the metal-H bond strength and the types of surface orbitals of the metal, Pt shows the lowest activation energy for dihydrogen molecules production.

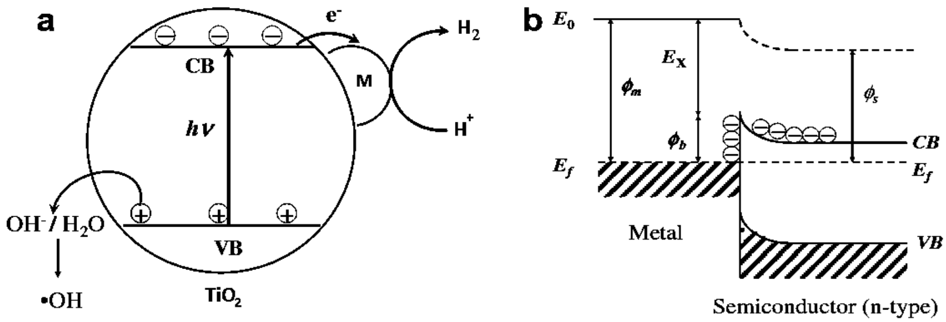

Figure 13. (a) Transfer and separation of photogenerated electrons and holes and (b) schematic of Schottky barrier in the metal–TiO_2 nanocomposite. [152]

3.3. Copper oxide as co-catalysts for H_2 evolution.

Instead of expensive noble metals, some earth abundant and low-cost transition metals, such as copper, have also been applied in photocatalytic H_2 evolution.[19-22,153-158] Nevertheless, up today, there is not a general consensus in the interpretation of the mechanism behind the high efficiency of this material. This is mainly due to the change oxidation state capability of copper and to the fact that the preparation pathway can affects the ratio among the different forms of Cu. Copper element in fact can be present as Cu^{2+} or Cu^+ ions or in the metallic form (Cu^0).

In the case of Cu^{2+} modified TiO_2 systems the real mechanism involved in the observed H_2 production still represents the most controversial aspect and conflicting models can be found in the literature. The solely presence of Cu^{2+}, indeed, is not enough to explain the high activity of the Cu(II) modified materials since the reduction potential for the redox couple Cu^{2+}/Cu^+ is positive (0.16V).[159]

It has been proposed however that the decoration with Cu(II) ions of the surface of TiO_2 can lead to the formation of CuO-like (Cu_xO)

structure. The common point of all these hypotheses is that, under UV excitation, electrons are promoted from the valence bands (VB) of both TiO_2 and CuO into their respective conduction bands (CB). Since the position of the CuO conduction band is much more positive than that of TiO_2, the photogenerated electrons should be transferred from TiO_2 to the CB of CuO, while the holes would be transferred from the VB of the TiO_2 to that of CuO. In this way, the recombination of electrons and holes can be avoided. The photoexcited electrons in CuO CB cannot directly contribute to the hydrogen production, since the CB edge position of CuO is more positive than the H^+/H_2 potential. Henceforth the hypotheses are divergent. For some authors the continuous accumulation of the excess electrons in the CB of CuO would cause a negative shift in its Fermi level, increasing the availability of the electrons to be transferred to H^+ (Figure 14).[160-161]

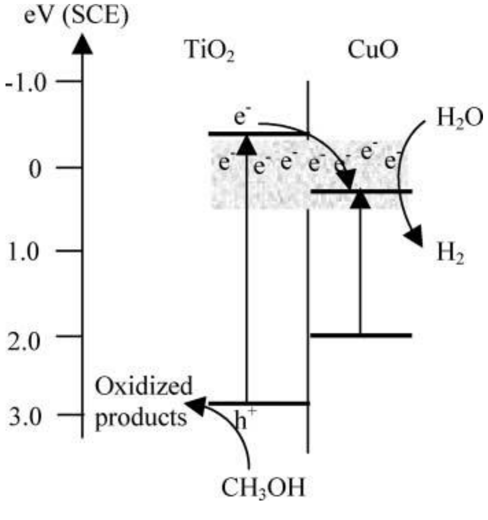

Figure 14. Schematic diagram showing the energy band positions of TiO_2, CuO and the electron transfer direction.[160]

According to other authors the accumulation of electrons at CuO causes the reduction of Cu^{2+} (in the form of CuO) to Cu^+ (in the form of Cu_2O). This causes a competition for electrons between CuO reduction and H_2

production, this explains the low hydrogen evolution rate in the initial stage of reaction. When the reduction process is completed the photogenerated electrons migrate from the CB of Cu_2O to that of TiO_2 while the holes migrate from the VB of TiO_2 to that of Cu_2O, resulting in a decrease in the recombination probability. In this process, the electrons that have reached the TiO_2 particle surfaces could react with H^+ to generate H_2, while the holes in the Cu_2O could be consumed by a sacrificial agent such as methanol (Figure 15).[20,23]

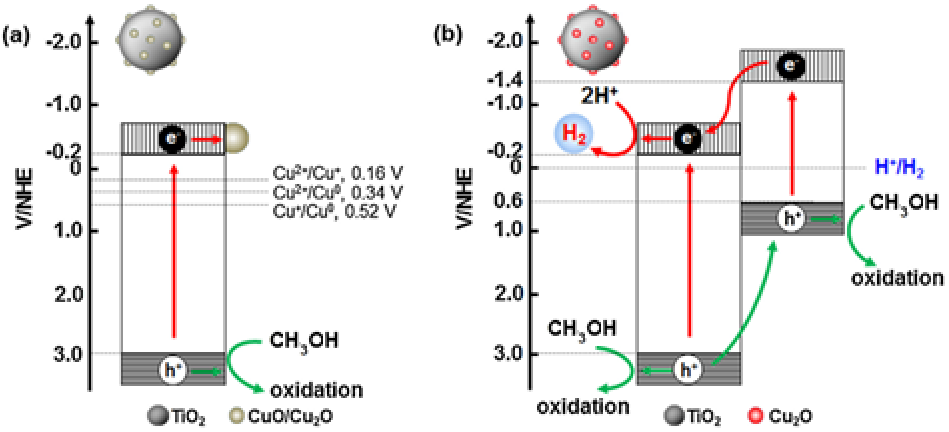

Figure 15. Proposed hydrogen photogeneration mechanism for: (a) the initial state Cu/TiO_2 upon light illumination; (b) the Cu/TiO_2 once the CuO has been reduced to Cu_2O by the photogenerated electrons.[20]

Another mechanism proposed for the CuO-TiO_2 system is based on the different properties induced by a different loading of CuO on the surface of titania.[24,162] At low CuO loadings copper exists as a sub-monolayer of CuO species on TiO_2. The CB of this species is more positive than that of the CB of TiO_2, hence the photoexcited electrons can be transferred from TiO_2 to CuO centres. Here the electrons can reduce the proton of water to H_2 since the CB of CuO monolayer is more negative than the H_2O/H_2 redox couple. At higher CuO loadings CuO nanoparticle formation occurs. The band gap of nanocrystals of CuO decreases with particle size (Figure 16). As the CuO nanoparticle size increases, the conduction band of CuO becomes positive with respect to H^+/H_2 couple, hampering the direct H_2 evolution. The CuO monolayer on TiO_2 is thus identified as the active site for efficient H_2 generation.

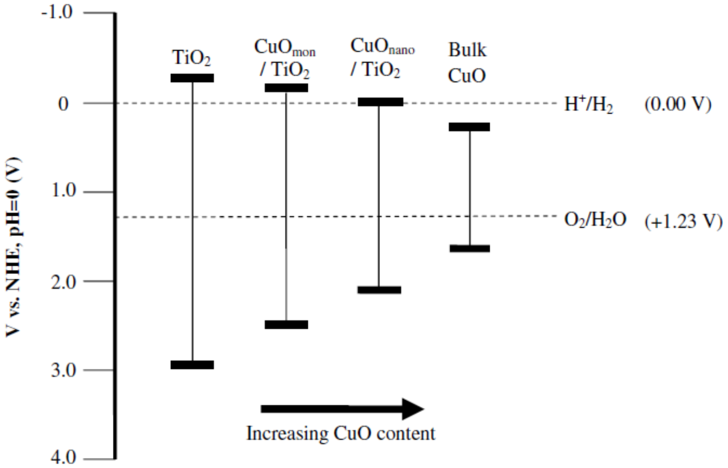

Figure 16. Band gap energies for TiO_2, CuO and CuO/TiO_2 photocatalysts.[24]

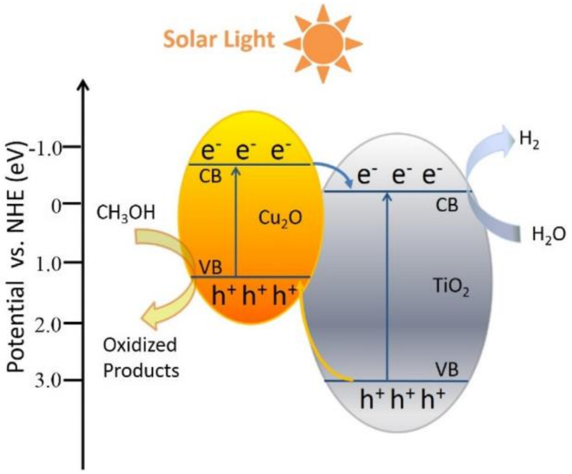

Figure 17. Schematic illustration of the band structures and charge transfer mechanism of Cu_2O-anatase TiO_2 heterojunction.[22]

As far as the Cu_2O-TiO_2 systems, in other word Cu^+ modified TiO_2, is concerned the H_2 evolution mechanism, above reported, is the same for all authors, i.e. the irradiation excited the electrons in Cu_2O from the valence band to the conduction band of both Cu_2O and TiO_2. Since the Cu_2O conduction band is more negative than the conduction band of TiO_2,[163] the photogenerated electrons are transferred from Cu_2O to the conduction band of TiO_2. Because of the TiO_2 VB is more positive than that of Cu_2O the holes generated in the valence band of TiO_2 move to the valence band of Cu_2O. Through this electron transfer process, the separation of photocarriers is improved and the production amount of hydrogen produced results very high (Figure 17).[21-22,164]

Moreover, some authors pointed out that in both CuO-TiO_2 and Cu_2O-TiO_2 system, after irradiation a part of copper oxide has been photoreduced to metallic Cu. This fact can further improve the separation of photogenerated electrons and holes and thus increase the photo-produced H_2 amount.[20,161,164-165] Metallic Cu, indeed, can act, like Pt, as an effective co-catalyst attracting the photogenerated electrons from the TiO_2 and then favoring electron transfer to the protons. [166-169]

Materials and methods

1. Samples preparation.

All reactants employed were purchased by Aldrich and used without any further purification treatment. Distilled water was used in the synthesis procedures. Synthesis procedures will be described for each system in the corresponding section.

1.1. TiO_2 systems.

Pristine TiO_2 anatase (hereafter TiO_2 or T) powder was prepared via sol-gel technique, mixing a solution of 15 ml of titanium(IV) isopropoxide in 15 ml of 2-propanol alcohol to which 16 mL of water were added. The gel was left to age for 15 hours at 290 K and subsequently dried at 343 K. The dried material was calcined in air at 773 K for 1 hour.

N-doped TiO_2 anatase (hereafter N-TiO_2) powder system was prepared with sol-gel technique mixing a solution of 15 mL of titanium(IV) isopropoxide in 14 ml 2-propanol alcohol with a solution of 0.54 g of NH_4Cl in 8 mL of water. The gel was kept for 15 hours at 290 K and subsequently dried at 343 K. The dried material (slightly yellow) was finally calcined in air at 773 K for 1 hour.

Reduced TiO_2 anatase (hereafter rd-TiO_2) powder was prepared via hydrothermal synthesis: 0.5 g of TiB_2 powder precursor were suspended into 20 mL of aqueous solution of HF (1 M), followed by hydrothermal treatment in a teflon autoclave at 453 K overnight. After the reaction, the product was filtered and washed with deionized water three times to remove dissoluble ionic impurities. Then the sample with a dark blue color was dried at 373 K for 1 hour.

Suspensions of TiO_2 powders in TEOA (triethanolamine) 25mM and thionine 1.39 mM aqueous solution were prepared mixing 4 mg of powder in 1 ml of solution. Each suspension was stirred and 70 μl of suspension were transferred in a EPR tube and gradually frozen at 77K for EPR measurements.

1.2. Hydrogenase preparation.

A part of this PhD study was performed in collaboration with the research group of Prof. Gilardi of the Life Science Department of the University of Turin. This group was involved in the preparation of the enzyme.

CpHydA [FeFe]-hydrogenase was cloned from Clostridium perfringens SM09, recombinantly expressed and purified under strict anaerobic conditions as described in Ref. 170.

1.3. Hydrogenase-TiO_2 hybrid materials preparation.

The preparation was carried out under an anoxic nitrogen atmosphere in a glove box (Belle Technology). The enzyme was anaerobically concentrated to 0.36 mM using Amicon Ultra 0.5 mL 30 K MWCO (Millipore). 8 mg of the TiO_2 powder were suspended and sonicated in 1mL of the anaerobic buffer 25mM TEOA pH 7. Subsequently, the enzyme and the TiO_2 suspension were mixed in a 1:1 volume ratio, resulting in final concentrations of 0.18 mM CpHydA and 4 mg/ml TiO_2. Thionine was added to a final concentration of 1.39 mM. 70 μL of this suspension were transferred in a EPR tube, sealed and gradually frozen at 77 K for EPR measurements.

1.4. $ZrTiO_4$ systems.

Pristine $ZrTiO_4$ (hereafter ZT) powder was prepared via the sol−gel technique, mixing a solution of 3.5 ml of titanium(IV) isopropoxide and 5 ml of zirconium(IV) propoxide (molar ratio 1:1) in 9 ml of 2-propanol to which 3.5 ml of water was added. The gel was left to age for 15 hours at 290 K and subsequently dried at 343 K. The dried material was calcined in air at 973 K for 1 hour. The powder presented a white color.

N doped-$ZrTiO_4$ powder (hereafter N-ZT) was prepared by mixing a solution of 1.75 ml of titanium(IV) isopropoxide in 1.75 ml of 2-propanol alcohol and a second water solution prepared with 2 g of $ZrOCl_2 \cdot 8H_2O$, 0.14 g of NH_4Cl and 5 ml of water. The resulting mixture was stirred at room temperature until a transparent solution was obtained. The solution was left to age for 15 hours at room temperature and subsequently dried at 343 K. Finally the dried material was calcined in air at 773 K for 1 hour. The powder so obtained has a yellow color. A material enriched with the ^{15}N isotope (^{15}N-$ZrTiO_4$) was prepared in the same way previously described using 98% ^{15}N enriched NH_4Cl.

Ce doped-$ZrTiO_4$ powders (hereafter Cex-ZT where x is the Ce molar ratio) powders were prepared via the sol–gel technique, mixing a solution of 3.5 ml of titanium(IV) isopropoxide and 5 ml of zirconium(IV) propoxide (molar ratio 1:1) in 9 ml of 2-propanol to which 3.5 ml of water solution of $CeCl_3 \cdot 7H_2O$ was added in order to have different molar ratio of cerium (0.5% and 10%). The gel was left to age for 15 hours at 290 K and subsequently dried at 343 K. The dried materials was calcined in air at 973 K for 1 hour. The powder presented vivid yellow color.

1.5. Copper modified oxide systems.

Cu_2O-TiO_2 (hereafter Cu_2O-T) and Cu_2O-$ZrTiO_4$ (hereafter Cu_2O-ZT) powders were prepared by chemical reduction followed by deposition method. At 10 ml of $Cu(NO_3)_2 \cdot 3H_2O$ $7.9 \cdot 10^{-3}$ M (0.5% wt on the basis of oxide) water solution were added 0.0568 g of glucose and 15 ml of NaOH $2.36 \cdot 10^{-3}$ M. The solution was stirred for 50 minutes at 343 K. At the end of the reaction a red suspension was formed (suspension A). In this reaction, known as Benedict reaction, glucose reduces Cu^{2+} to Cu^{+} allowing the formation of Cu_2O oxide. 1 g of oxide (TiO_2 or $ZrTiO_4$) was added in 20 ml of deionized water and the suspension was sonicated at 333 K for 10 minutes (suspension B). The suspension A was added to the suspension B and stirred for 10 minutes at 343 K. After this time the orange powder was filtered and washed three times with water and ethanol, in order to remove the reaction residues as glucose and NaOH, and finally dried at 343 K.

Cu^{2+}-TiO_2 (hereafter Cu^{2+}-T) and Cu^{2+}-$ZrTiO_4$ (hereafter Cu^{2+}-ZT) powders were prepared by wet impregnation. 1 g of oxide (TiO_2 or $ZrTiO_4$) was added in 20 ml of deionized water and the suspension was sonicated at 333 K for 10 minutes. 10 ml of $Cu(NO_3)_2 \cdot 3H_2O$ $7.9 \cdot 10^{-3}$ M (0.5% wt on the basis of oxide) were added to the oxide suspension and sonicated for 50 min at 333 K. After this time the suspension was stirred at 353 K until the formation of a dried blue powder. The powder was calcinated in air at 623 K for 4h and then washed three times with water.

1.6. Platinum - oxide systems.

Pt-TiO_2 (hereafter Pt-T) and Pt-$ZrTiO_4$ (hereafter Pt-ZT) powders were prepared by impregnation of the oxide with a Pt-colloidal suspension of nanoparticles of Pt. The colloidal suspension of nanoparticles of Pt was prepared by chemical reduction following three different steps:

- 125 mg of $HPtCl_6 \cdot 6H_2O$ were dissolved in 5 ml of water (solution C_1).
- 0.1 g of sodium citrate were dissolved in 10 ml of water (solution S_1).
- 7.5 mg of $NaBH_4$ and 0.1 g sodium citrate were dissolved in 10 ml of water (solution S_2).

To the solution C_1 2.5 ml of S_1 and 2.5 ml of S_2 (drop by drop) were added.

The colloidal suspension was stirred for 5 minutes and changes the color from yellow to black.

The impregnation of the oxide powder with Pt nanoparticles was performed mixing a suspension of 1 g of oxide (TiO_2 or $ZrTiO_4$) in 73 ml of water with 27 ml of the Pt suspension (0.5%wt on the basis of oxide) and stirring for 30 minutes. The final grey powder was filtered and washed three times with water.

2. Characterization methods.

2.1. X-Ray Powder Diffraction.

Powder X-ray diffraction (XRD) patterns were recorded with a PANalytical PW3040/60 X'Pert PRO MPD diffractometer using a copper K_α radiation source (0.154056 nm). The intensities were obtained in the 2θ range between 20° and 80°. X'Pert High-Score software was used for data handling.

2.2. UV-Visible Diffuse Reflectance Spectroscopy (DRS).

UV-Visible absorption spectra were recorded using a Varian Cary 5 spectrometer, coupled with an integration sphere for diffuse reflectance studies, using a Carywin-UV/scan software. A sample of PTFE with 100% reflectance was used as the reference. Spectra were registered in the 200–800 nm range at a scan rate of 240 nm/min with a step size of 1 nm. The measured intensities were converted with the Kubelka-Munk function.

The UV-Visible DRS studies after irradiation of the copper modified samples were performed irradiating 0.4 g of samples suspended in 2 ml of water/methanol solution (10% v/v) in a quartz cell for DRS measurement. After irradiation, prior to the spectra acquisition the sample were let to sediment on the bottom of the DRS cell. The UV-Visible DRS spectra were recorded in the 200–2500 nm range at a scan rate of 240 nm/min with a step size of 1 nm. Since during the irradiation was not possible to stir the samples, after every irradiation the samples were sonicated in order to make homogenous the powders.

2.3. Surface area measurements.

The surface area measurement was carried out on a Micromeritics ASAP 2020/2010 apparatus using the Brunauer–Emmett–Teller (BET) model for N_2 adsorption measurements. Prior to the adsorption run, the sample was outgassed at 573 K for 2 hours.

2.4. Electron Paramagnetic Resonance (EPR) characterization.

Continuous Wave Electron Paramagnetic Resonance (CW-EPR) experiments were performed with a Bruker EMX spectrometer operating at X-band (9.5 GHz), equipped with a cylindrical cavity operating at 100 kHz field modulation. All the spectra were recorded with a Modulation Amplitude of 0.2 mT. Other experimental parameters are reported in the caption of the figures.

Q-Band CW-EPR spectra have been recorded at room temperature (RT) on a Bruker ELEXYS 580 operating at a 50 kHz field modulation.

The spin counting was performed comparing the intensities of the EPR spectra of the samples with those of freshly prepared 2,2-diphenyl-1-picrylhydrazyl (DPPH) solutions in cyclohexane.

2.5. Transmission Electron Microscopy (TEM).

For $ZrTiO_4$ and N-$ZrTiO_4$ samples the nanoscale TEM imaging was performed in chemistry faculty of the Jagiellonian University (Poland) in collaboration with the research group of Prof. Z. Sojka by using a high-resolution transmission microscope Tecnai Orisis (FEI) with a X-FEG Schottky field emitter, operated at the accelerating voltage of 200 keV. For chemical composition analyses a windowless energy dispersive X-ray (EDX) system with a four-sector silicon drift detector (SDD) was used. The Z contrast images were acquired by means of a high-angle annular dark field (HAADF) detector in the scanning mode (STEM).

The STEM images coupled with the EDX elemental mapping were acquired by including the sample drift correction using the Bruker Esprit software. Prior to microscopic analysis, the samples were ultrasonically dispersed in ethanol and dropped on a holey carbon film supported on a copper grid (Agar Scientific, 300 mesh). Analysis of the observed TEM images was corroborated by the computer image simulations by means of the multislice method implemented in the JEMS software.[19] The Poisson noise at the level of 10% of the total contrast was added to the simulated images, to approach the experimental imaging conditions. To confirm the crystal phase assignment and reveal the orientation of crystallites, a single crystal diffraction pattern was simulated (within the kinematical and dynamical approximation) by means of the Rhodius software.[171-172]

For Ce-$ZrTiO_4$ samples the TEM images were performed at chemistry department of University of Torino using a high-resolution transmission microscope TEM JEOL JEM-3010 operated at a 300 keV ultrahigh resolution analytical. The microscope is equipped with Gatan US1000 CCD camera and an Energy Dispersive Detector OXFORD Software INCA.

2.6. UV-Visible Spectroscopy.

The UV-Visible spectra were obtained using UVIKON 930 (Kontron) spectrophotometer equipped with a deuterium lamp for the UV light and a tungsten lamp for the visible light. Spectra were registered in the 200–600 nm range.

2.7. Dynamic Light Scattering.

The mean hydrodynamic diameter and polydispersity index (PDI) of Pt-nanoparticles were obtained using a Zetasizer (Nano ZS Malvern Instruments) based on the Dynamic Light Scattering (DLS technique). The He-Ne laser used has λ=633nm.

3. Photoactivity tests.

An important feature of an efficient photocatalyst is related to the capability of the photogenerated charge to reach the surface of the nanoparticles and reacts with adsorbed molecules.

Such features can be preliminarily evaluated with two different methods. i) detection of photogenerated Reactive Oxygen Species (ROS) namely $O_2^{\bullet -}$ and $OH^{\bullet}$ radicals in solution. ii) reaction of photogenerated charge carriers with scavengers in gas phase. Scavengers are H_2 and O_2 for photogenerated holes and electrons respectively (see below).

The photocatalytic activity has been, then, tested monitoring the photoinduced hydrogen evolution.

3.1. Detection of photoformed charge carriers and ROS species.

The migration of photoformed electrons at the surface and their reactivity in electron-transfer reactions was tested firstly via EPR spectroscopy upon irradiation under oxygen gaseous atmosphere. The gas phase O_2 molecule reacts with photogenerated electrons, capable of reaching the surface, producing surface adsorbed superoxide O_2^- following equation 4

$$O_{2\ (gas)} + e^-_{(CB)} \rightarrow O_2^-{}_{(ads)} \tag{4}$$

The EPR detection of O_2^- upon irradiation under O_2 is, thus, the evidence of generation of surface reacting electrons.

These tests were performed irradiating the sample in presence of 20 mbar of oxygen at 77 K for 10 minutes. Before recording the EPR spectra the oxygen excess was removed from the gas phase in order to avoid dipolar broadening caused by physisorbed O_2.

The photocatalytic production of the superoxide ion (O_2^-) in water solution was also followed via spectrophotometric methods with nitroblue tetrazolium (NBT) molecule. This molecule can be reduced by the superoxide ion (O_2^-) forming the insoluble purple formazan (Figure 18).[173] Although formazan is soluble in aprotic solvents, it is insoluble in aqueous solutions. Hence, when formazan is produced during photocatalytic reactions in aqueous solutions a precipitation occurs. The amount of photogenerated superoxide ions was detected measuring the intensity decrease of the absorption maximum at 259 nm of NBT in the solution.

The tests were performed with 50 ml of NBT (20 µM) water solution and 0.05 g of photocatalyst powder (concentration of 1 g/l of photocatalyst). The suspension was left in dark for 15 minutes before the irradiation with UV-Visible light. Every 15 minutes of irradiation 3 ml of suspension was taken and the powder was removed from the solution by centrifugation. The supernatant solution was placed into a quartz cell in order to record the UV-Visible absorption spectra.

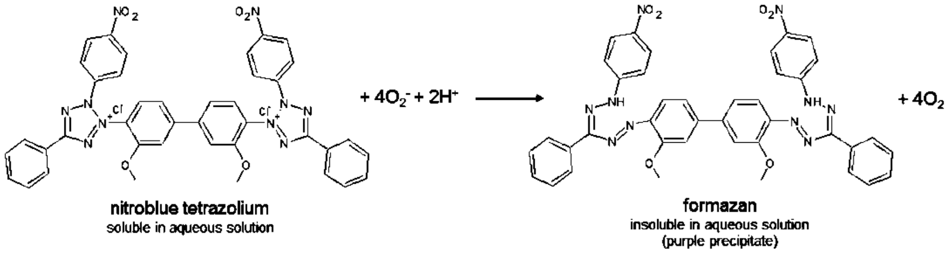

Figure 18. Reaction of nitroblue tetrazolium (NBT) with the superoxide ion.[173]

The formation and reactivity of holes upon irradiation was tested monitoring the formation of hydroxyl radicals ($OH^•$) in water solution. $OH^•$ radicals are formed by the reaction between water and the photoformed holes according to the following equation:

$$h^+ + H_2O \rightarrow OH^• + H^+ \qquad (5)$$

For this reason the detection of $OH^•$ radicals is an indirect evidence of the photoformed holes.

Due to their high reactivity, $OH^{\bullet}$ radicals can be detected by EPR in solution only using a spin trap molecule namely 5,5-dimethyl-pyrroline N-oxide (DMPO), a diamagnetic molecule that, reacting with $OH^{\bullet}$ radicals, forms a relatively stable radical detectable with EPR spectroscopy.

For these tests 500 μl of phosphate buffer 0.5 M and 250 μl of water were added to 250 μl of DMPO 0.085M water solution. 27 mg of the photocatalyst powder were added to the solution. The suspension was irradiated with UV-Visible light (excluding the deep UV components with a cut-off 315 nm) with an irradiance of 200 W/m^2. At different irradiation time the EPR spectra of the solution were recorded collecting the sample with a capillary.

The holes transfer capability was also tested in gas phase irradiating the samples under H_2 atmosphere. Under such conditions, the holes photogenerated in the valence band migrate to the surface, where they interact with molecular hydrogen (H_2) that undergoes a homolytic splitting generating reactive hydrogen atoms. $H^{\bullet}$ atoms, in turn, react at the surface, injecting electrons into the solid (see eqn. 6-9).[174] The evidence of surface hole reactivity is thus the formation of reduced species (Ti^{3+}, Zr^{3+},…) due to the electron generated according to equation 9 that can ben detectable by EPR spectroscopy.

$$MO_x + h\nu \rightarrow e^-_{(CB)} + h^+_{(VB)} \qquad (6)$$

$$h^+_{(VB)} + O^{2-}_{(surf)} \rightarrow O^-_{(surf)} \qquad (7)$$

$$O^-_{(surf)} + H_2 \rightarrow OH^-_{(surf)} + H^{\bullet} \qquad (8)$$

$$H^{\bullet} + O^{2-}_{(surf)} \rightarrow OH^-_{(surf)} + e^- \qquad (9)$$

The EPR spectra were recorded after irradiating the samples at 77K in 50 mbar of H_2 for 10 minutes.

3.2. Photocatalytic H_2 evolution.

For the hydrogenase-TiO_2 hybrid systems the hydrogen evolution test was performed in a 7 ml glass vial filled with 1 mL of O_2-free sample solution containing TEOA (25 mM pH 7), 1 mg/ml of TiO_2 and CpHydA (50 nM). They were irradiated for 60 minutes under natural sunlight at a flux of approximately 650 W/m^2. During irradiation the samples were kept on ice. Control experiments in the absence of TiO_2, or the enzyme or in the dark were also performed. All the samples were tested at the same time, under the same experimental conditions.

The hydrogen evolution has been measured via gas chromatography. The gas chromatograph (Agilent Technologies 7890A) was equipped with purged packed inlet, Molesieve 5A column (30 m, ID 0.53 mm, film 25 mm) and thermal conductivity detector (TCD). Argon was used as carrier gas. Quantitative separation was achieved in less than 3 minutes at 333 K.

For the Copper and Platinum modified TiO_2 and $ZrTiO_4$ samples the hydrogen evolution tests were performed in a 100 ml flask reactor of quartz with a rubber septum for bubbling and sampling. 0.1 g of photocatalyst were suspended in a 10% v/v methanol aqueous solution (72 ml H_2O and 8 ml of methanol) and sonicated for 10 min. The amount of powder is thus 1.25 g/l. The irradiation was performed with a 150W Xe lamp with an irradiance power, measured with a UV sensor, of 40 mW/cm^2. A magnetic stirrer was placed at the bottom of the reactor to keep the particles in suspension during the experiment. Prior to illumination, nitrogen was purged into the reactor for 30 min to remove dissolved oxygen. The photocatalytic hydrogen activity was then studied by illuminating the suspension for 4 hours.

To evaluate hydrogen generation a 200 µl gas sample was taken every 30 min from the reactor head space through the rubber septum. The gas samples were then injected into a gas chromatograph equipped with a HayeSep Q 80/120 column and a TCD detector. Nitrogen was used as the GC carrier gas and the rate of the flow is 1.0 ml/min.

Results and discussion

1. The zirconium titanate systems.

$ZrTiO_4$ exhibits a structure similar to those of TiO_2 polymorph but half of its atoms are zirconium. This matrix modification of titania, with the insertion of zirconium atoms, lead to changes in both the band gap energy value (E_g) and the conduction band potential of titanium dioxide ($E_g = 3.2$ eV for anatase) becoming, in principle, more similar to that of zirconia ($E_g = 5$ eV).

A system that maintains the general photocatalytic properties of titania (mainly the photooxidation ability related to the holes in the valence band) and simultaneously increases its reductive abilities should be of remarkable interest in the area of photocatalysis. This fact prompted us to investigate the photophysical and photochemical properties of $ZrTiO_4$. Indeed, despite the widely use of $ZrTiO_4$ in technological application, its photochemical/photophysical and redox properties remain poorly investigated.[86-89]

The purpose of this chapter of the PhD thesis is the study of the electronic structure of zirconium titanate, its band potentials, its behavior under irradiation, and the presence of surface trapping sites for photogenerated charge carriers. This approach is suitable to preliminary understand the potential of this material in terms of photoactivity and photocatalysis.

Despite its potential advantages, $ZrTiO_4$ exhibits, like TiO_2 and ZrO_2, a high band gap and thus its main limit is the absorption of the UV fraction only of the solar light. For this reason modifications of this oxide have been also investigated, namely with nitrogen and cerium, in order to influence the photoactivity of the system possibly with an extension towards visible light absorption.

The results of this chapter will be organized as follow: first, the redox and photochemical properties of pristine $ZrTiO_4$ (ZT) will be described.

Afterwards the feature of N-doped $ZrTiO_4$ (N-ZT) and Ce-doped $ZrTiO_4$ (Cex-ZT where x is the Ce molar ratio) systems will be described and finally a comparison of the photoactivity of all samples will be provided.

The investigation of these materials is supported by DFT calculations performed in collaboration with the research group of Prof. G. Pacchioni (University of Milano Bicocca).

1.1. Pristine $ZrTiO_4$.

1.1.1. Structural, morphological and optical characterizations.

XRD analysis of $ZrTiO_4$ powder (ZT) produce the XRD pattern reported in Figure 19A (black line) together with the reference lines of this compound (red lines). All the peaks of the diffraction pattern of the sample correspond the $ZrTiO_4$ phase[175] and no segregations of TiO_2 or ZrO_2 are observed.

The surface area of the ZT sample measured by the BET method corresponds to 66 m^2/g.

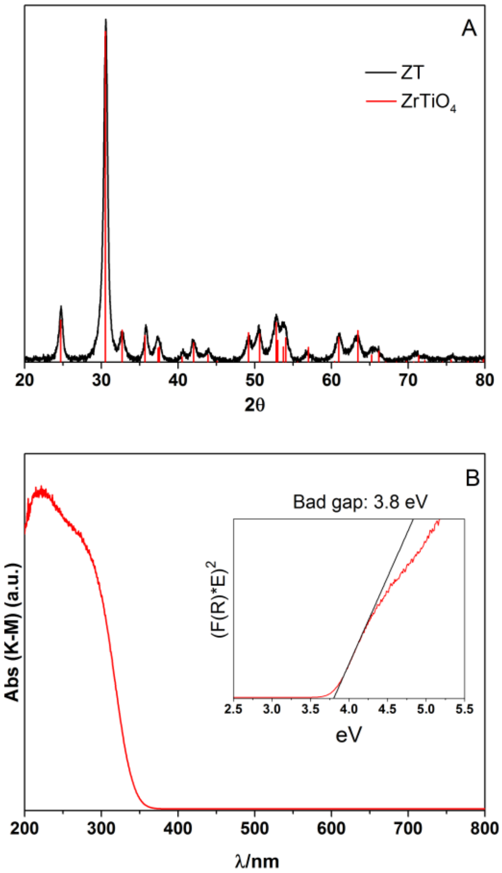

Figure 19. Panel A: X-ray diffraction patterns of ZT (black line) and reference of $ZrTiO_4$ (red lines).[174] Panel B: UV–Visible diffuse reflectance spectrum of ZT powder. In the inset the Tauc's plot is reported.

The optical UV-Visible absorption of ZT is shown in Figure 19B. The inset of Figure 19B shows the Tauc's plot of the optical absorption spectrum to evaluate the experimental band gap value.

According to Tauc's relation, the absorption coefficient α is given by

$$\alpha(h\nu) = B(h\nu - E_g)^m \qquad (10)$$

where B is an energy independent constant, α is the absorption coefficient, E_g is the optical band gap energy, h is Planck's constant, ν is the frequency of the incident photon, and m is an index that depends on the nature of electronic transition responsible for the optical absorption. Values of m for the allowed direct and non direct transitions are 1/2 and 2, respectively. Direct transition occurs when the valence band maximum and the conduction band minimum are at the same point in the Brillouin zone, while a non-direct one occurs when the maximum and minimum are at different places. In the present case, since the calculated electronic bands are almost flat (Figure 20), $ZrTiO_4$ could be considered a direct band gap oxide. The optical band gap energy evaluated with Tauc's plot for a direct transition is 3.8 eV, which corresponds to about 326 nm. The optically detected band gap value is intermediate between that of the two binary oxides of reference (TiO_2, ZrO_2) though closer to that of titania.

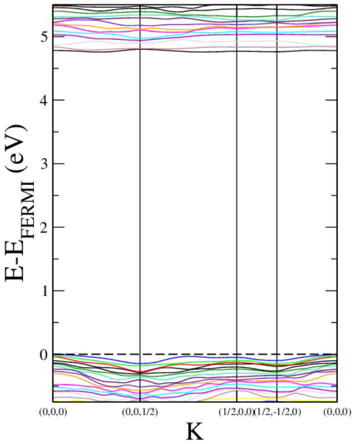

Figure 20. Calculated electronic bands of $ZrTiO_4$.

The TEM, STEM images and EDX maps shown in Figure 21 and Figure 22 were acquired at the chemistry department of the Jagellonian University (Krakow, Poland) in collaboration with the research group of Prof. Z. Sojka. The TEM images reported in Figure 21a,b show the morphological and structural feature of the $ZrTiO_4$ nanoparticles. They exhibit rounded shape and a rather narrow grain size distribution with an average diameter of about 15 nm in agreement with the Scherrer analysis of the XRD pattern. The nanoparticles are aggregated into elongated structures that form globular agglomerates of 100−200 nm diameter.

The corresponding selected area electron diffraction (SAED) pattern shows the polycrystalline nature of $ZrTiO_4$ sample (Figure 21c). The observed diffraction rings were indexed within the orthorhombic structure of $ZrTiO_4$ (space group Pbcn, reference JCPDS diffraction pattern No. 34–415).

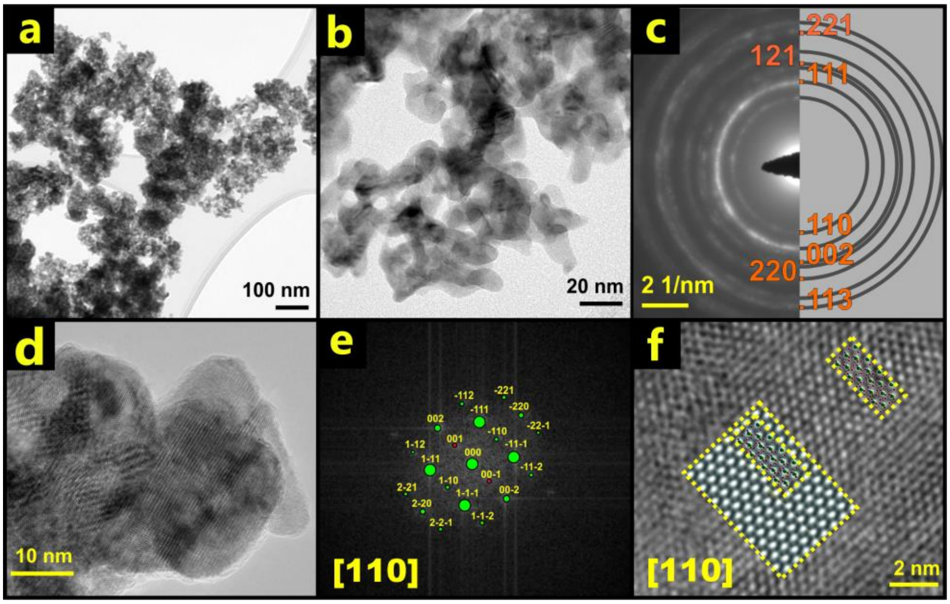

Figure 21. TEM images of the $ZrTiO_4$ nanostructures (a, b) along with the polycrystalline electron diffraction SAED pattern (c). High resolution image of the nanocrystallites (d), and FFT pattern taken from the HR TEM image viewed along the [110] direction with the superimposed simulated single crystal diffraction pattern (e). The simulation was carried out taking into account kinematical (green dots) and dynamical (red dots corresponding to the (001) and (00-1) reflections) scattering. HR-TEM image of the orthorhombic $ZrTiO_4$ nanoparticle oriented along the [110] axis (f) together with the simulated image (yellow rectangle) and the superimposed atomistic structure of $ZrTiO_4$ (Zr green dots, Ti blue dots, O red dots).

The HR-TEM image (Figure 21d) shows the presence of ordered lattice fringes that confirm a high degree of crystallinity of the $ZrTiO_4$ nanoparticles. Simulation of the FFT diffraction pattern (Figure 21e) allows the straightforward assignment of all observed diffraction spots and determination of the nanocrystal alignment along the [110] direction. The corresponding HR-TEM image was simulated (Figure 21f) within the extended Scherzer defocus regime and the spherical aberration constant Cs = 12 μm and matches perfectly with the experimental one. Analysis of the calculated thickness-defocus maps showed that the observed nanocrystal has the thickness of about 8 nm.

Within the applied imaging conditions, the bright spots define the positions of the mixed zirconium and titanium columns, whereas oxygen columns remain invisible.

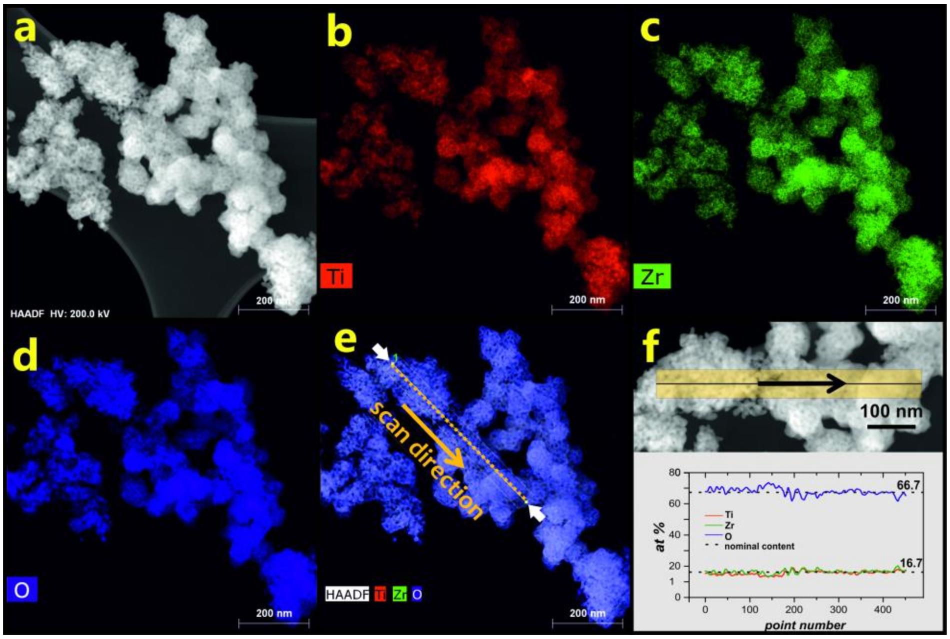

Figure 22. STEM-HAADF image of the $ZrTiO_4$ nanostructures (a) along with EDX maps (b–d) showing distribution of the constituting elements Ti (red), Zr (green), and O (blue). EDX line profile across the $ZrTiO_4$ aggregates (e) and the corresponding variation of the composition (f).

The composition homogeneity of the sample at submicro-nanoscale was examined with HAADF/STEM pictures (Figure 22a) and EDX maps (Figure 22b-f). Despite a small fluctuations of the Ti and O content, (-2.5 at. %, +3.6 at. % for Ti and O respectively, left part of the plot of Figure 22f), the 1:1:4 stoichiometry of $ZrTiO_4$ is well preserved. Summarizing, the obtained microscopic results revealed good homogeneity and crystallinity of the synthesized material.

1.1.2. Band alignment.

The alignment of the band potential of $ZrTiO_4$ with those of the two binary reference oxides has been done following the procedure reported by Butler [176] and based on the Mulliken electronegativity of the elements (Figure 23). The results obtained for both TiO_2 and ZrO_2 are close to what has been found for the same oxides in various reports.[177-179]

The valence band edge of $ZrTiO_4$ is, in this way, slightly more positive than that of TiO_2 (0.32 eV); thus, on the basis of the energy gap value, the limit of the conduction band of the solid is 0.28 eV more negative of the corresponding one of titania (Figure 23).

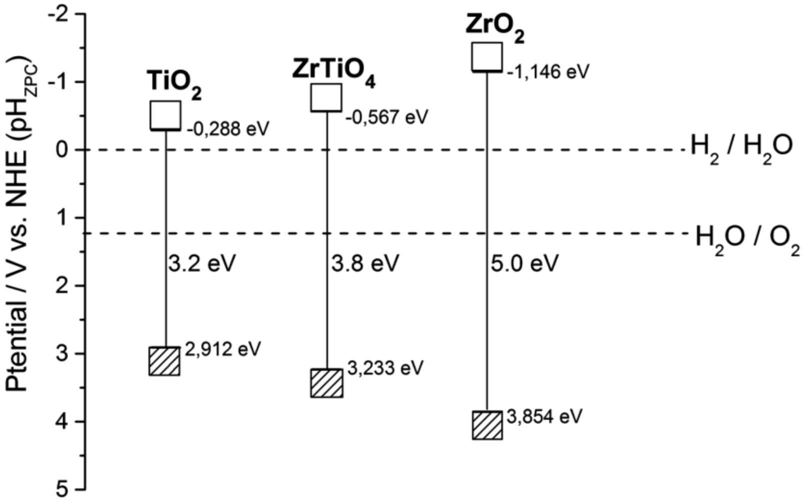

Figure 23. Relationship between the band structures of ZrO_2, TiO_2, and $ZrTiO_4$ and redox potentials of water splitting.

These results are in perfect agreement with preliminary ultraviolet photoelectron spectroscopy (UPS) valence band measures which were performed by the research group of Prof. G. Granozzi (University of Padova). In this case the comparison between UPS valence band spectra of $ZrTiO_4$ and that of TiO_2 anatase samples (Figure 24) reveals that the valence band maximum of $ZrTiO_4$ is 0.35 eV more positive than that of TiO_2 while, considering the energy gap value, the conduction band minimum of $ZrTiO_4$ is 0.25 eV more negative than that of TiO_2.

Summarizing the band positions of $ZrTiO_4$ material are almost at midway between those of the two reference oxides (TiO_2 and ZrO_2) although a bit closer to that of titania. Hence, the presence of a small but definite increment of the reductive potential of conduction band electrons in $ZrTiO_4$ with respect to TiO_2 can be assumed.

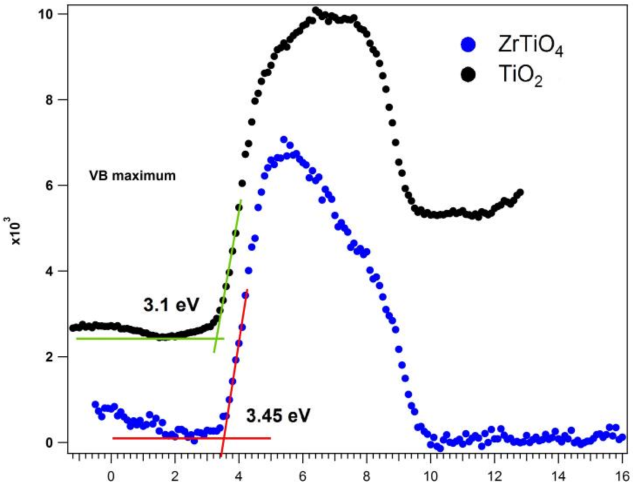

Figure 24. UPS valence band spectra of $ZrTiO_4$ (blue dots) and TiO_2 anatase prepared via sol gel method (black dots).

1.1.3. Redox properties investigated by EPR spectroscopy.

Annealing treatments of $ZrTiO_4$ were performed under vacuum at different temperatures for 1 hour from 373 to 873 K.

As previously mentioned (see Section 1.1.3 of Introduction chapter), in the case of reducible oxides, this type of treatment induces a loss of oxygen and generates, besides oxygen vacancies, two extra electrons per vacancy that normally reduce the metal.[180] It is useful to remember that, while TiO_2 is very sensitive to annealing as it forms reduced Ti^{3+} species at the early stages of the annealing process,[30] ZrO_2 is more reluctant to reduction with respect to TiO_2. Furthermore, in ZrO_2 the majority of extra electrons, formed upon annealing, are not EPR visible (in other words only a minor fraction of these electrons forms Zr^{3+} ions).[41]

The EPR spectra after annealing of the ZT sample are reported in Figure 25. The behavior of ZT in the early stages of annealing is more similar to that of ZrO_2 than to that of titania. The EPR spectrum of ZT (that contains tiny amount of Zr^{3+} defects in the starting material having $g_{//} = 1.978$ and $g_{\perp} = 1.960$, analogously to what occurs in pure ZrO_2) remains almost unchanged upon annealing until 573 K except for the tiny spectral component at $g = 2.003$, which slightly increases with the annealing temperature. As in the case of the parent oxides (TiO_2 and ZrO_2) such feature is related to trapped electrons and represent only a minor fraction of the overall reduced states observed via EPR.[30,41]

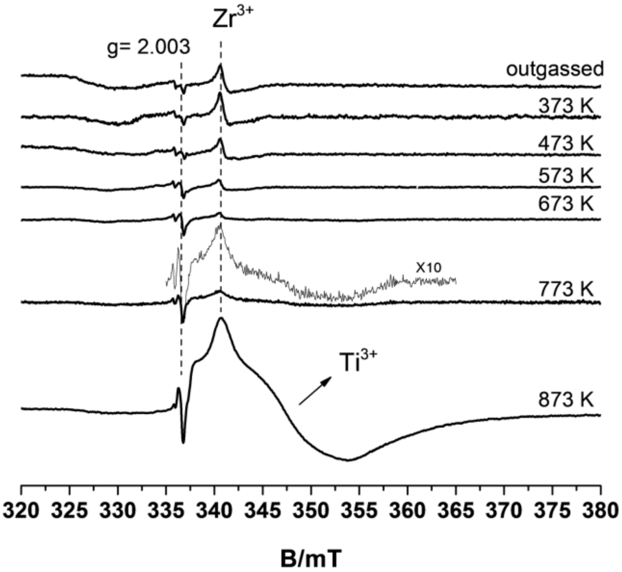

Figure 25. EPR spectra of ZT powder outgassed at room temperature and after annealing for 1 h under vacuum at the temperature indicated in the figure. All the spectra were recorded at 77 K at microwave power of 10 mW.

When the annealed ZT sample is contacted with O_2 after each step, no electron transfer to oxygen is observed, suggesting that annealing until this temperature does not modify the solid, which is much more resistant to reduction than titania. This is consistent with the computed oxygen vacancy formation energies, ΔE, which, in the case of of $ZrTiO_4$

is equal to about 6 eV, relatively close to that of ZrO_2 (7.2 eV).[41,181] At variance forming a vacancy in bulk TiO_2 has a smaller energy cost (4.5 eV).

Upon annealing at 673 K, while the EPR signal is still almost unaltered an initial reduction in the solid has occurred, as indicated in Figure 26A. When the material is contacted with oxygen, in fact, the formation of well-known signal of the O_2^- superoxide anion (Figure 26A(b)) occurs by electron transfer. The material, annealed at 673 K (Figure 25), is thus reduced but there is no EPR evidence of the localized excess electrons (Ti^{3+}, Zr^{3+}), which must therefore be present as diamagnetic centers, most probably, as suggested by calculations, as V_O^X neutral centers with two electrons in a vacancy (see Section 1.1.5). Hence, until an annealing temperature of 673 K, the behavior of the ZT system is close to that of ZrO_2.

The behavior changes upon annealing at higher temperature when the reluctance to oxygen release breaks down.

Already at 773 K, but more evidently at 883 K, a broad signal (around *g* = 1.93) assigned to surface Ti^{3+} ions is observed.[30] This evidence unambiguously indicates the presence of extra electrons in the solid produced upon O_2 release. Therefore the behavior of ZT material under an annealing at temperature higher than 673K, is closer to that of TiO_2 since no analogous signal was ever observed for ZrO_2.

According to the computed density of states (see Section 1.1.5), the empty Ti 3d levels are lower in energy than the Zr 4d ones and, thus, excess electronic charge accumulates on titanium ions.

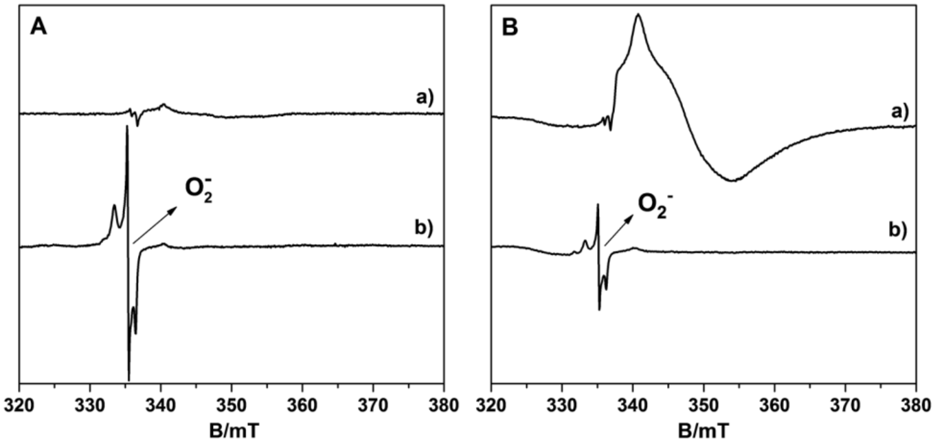

Figure 26. Panel A: EPR spectra of ZT reduced by annealing under vacuum at 673 K. Panel B: EPR spectrum of ZT reduced at 873 K. Spectrum (a) reduced ZT powder, spectra (b) reduced ZT powder after contact with 20 mbar of O_2 at room temperature (RT). Both spectra were recorded at 77 K and with a microwave power of 10 mW.

When the annealed solid at 873 K is contacted with oxygen at room temperature (Figure 26B(b)), the broad, intense signal belonging to the Ti^{3+} centers instantaneously disappears, and the signal of the superoxide O_2^- ions arises. Analyzing the spectra before and after O_2 adsorption (Figure 26B) in quantitative terms it can be noted that the integrated intensity of the EPR signal of the reduced sample (Figure 26B(a)) is one order of magnitude higher than that of the sample contacted with oxygen (Figure 26B(b)). The difference is due to the fact that the majority of oxygen is used to restore the O_2 losses caused by annealing, leading to O_2 incorporation in the lattice in the diamagnetic O^{2-} form following equation 11.

Only a minor fraction of the adsorbed oxygen remains partially reduced to superoxide O_2^- that is the only paramagnetic product.

$$O_2 + e^- \rightarrow O_2^- + e^- \rightarrow O_2^{2-} + 2e^- \rightarrow 2O^{2-} \qquad (11)$$

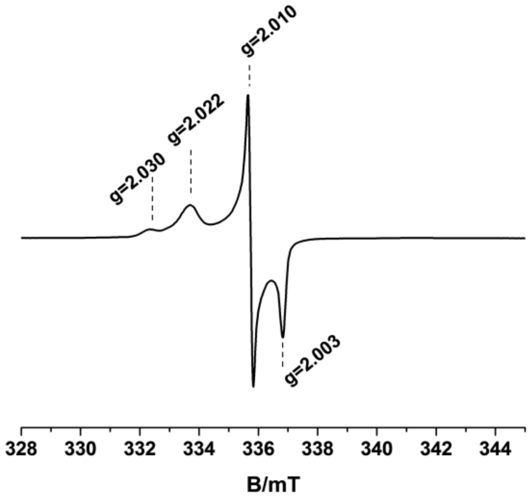

Figure 27. Magnification of the EPR spectrum of the superoxide radical formed by contacting the ZT sample annealed at 873 K with oxygen. The spectrum was recorded at 77 K and with a microwave power of 1 mW.

The features of the EPR spectrum of the superoxide radical (Figure 27) are characterized by a g_z region with two resolved components indicating the presence of O_2^- adsorbed on both titanium and zirconium tetravalent surface ions (g values in Table 1). The weaker g_{zz} component (g = 2.030) corresponds to superoxide ions adsorbed on Zr^{4+} ions, whereas the more abundant one (g = 2.022) is due to O_2^- on Ti^{4+} ions.[182] This indicates that both zirconium and titanium ions are exposed at the surface of the material.

g_{zz}	g_{yy}	g_{xx}	**description**
2.022 ± 0.002	2.010 ± 0.0005	2.003 ± 0.0005	O_2^- on Ti^{4+}
2.030 ± 0.002	2.010 ± 0.0005	2.003 ± 0.0005	O_2^- on Zr^{4+}

Table 1. g value of superoxide species adsorbed on a ZT sample extracted by simulation performed using SIM32 software.[183]

1.1.4. Photoformation and reactivity of charge carriers followed by EPR.

The photoactivity of $ZrTiO_4$ has been tested by EPR under UV−Visible irradiation in different condition: firstly the photo charge separation has been investigated recording the EPR spectra under irradiation of the sample in vacuum since by EPR it is possible to monitor the formation and stabilization of both photoexcited electrons and holes. Afterwards the capability of the material of charge transfer to molecules adsorbed on the surface has been tested under irradiation both in oxygen (to test the electron transfer) and hydrogen atmosphere (to test the hole transfer) (see Section 3.1 of Material and Methods chapter for more details).

In order to clean the surface of the oxide from some adsorbed impurity, before each experiment the sample was subjected to an activation process consisting in heating for 30 minutes at 773 K under vacuum and other 60 minutes in O_2 at the same temperature.

Irradiation under vacuum of the activated solid (showing already a weak trace of Zr^{3+} ions, Figure 28a) causes the appearance of two signals (Figure 28b). At higher field trapping of photoexcited electrons is manifested by the increase of Zr^{3+} and Ti^{3+} signals (broad lines amenable to surface species[31]). At a lower field the axial signal, characterized by the g components g_1 = 2.005 and g_2 = 2.014, corresponds to trapped holes (O^- ions).

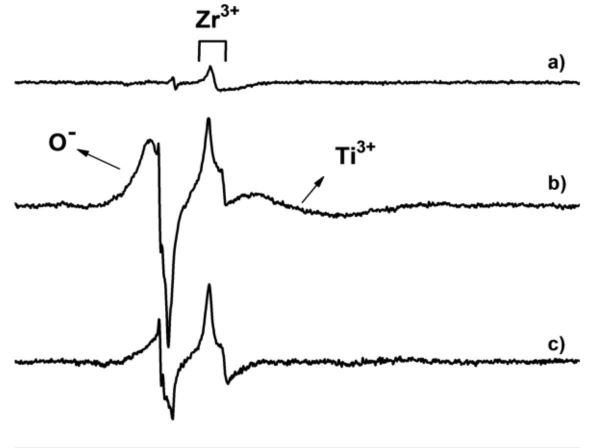

Figure 28. EPR spectra showing the effect of UV−Visible irradiation under vacuum of zirconium titanate: (a) activated sample in the dark; (b) after UV−Visible irradiation; (c) sample after a thaw−freeze treatment (lamp off, heating at RT and cooling again at 77 K). All the spectra are recorded at 77 K with a microwave power of 10 mW. The irradiation was performed in the EPR cavity at 77 K for 10 min with a UV−Visible light.

Spectrum c of Figure 28, which reports the sample after a thaw−freeze treatment (lamp off, heating at room temperature, and cooling again at 77 K), show that the majority of holes and electrons recombine and in particular the electrons, stabilized on Ti^{3+}, undergo a complete recombination upon temperature increasing. However part of the signals belonging to the holes and to Zr^{3+} ions are still appreciable indicating that a fraction of the charge trapping sites escapes recombination. Zr^{3+} ions seem, in fact, recombine less efficiently than Ti^{3+}.

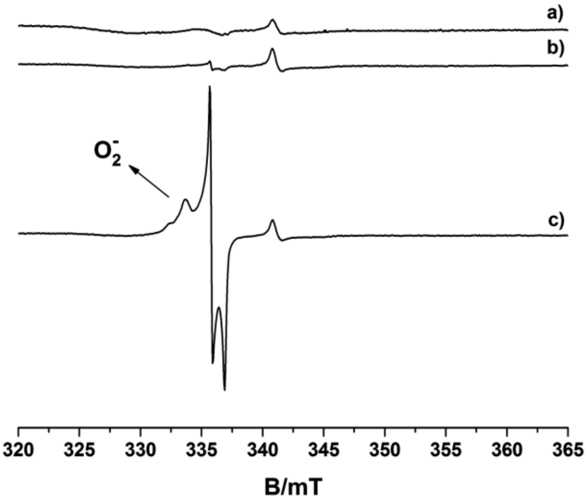

Figure 29. EPR spectra of a ZT sample irradiated in O_2 atmosphere: (a) activated sample in the dark; (b) same sample contacted with 20 mbar of O_2 in dark; (c) sample in (b) upon irradiation with UV−Visible light at 77 K. All the spectra were recorded at 77 K and with a microwave power of 1 mW.

The capability of ZT sample to transfer the photogenerated electrons has been tested studying the effect of the irradiation of the sample in oxygen atmosphere (Figure 29). Indeed, as mentioned in Section 3.1 of Material and Methods chapter, the formation of superoxide upon irradiation under O_2 is the evidence the migration of the photogenerated electrons to the surface and of their reactivity.

While the spectrum of the activated material (Figure 29a) does not change contacting the powder with of O_2 (Figure 29b), after irradiation with UV−Visible light in O_2 atmosphere an intense signal typical of superoxide ions appears (Figure 29c). No evidence of Ti^{3+} nor Zr^{3+} ions is visible (the trace of Zr^{3+} already present in the starting material is not altered by irradiation) indicating that the electron transfer from the solid to the O_2 molecule occurs.

The feature of the EPR spectrum of the superoxide radical formed upon irradiation is strictly similar to that observed upon reoxidation (Figure 26) and is due to two species of superoxide ion respectively adsorbed on Ti^{4+} and Zr^{4+} ions present at the surface of the solid.

On the other hand, the transfer of photogenerated holes at the surface of $ZrTiO_4$ has been tested irradiating the solid with UV−Visible light in H_2 atmosphere. In this case the fingerprint of surface hole reactivity is the formation of reduced species (see Section 3.1 of Material and Methods chapter). The effects on the EPR spectra of the irradiation in H_2 atmosphere are reported in Figure 30. The background spectrum (Figure 30a) does not change when the powder is contacted with of H_2 (Figure 30b). However, upon UV−Visible irradiation (Figure 30c) a very intense signal typical of Ti^{3+} arises. The formation of this signal is due to both trapping the photogenerated electrons and the injection of electrons caused by the reaction of holes with H_2 molecules according to the following reaction scheme:

$$ZrTiO_4 + h\nu \rightarrow e^- + h^+ \qquad (12)$$

$$e^- + Ti^{4+} \rightarrow Ti^{3+} \qquad (13)$$

$$h^+ + O^{2-} \rightarrow O^- \qquad (14a)$$

$$O^- + H_2 \rightarrow OH^- + H^\bullet \qquad (14b)$$

$$H^\bullet + Ti^{4+}\, O^{2-} \rightarrow Ti^{3+} + OH^- \qquad (14c)$$

By irradiation under H_2, the holes reacts with hydrogen forming Ti^{3+} centers so that no more recombination is possible, as shown by the fact that, upon thaw−freeze treatment, the EPR spectrum remains unaffected (Figure 30d).

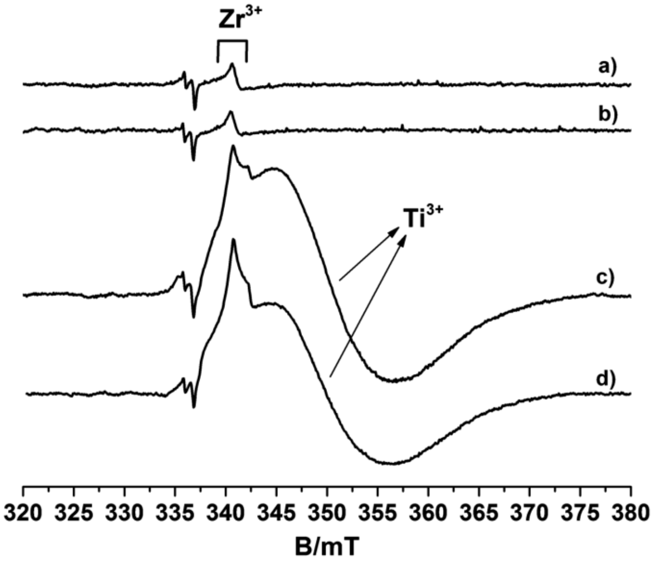

Figure 30. EPR spectra of ZT sample irradiated in H_2 atmosphere: (a) activated sample in dark; (b) same sample contacted with 50 mbar of H_2; (c) sample in (b) upon irradiation with UV−Visible light at 77 K; (d) sample after a thaw-freeze treatment (lamp off, heating at RT and cooling again at 77 K). All the spectra were recorded at 77 K and with a microwave power of 10 mW.

1.1.5. DFT calculations.

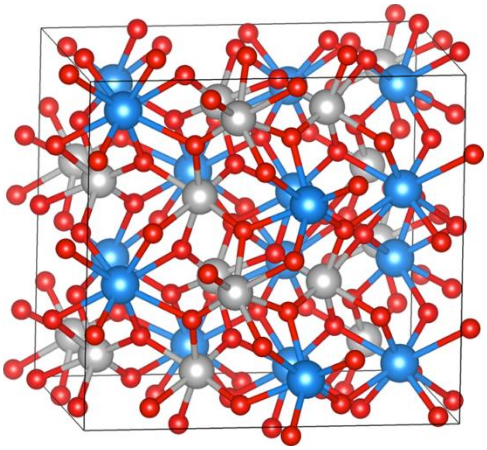

Figure 31. 2x2x2 Supercell of $ZrTiO_4$ optimized structures. Ti atoms are in gray, Zr in light blue and O in red.

DFT calculation were performed in collaboration with the group of Prof. G. Pacchioni. The main results are summarized in this section. For more details see reference 184.

Geometrical and Electronic Structure. Different $ZrTiO_4$ geometrical configurations have been taken into account but the more stable and more similar to the experimental one has resulted that containing dispersed Ti and Zr ions in the octahedral sites without any segregation of Zr and Ti atoms (Table 2 and Figure 31).

Different O sites have been generated depending on their first neighbors. Most of the oxygen atoms results three coordinated (O_{3c}) but the O_{3c} directly bound to three Zr ions change their coordination sphere by attracting a nearby Ti ion and thus forming a distorted tetrahedron O_{4c} (Figure 32).

	a		**b**		**c**		**E_g (eV)**
ZrO_2	5.240		5.265		5.417		5.73
TiO_2	3.789		3.789		9.776		3.87
	a	**Δ%**	**b**	**Δ%**	**c**	**Δ%**	**E_g (eV)**
Expt $ZrTiO_4$	4.807		5.479		5.034		3.8
Calc $ZrTiO_4$	4.860	+1.1	5.515	+0.7	5.078	+0.9	4.76

Table 2. Mean cell parameters (Å), differences (Δ%) with respect to the experimental values,[73] and minimum band gap of TiO_2 anatase, monoclinic ZrO_2 and of experimental and calculated $ZrTiO_4$

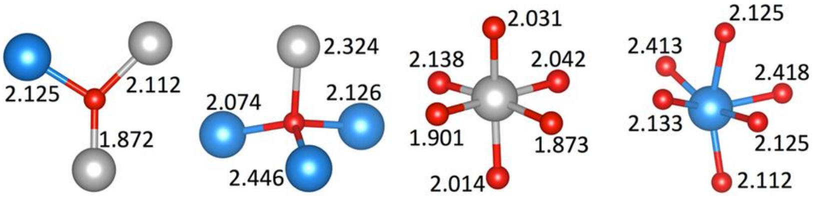

Figure 32. Local structural features of simulated $ZrTiO_4$ structure, where gray represents Ti atoms, light blue Zr, and red O.

Figure 33 shows the projected density of states (PDOS) of $ZrTiO_4$. As expected, the top of the valence band (VB) is characterized by O 2p states, whereas the bottom of the conducting band (CB) is characterized by the empty Ti 3d states. It is worthwhile to note that the Ti 3d states lie at lower energy than the Zr 4d states.

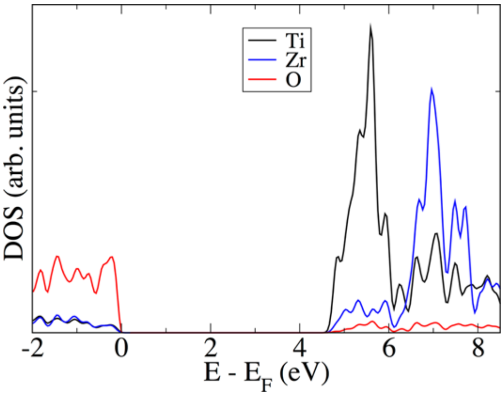

Figure 33. PDOS of $ZrTiO_4$. O contribution to the DOS is represented in red, Ti contribution in black, and Zr contribution in blue. The Fermi level is set to the top of the valence band.

The experimental band gap (E_g = 3.8 eV) is 18% larger than that of TiO_2 (3.2 eV, Table 2). The computed E_g for $ZrTiO_4$, 4.76 eV, is 23% larger than that of anatase TiO_2 computed at the same computational level, E_g = 3.87 eV (Table 2). The overestimation of the calculated $ZrTiO_4$ band gap is related to the Ti component, whose computed 3d empty states lie at relatively high energies due to structural effects. The absolute value is too large due to the fact that the B3LYP functional tends, as in the case of TiO_2, to overestimate the band gap (by about 21% in the case of TiO_2, Table 2). If this correction is applied and the computed band gap of $ZrTiO_4$ is reduced by 21%, the value of 3.8 eV is obtained, that exactly matches with the measured E_g. In conclusion, in $ZrTiO_4$, the nature of VB and of the bottom of CB is very similar to that of TiO_2 and the small increase of the band gap is due to geometrical effects that lead to a widening of the gap.

Oxygen Vacancy. The nature of the oxygen vacancies (V_O) and the fate of the two electrons left in the solid when the vacancy is created after thermal annealing of the material have been investigated by simulating several $ZrTiO_{4-x}$ defective structures. Different V_{O3c} and V_{O4c} have been modeled and three situations have been found. The lowest in energy corresponds to two excess electrons localized on Ti ions (triplet state). The other two configurations, higher in energy, are (i) one with one electron on Ti and one on Zr (triplet state), and (ii) one with two electrons trapped in the cavity (singlet state). It can be concluded that the defective $ZrTiO_{4-x}$ behaves like TiO_{2-x}, with reduction of the Ti ions and formation of Ti^{3+} species.

1.1.6. Conclusions.

In this part of PhD work the zirconium titanate ($ZrTiO_4$) system, that could be considered the first type of TiO_2 modification, has been investigated. This solid, indeed, introduces an elevated concentration of tetravalent zirconium ions in a TiO_2-like matrix being based on linked MeO_6 octahedrons (Me = Zr, Ti) with three coordinated oxygen ions at the connection (scrutinyite structure).

$ZrTiO_4$ nanocrystals have been prepared via sol-gel method and show an optical band gap of 3.8 eV. This experimental value perfectly matches with that extract from the DFT calculations. Furthermore it was demonstrated (with both calculations and UPS valence band measurements) that $ZrTiO_4$ exhibits an increment of the reductive potential of conduction band electrons with respect to TiO_2.

Upon thermal annealing in vacuum zirconium titanate behaves more similarly to ZrO_2 (i.e. reluctant to the reduction) in weak and mild annealing conditions, whereas its resistance to reduction decreases at $T > 673$ K when it behaves like TiO_2 forming important amounts of surface Ti^{3+} ions. The behavior of $ZrTiO_4$ upon annealing at high temperature is due to the presence of tetravalent Ti ions, which are better electron traps than the Zr ions since their electronic energy is lower. The computational results nicely fit with the experimental observations explaining the initial resistance to oxygen loss in terms of the formation cost of an oxygen vacancy that, in $ZrTiO_4$, is 1.5 eV higher than in TiO_2. The formation of Ti^{3+} upon annealing at higher temperature is also confirmed by calculations that indicate that, after O extraction, the most stable solution is that with two electrons on two distinct titanium ions.

Under UV-Visible irradiation $ZrTiO_4$ easily undergoes a charge separation and the photogenerated charge carriers easily reach the surface and react with molecules in the gas phase, similarly to what occurs in the case of titania. For this reason zirconium titanate is an oxide that could be potentially useful in photocatalysis. In particular, since its conduction band potential is more negative than that of anatase and thus a higher reductive potential of photoexcited electrons is expected, this material could be considered a possible candidate for hydrogen evolution via water photoreduction.

1.2. Nitrogen doped- $ZrTiO_4$.

1.2.1. Structural, morphological and optical characterizations.

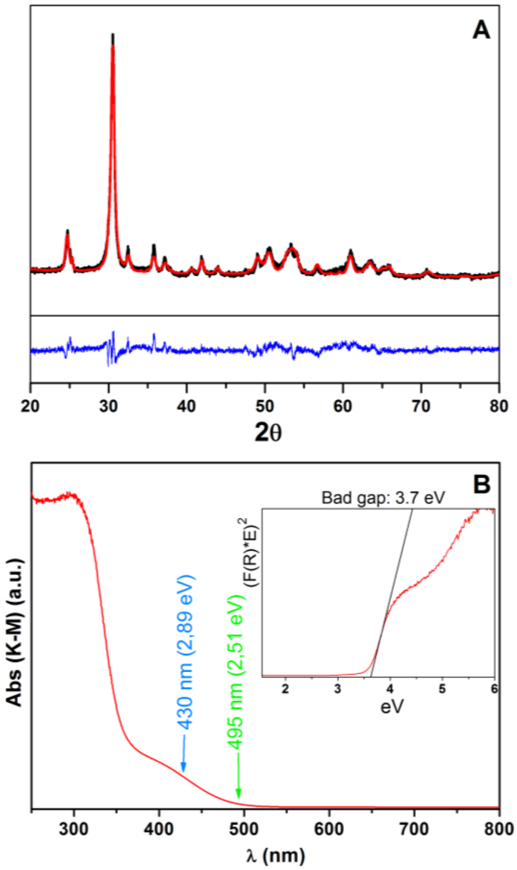

Figure 34. Panel A: XRD pattern of a N-ZT sample. Black line: experimental trace. Red line: computer simulation obtained by Rietveld refinement. Blue line: difference between experimental simulated patterns. Panel B: UV-Visible diffuse reflectance spectrum of a N-ZT sample. In the inset the Tauc's plot is reported.

The XRD diffractogram of N-doped $ZrTiO_4$ (N-ZT) sample, with the corresponding computer simulation are reported in Figure 34A. The Rietveld refinement of the XRD pattern shows the formation of crystals of $ZrTiO_4$ beside a small fraction of anatase (ca. 2%) and of tetragonal ZrO_2 (ca. 1.3%). The powder exhibits a specific surface area around 12 m^2g^{-1}, hence the different synthetic method with respect to that adopted for the pristine material leads to the formation of bigger particles (see Table 3) and thus to a lower surface area with respect to the undoped ZT.

Figure 34B reports the UV-Visible absorption of N-ZT sample. The characteristic absorption edge in the UV region, due to the electron transfer from the valence band to the conduction band is observed. The optical band gap absorption obtained by the Tauc plot (Table 3) indicates that the optical band gap of the N-ZT sample is slightly lower than that of the undoped ZT material. Assuming a direct transition as in the case of pristine ZT, the band gap energy (E_g) measured by the Tauc's plot method is, in fact, 3.7 eV. This difference is not due to the presence of nitrogen but is likely the result of the different synthetic route that brings about the formation of bigger particles (Table 3). Indeed the band gap energy measured by Tauc's plot of a zirconium titanate sample, prepared with the same synthetic method of N-ZT sample without the nitrogen source, is again 3.7 eV (Table 3). This phenomena could be related to some limitations resulting from the approximation of the Kubelka-Munk method that allow to convert reflectance measures into the equivalent absorbance spectra. This approximation depends on the absorption and scattering coefficients that in turn depends on the particles size. The comparison between solids with different particles size (Table 3) and, in particular, between samples with size particles heterogeneity is rather complex.[185-186]

Beside this effect, the optical properties of the N-ZT material differ from those of the bare zirconium titanate especially for the broad absorption shoulder in the visible region centered at about 430 nm. The optical features reported in Figure 34B are similar to that of nitrogen doped TiO_2 materials in which the doping procedure introduces intra-band gap states that cause light absorption in the visible wavelength range.[12]

	Particles size (nm)	**Surface area (m^2/g)**	**E_g (eV)**
ZT1	15	66	3.8
ZT2	50-200	12	3.7
N-ZT	50-200	11	3.7

Table 3. Particles size, specific surface area and band gap energy of different sample: ZT1 is the pristine ZT prepared with the method reported in section 1.1. ZT2 is the pristine ZT prepared with the same synthetic method of N-ZT.

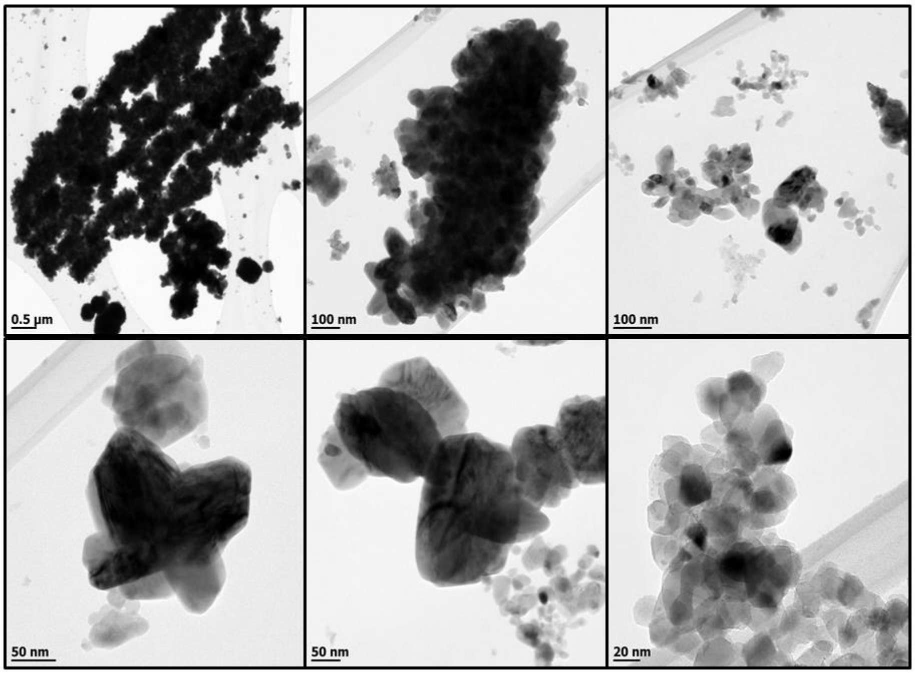

Figure 35. TEM images of N-ZT sample.

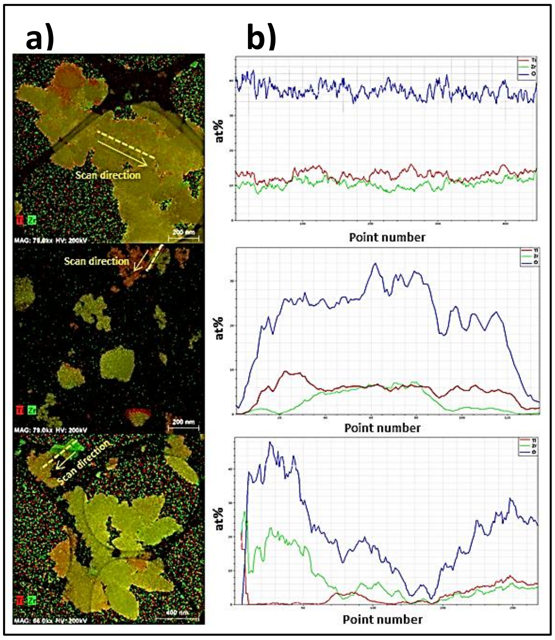

Figure 36. EDX maps of N-ZT. (a) line profile across the N-ZT aggregates and (b) the corresponding variation of the composition. Ti (red), Zr (green), O (blue).

The TEM images of the N-ZT sample, reported in Figure 35, indicate that, at variance of the ZT sample, this material exhibits a high heterogeneity from the point of view of the morphology. The particles are different in size, from 50 nm to 200 nm, and form big aggregates.

Furthermore they present different shape with cross, cubic and spherical aspect.

The EDX maps reported in

Figure 36 show that in most part of the sample the chemical composition is homogeneous with the expected spatial dispersion of Zr, Ti and O atoms. However in some parts, the stoichiometry is not respected and some segregation of titanium dioxide and zirconium dioxide are observable in agreement with the XRD evidences (Figure 34A).

Again the differences of this oxide with respect to the pristine ZT sample (described in the previous section), in terms of composition and morphology, is not due to the presence of nitrogen but, rather, to the different synthesis method used for N-ZT samples preparation. This synthetic method lead to big particles with high heterogeneity of shape and composition, however this type of preparation was the only that allowed the doping process.

1.2.2. EPR characterization of N center.

The presence of nitrogen in the N-ZT sample was confirmed by EPR spectroscopy. The EPR spectra of the material were performed at two distinct frequencies, 9.5 GHz (X-band) and 35 GHz (Q-band) (Figure 37). The as-prepared material shows a relatively low intensity EPR signal. For this reason all the spectra reported in Figure 37 were recorded after visible light irradiation in order to increase the signal to noise ratio (see Section 1.2.3 for details) and to obtain a more reliable analysis. This paramagnetic defect is certainly amenable to nitrogen atoms since the spectra of the materials containing N in natural abundance (^{14}N-ZT) exhibit the typical three-line hyperfine structure (^{14}N has nuclear spin $I = 1$ and the EPR line multiplicity is $n = 2I+1 = 3$).

This is also confirmed by isotopic substitution with ^{15}N. In this case the signals change from three to two hyperfine lines according to the different nuclear spin of ^{15}N ($I=1/2$, $n=2$).

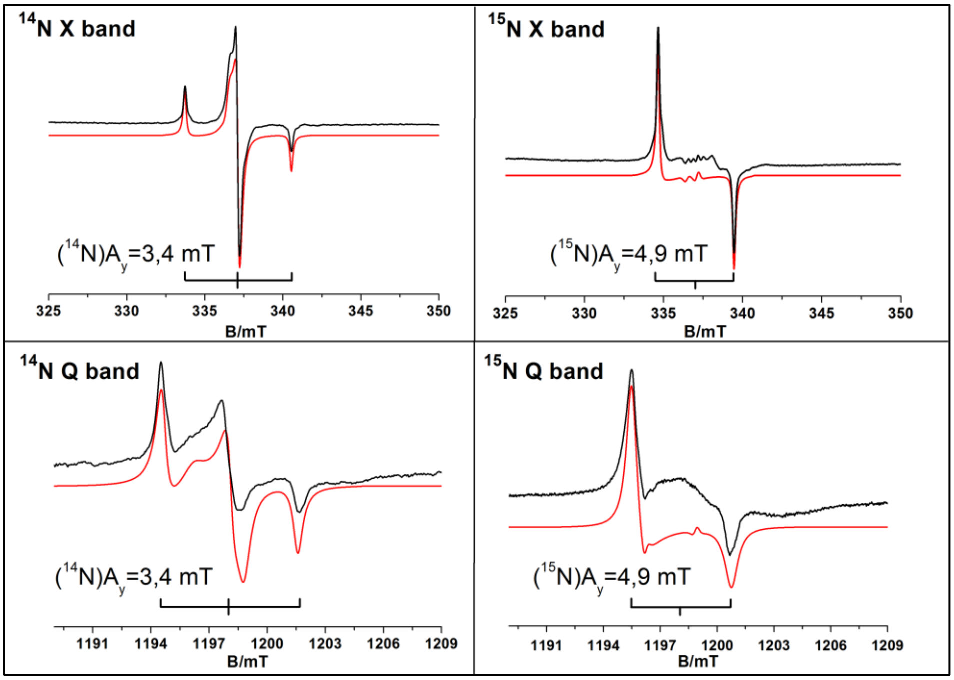

Figure 37. X and Q band experimental (black) and simulated (red) EPR spectra of ^{14}N-ZT and ^{15}N-ZT samples recorded at RT. All the spectra were recorded after irradiation with visible light (λ>420 nm) in order to get a better signal to noise ratio, as shown in the following Section (1.2.3).

The whole set of spectra reported in Figure 37 was simulated (red lines) on the basis of rhombic **g** and hyperfine **A** tensors having three *g* values very close to each other. The values of *g* and A tensor elements obtained by the simulation are reported in Table 4.

The use of a higher frequency (Q-band) has the aim of increasing the separation between the various *g* features while those due to the electron nucleus interaction (hyperfine structure) remain constant. The same set of spin-Hamiltonian parameters was used in the four simulations reported in Figure 37 just scaling the hyperfine coupling constant of the expected value passing from ^{14}N and ^{15}N which corresponds to the ratio of the two nuclear g_N factors of the two nuclei. The goodness of the fit between experimental and simulated spectra in the four distinct cases firmly indicates the quality of the obtained spin Hamiltonian parameters.

g tensor	^{14}N **A** tensor (mT)	**^{15}N A** tensor (mT)
$g_z = 2.0081 \pm 0.0001$	$A_z = 0.22 \pm 0.09$	$A_z = 0.32 \pm 0.09$
$g_y = 2.0046 \pm 0.0003$	$A_y = 3.40 \pm 0.06$	$A_y = 4.90 \pm 0.06$
$g_x = 2.0038 \pm 0.0002$	$A_x = 0.16 \pm 0.01$	$A_x = 0.26 \pm 0.01$

A_1	A_2	A_3	a_{iso}	T_1	T_2	T_3	ρ
±3.40	±0.22	±0.16	1.26	2.14	1.04	1.10	0.69

Table 4. **g** and hyperfine **A** tensors, ^{14}N hyperfine coupling constants (mT) and total spin density of the nitrogen center in $ZrTiO_4$ extracted by simulation of the experimental spectra.

The signal is characterized by a hyperfine coupling tensor mainly concentrated in one direction typical of a spin density localized in a directional (p-type) orbital. The spin density on the nitrogen atom of the N center can be derived from the hyperfine matrix **A** (Table 4) according to:

$$\mathrm{A} = \begin{vmatrix} A_1 & 0 & 0 \\ 0 & A_2 & 0 \\ 0 & 0 & A_3 \end{vmatrix} = a_{iso} + \begin{vmatrix} 2T & 0 & 0 \\ 0 & -T & 0 \\ 0 & 0 & -T \end{vmatrix} = 1.260 + \begin{vmatrix} 2.138 & 0 & 0 \\ 0 & -1.040 & 0 \\ 0 & 0 & -1.097 \end{vmatrix} \qquad (15)$$

where a_{iso} is the Fermi contact term (proportional to the 2s electron spin density in the nuclear volume) and **T** is the dipolar matrix having the typical form of the electron-nucleus dipolar interaction for an electron in a p orbital (i.e., $2T$, $-T$, $-T$). The spin density in the p orbital, ρ_{2p}, calculated by comparison of the experimental dipolar value with the corresponding atomic one ($\rho = T/T^{o}$) is $\rho_{2p} = 0.67$ ($T^{o} = 1.816$ mT (ref. 187)). The comparison of the isotropic Fermi contact term with the corresponding tabulated one indicates a further amount of electron spin density (0.020) in the 2s orbital of the nitrogen atom. The total spin density on the N atom of the observed species therefore amounts to 0.69, with the larger contribution being due to a single 2p orbital.

This analysis shows that the nitrogen hyperfine tensor does not cover for the whole unpaired electron spin density. Hence, a fraction of the spin density is likely localized on other nuclei having zero nuclear spin. This evidence suggests that the nitrogen containing species strongly interacts with the oxide matrix as it was found in the case of N-TiO_2.[188]

Comparing the EPR data of N-ZT with that of other nitrogen doped oxides it can be concluded that (i) in the N-ZT sample are not present diatomic N-species as reported for example in the case of N-MgO or N-ZnO.[108,189] (ii) The nitrogen paramagnetic center in $ZrTiO_4$, though similar, is not the same observed in TiO_2. In the case of ZT, in fact, the N hyperfine constant (hence the spin density) is higher than in the case of TiO_2.

For the sake of simplicity, hereafter the paramagnetic nitrogen species in zirconium titanate will be denoted as $N^•$.

In order to better understand the nature of N paramagnetic species some DFT calculations have been performed by the research group of Prof. G. Pacchioni.

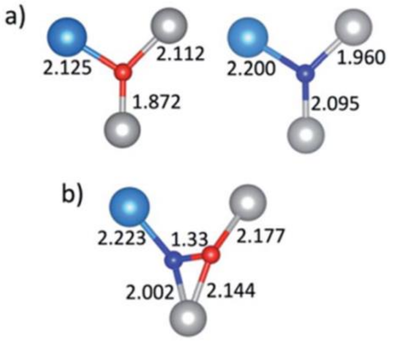

Figure 38. Local structural features of (a) pure $ZrTiO_4$ (left) and N_{sub}- $ZrTiO_4$ (right), (b) N_{int}- $ZrTiO_4$. Bond lengths are in Å. Zr atoms are represented in light blue, Ti in gray, O in red and N in blue.

The structure of N-$ZrTiO_4$ adopted for the calculation is that of $ZrTiO_4$ already described in Section 1.1.5. The $N^•$ dopant has been inserted as a substitute for O, N_{sub}, and as an interstitial, N_{int}. Several N_{sub} and N_{int} configurations have been modelled but the more stable have resulted that reported in (Figure 38) (see ref. 190 for more details).

The interstitial N dopants have been inserted in the middle of the cavities and forming a N–O species with an O atom.

In Figure 39 the total density of states of N and the neighboring Zr, Ti and O atoms of all the defective structures are reported. The N_{sub} dopant introduces a singly occupied N $2p_{\alpha}$ state, which lies just above the O 2p states. The corresponding empty $2p_{\beta}$ component (hole state) is fully localized and lies about 1.2 eV below the bottom of the conduction band (CB) (Figure 39a,b).

The interstitial dopant is associated with a NO p molecular orbital, as observed for other oxides.[12,112,181] Here, the spin density (ρ) is localized on the p system, thus reducing the localization on $N^{\bullet}$ from 0.9 (ρ in N_{sub}) to about 0.8 (Table 5). The presence of $NO^{\bullet}$ species introduces singly occupied NO π_{α}^{*} states, which lie above the top of the O 2p valence band (VB) by 1 eV and that are responsible of the EPR signals. The hole state is localized on the empty $NO^{\bullet}$ π_{β}^{*} 0.5 eV below the CB (Figure 39c,d).

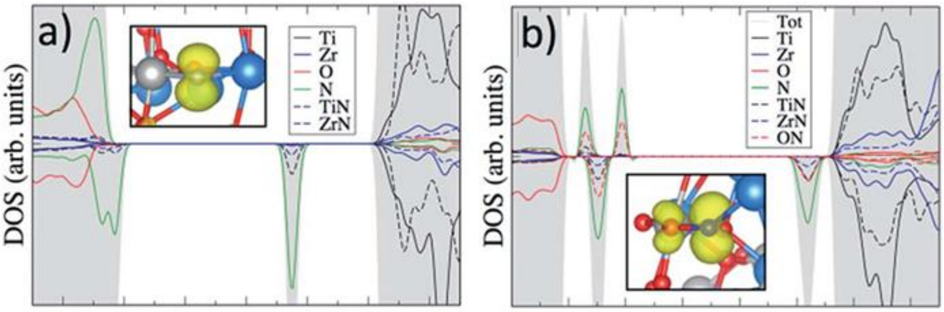

Figure 39. Total density of states (grey) and projected density of states of (a) N_{sub}-$ZrTiO_4$ and (b) N_{int}-$ZrTiO_4$. The Fermi energy is set to the highest occupied level. In the inset the spin density plots are reported.

Table 5 shows the hyperfine coupling constants (hfcc) for the N-doped ZT structures. The comparison between the substitutional and the interstitial hfcc shows small but significant differences in the **T** matrix and a_{iso} values and those of N_{int} are in better agreement with the experimental data. This seems sufficient to assign the N doped-$ZrTiO_4$ species to interstitial $N^{\bullet}$ dopants, that forms a N–$O^{\bullet}$ species with O lattice atoms.

	A_1	A_2	A_3	a_{iso}	T_1	T_2	T_3	ρ
Expt	**±3.40**	**±0.22**	**±0.16**	**1.26**	**2.14**	**1.04**	**1.10**	**0.69**
N_{sub}-$ZrTiO_4$	2.994	-0.684	-0.660	0.550	2.444	-1.234	-1.210	0.90
N_{int}-$ZrTiO_4$	**3.369**	**-0.358**	**-0.195**	**0.939**	**2.430**	**-1.296**	**-1.134**	**0.75**

Table 5. Computed and experimental ^{14}N hyperfine coupling constants (mT) and spin densities of all the defective structures.

1.2.3. Photosensitivity of the N$^{\bullet}$ center.

In order to investigate the role of the N containing species on the photoactivity of $ZrTiO_4$ material an EPR characterization of a N-ZT sample under different conditions of illumination has been performed.

As opposite to the pristine ZT material that can absorb only UV photons, the optical properties indicate that the N-ZT material also shows some visible light absorption. For this reason, it is important to monitor the effect of visible light irradiation.

Figure 40 reports the EPR intensity of signals of the N$^{\bullet}$ species upon polychromatic visible light irradiation (λ > 420 nm) in vacuum. Under irradiation the EPR signal of N$^{\bullet}$ rapidly grows by about one order of magnitude. When the irradiation source is turned off the signal intensity decreases (following

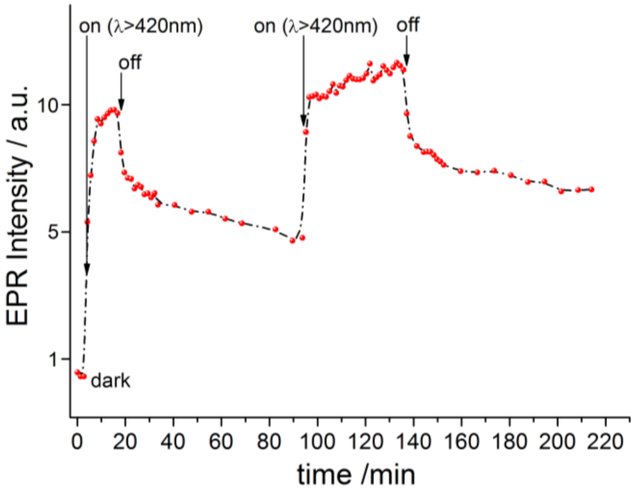

Figure 40. EPR signal intensity of N$^{\bullet}$ species under visible light irradiation (λ > 420 nm).

an apparent exponentially decay) without recovering, in a time interval of one hour, the initial intensity. The described behavior is reversible, and the signal grows when the light is turned on again.

The visible light ($E \leq 2.95$ eV) is ineffective on bare $ZrTiO_4$ and does not have sufficient energy to promote electrons from the valence band to the conduction band (3.8 eV). For this reason the behavior of the N-ZT under visible light irradiation has to be ascribed to the interaction of visible light photons with the electrons of the N intra band gap states. In more details the irradiation excites the electrons from the band gap state associated with the nitrogen impurity above the VB to the conduction band (CB). However, since the effect of the visible light absorption is a net increase of the EPR intensity of the paramagnetic $N^{\bullet}$ species, the operating mechanism at the origin of such a phenomenon has to involve a diamagnetic counterpart (N^{-}) of the $N^{\bullet}$ center. Indeed the selective irradiation depopulates the N^{-} centers causing the increase of the $N^{\bullet}$ EPR spectra (eqn 16)

$$N^{-}(\uparrow\downarrow) + h\nu(\text{vis.}) \rightarrow N^{\bullet}(\uparrow) + e^{-}(CB) \qquad (16)$$

When the irradiation source is turned off the recombination occurs (eqn 17):

$$N^{\bullet}(\uparrow) + e^{-}(CB) \rightarrow N^{-}(\uparrow\downarrow) \qquad (17)$$

The increase of $N^{\bullet}$ intensity upon irradiation can be explained by only assuming that N^{-} centers are more abundant than $N^{\bullet}$ ones.

It is also worth to note that after turning off the irradiation source, the intensity of $N^{\bullet}$ centers does not recover the initial value but remains higher than the starting one after at least an hour. Considering that no other paramagnetic centers are observed during the excitation and relaxation steps, this implies that a fraction of the photoexcited electrons do not relax recovering the starting situation and remain trapped, after irradiation, in some diamagnetic form and so EPR silent, similar to what occurs for EPR silent trapped electrons in the pristine ZT material. As predicted by the theoretical calculation in bare $ZrTiO_4$, most probably, these centers correspond to neutral vacancies V_O^x with two electrons trapped in the defects.

In order to better understand which component of the visible light spectrum is involved in $N^\bullet$ photoexcitation, irradiation experiments with monochromatic light have been also performed. Figure 41A shows the EPR spectra of a N-ZT sample recorded under irradiation with two different monochromatic wavelengths, in the green (495 nm) and in the blue (430 nm) region of the visible spectrum respectively (Figure 41A(a) and A(b)). The first wavelength corresponds to the tail of the absorption band in the visible region, while the second one corresponds to the maximum of this absorption (Figure 34B). The effect of the two monochromatic wavelengths is also compared with that caused by the irradiation with polychromatic visible light (λ > 420 nm) (Figure 41A(c)).

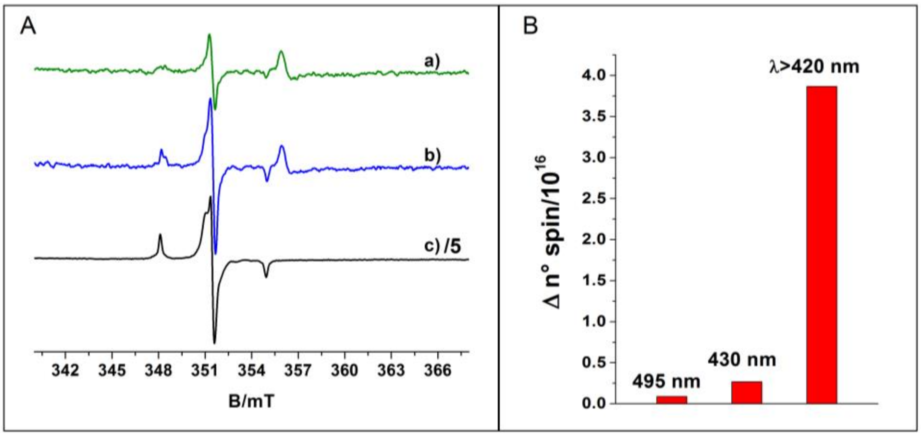

Figure 41. Panel A: EPR spectra of the N-ZT sample under different irradiation conditions: (a) irradiated with green light (λ = 495 nm), (b) irradiated with blue light (λ = 430 nm) and (c) irradiated with polychromatic visible light (λ > 420 nm). Spectra recorded at RT and with a microwave power of 1mW. Panel B: Spin counting (spins per gram) of the $N^\bullet$ species after 10 minutes of irradiation with different light sources. The irradiance is 0.6 W m^{-2} and >2000 W m^{-2} for monochromatic light (blue and green) and polychromatic light (λ > 420 nm) respectively.

The monochromatic irradiation was performed by applying a monochromator to the lamp obtaining an irradiance of 0.6 W m^{-2} in the two cases. In Figure 41B the spin count (number of spins per gram of material) under different irradiation conditions is also reported.

From inspection of Figure 41 the following facts emerge. (i) The green light irradiation causes only a poorly increase of the intensity of N$^{\bullet}$ species in comparison to what happens with blue light. This behavior is in agreement with the optical spectrum reported in Figure 34B where the maximum absorption occurs in the blue region. (ii) The largest growth in intensity of the N$^{\bullet}$ effect is observed when the sample is irradiated with polychromatic visible light. This latter fact is due to various reasons. First of all the irradiance of the whole lamp (λ > 420 nm) is much higher than that obtained using the monochromator. Second, the effect of the polychromatic light (that includes NIR frequencies) results in a complex mechanism of excitation of the electrons involving transitions from the valence band to nitrogen intra-band gap states, as already observed in similar cases.[12]

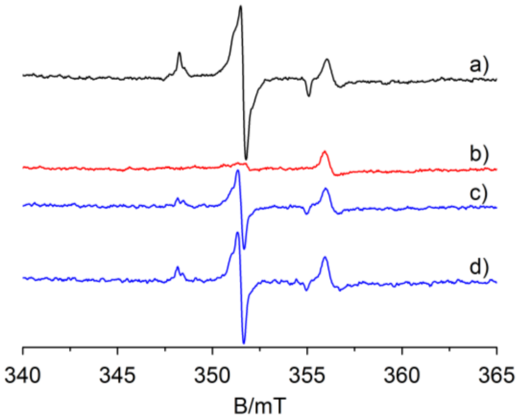

Figure 42. EPR spectra of the N-ZrTiO$_4$ sample. a) outgassed at RT. b) After annealing at 773K for 30 min. c) After oxidation at 773K for 60 min in 50 mbarr of O$_2$. d) After oxidation at 773K for 180 min in 50 mbar of O$_2$. Spectra recorded at RT and with a microwave power of 1mW.

The simultaneous presence of diamagnetic (N^{-}) and paramagnetic (N$^{\bullet}$) intra-band gap states is confirmed by thermal annealing under vacuum (773 K) and a reoxidation at the same temperature.

Figure 42 shows the effect of the thermal annealing in vacuum at 773K which causes a strong decrease of the EPR intensity of species $N^{\bullet}$ (Figure 42b). As previous results demonstrated, in this condition oxygen deplection occurs leaving two extra electrons per vacancy in the solid (see Section 1.1.3.). Extra electrons are thus localized on the nitrogen states, that lie at lower energy than that of Zr^{3+} or Ti^{3+}, reducing in this way the paramagnetic population in the solid. The whole process can be described by the equations 18 and 19.

$$ZrTiO_4 \rightarrow ZrTiO_{4-X} + \frac{X}{2} O_2 + xV_O^{\bullet\bullet} + 2e^- \qquad (18)$$

$$N^{\bullet}(\uparrow) + e^- \rightarrow N^-(\uparrow\downarrow) \qquad (19)$$

$$\frac{X}{2} O_2 + xV_O^{\bullet\bullet} + 2xN^-(\uparrow\downarrow) \rightarrow O^{2-} + N^{\bullet}(\uparrow) \qquad (20)$$

Reoxidation in oxygen inverts the phenomenon (eqn 20). Indeed, upon reoxidation at the same temperature, the EPR signal increases, although the initial intensity is not fully recovered (Figure 42c). This latter fact can be ascribed to the difficult oxidation of a low surface area material as in the case of N-ZT (12 m^2/g). Indeed, performing an oxidation for a longer time (Figure 42d) an higher increase of the EPR signal is achieved.

According to what was reported for other N-doped oxides, the N dopants in $ZrTiO_4$ matrix leads to a strong decrease of the cost of oxygen vacancy (V_O) formation (E_{form}). In this case the calculated E_{form} goes from 5.5 eV to 1.0 eV. This is related to the presence of N acceptor species that facilitates the formation of the oxygen vacancy. As a consequence, the two electrons associated with the V_O are transferred to two $N^{\bullet}$ states and their magnetic moment is completely quenched resulting in a diamagnetic center N^-. The corresponding N^- energy levels lie at about 0.45 eV above the top of the VB.

1.2.4. Charge transfer ability.

In order to understand if the electrons, that are promoted in the conduction band by the irradiation, are able to reach the surface and react, the EPR spectra of the sample were performed upon irradiation of the sample in oxygen atmosphere.

Surprisingly both irradiations with visible and UV-Visible light in O_2 atmosphere don't induce the formation of superoxide species, as contrariwise occurs in the case of the pristine ZT sample, but cause only the increase of the signal of $N^{\bullet}$ species as described in the previous experiments.

The same result was obtained if the irradiation of N-ZT sample were performed in H_2 atmosphere. In this case the absence of any reduced species (Ti^{3+} or Zr^{3+}) in EPR spectra recorded under both visible and UV-Visible irradiation clearly indicates that a hole transfer from the solid to the H_2 molecules doesn't occurs, as opposed to what happens in the case of pristine ZT.

These results indicate that N doped-$ZrTiO_4$, although it contains photosensitive nitrogen species, it is not able to transfer the photoformed charge carriers to molecules adsorbed on its surface. This behavior is unexpected and can be due to two different reasons: (i) The surface contamination by some byproducts of the synthesis that hampers the interaction with adsorbed species. This hypothesis, however, was excluded since an infra red investigation reveals that any impurities were not present on the surface of the material. (ii) The surface area that is too low to allow an efficient charge transfer from the bulk to the molecules adsorbed on the surface.

In order to clarify the role of the last possibility, the electron transfer capability of N-ZT was also tested on a thermally annealed (reduced) material in analogy with what done on ZT material (see Section 1.1.3 Figure 25). Three samples were used for this comparison: i) N-ZT (11 m^2/g), ii) the pristine ZT sample (ZT1) prepared by procedure described in Section 1.1 (high surface area, 66 m^2/g), iii) a pristine zirconium titanate (ZT2) prepared with the same method of N-ZT and thus with low surface area (12 m^2/g) (see Table 3).

Figure 43 reports the EPR spectra of the three samples upon thermal annealing (black spectra) and after contact with O_2 (red spectra).

The results can be summarized as follow: the annealed ZT1 (high area sample) is able to transfer electrons when contact with oxygen forming an intense signal of superoxide species as described in Section 1.1.3. (Figure 43C). On the contrary, the contact with O_2 with the annealed N-ZT and ZT2 (low area) samples doesn't cause neither the abatement of the signal of reduced species nor the formation of significant amount of superoxide species (Figure 43A and B). In the case of ZT2 the amount of $O_2^{\bullet-}$ is definitely lower with respect of the pristine ZT1.

This results clearly indicates that the electron transfer doesn't occurs in the case of low surface area samples (N-ZT and ZT2).

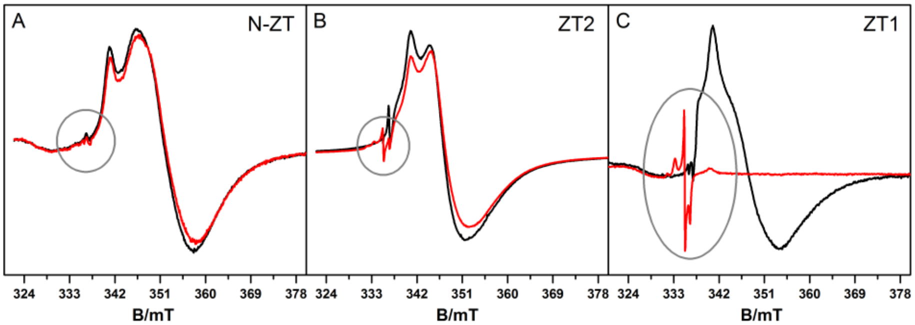

Figure 43. EPR spectra of N-ZT(A), pristine ZT with low surface area (B) and pristine ZT with high surface area (C). Black spectra: sample reduced at 873 K in vacuum. Red spectra: reduced sample after contact with 20 mbar of O_2 at room temperature (RT). All spectra were recorded at 77 K and with a microwave power of 10 mW and are normalized. The signal of superoxide species is highlighted by circles.

In other word, this experimental evidence seems suggests that the absence of electron transfer in the case of N-ZT sample is related to its low surface area rather than to the presence of N dopant.

1.2.5. Conclusions.

In this part of the work the N-doped $ZrTiO_4$ material has been synthesized and investigated. The resulting solid shows a yellow color and the presence of a paramagnetic defect, which is due to a nitrogen-containing species. By coupling DFT and EPR investigation, it has been possible to assign the observed paramagnetic nitrogen impurity to an interstitial form of nitrogen. In such defect, the nitrogen is bound to an O atom leading to a N–O species with an unpaired electron occupying a NO p-type localized orbital. These localized orbitals are positioned in the band gap of the material. In particular they lie above the valance band and explain the visible light absorption properties of the material. The N intra-band gap states can be either singly or doubly occupied with the formation, beside the paramagnetic species $N^{\bullet}$, of the corresponding diamagnetic counterpart (N^{-}). These latter states (N^{-}) are more than the paramagnetic ($N^{\bullet}$) ones. The electronic structure and the behavior of N-ZT sample is summarized in Figure 44.

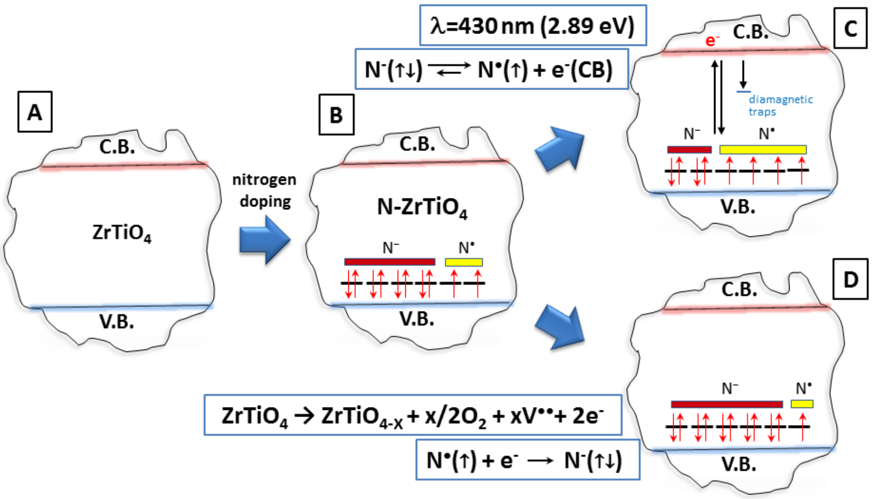

Figure 44. Proposed model for the description of the electronic and paramagnetic properties of N-doped $ZrTiO_4$. (A) electronic structure of bare $ZrTiO_4$. (B) Electronic structure of N-$ZrTiO_4$. (C) Effect of visible light irradiation on the paramagnetic population in the doped solid. (D) Effect of the thermal annealing in vacuum on the paramagnetic population in the doped solid.

Visible light irradiation affects the ratio between paramagnetic and diamagnetic population because electron excitation occurs from the more abundant doubly occupied states to the conduction band, increasing, in this way, the $N^{\bullet}$ states (Figure 44C). Conversely, when excess electrons in the solid are generated via oxygen depletion, they are trapped by the nitrogen states decreasing the paramagnetic population in the material (Figure 44D).The N doped $ZrTiO_4$ material, thus, is photosensitive to visible light which is suited to inject the electrons in the conduction band of the material. Unfortunately the low surface area of the material, prepared in this work, hampers the transfer of the charge carriers to molecules adsorbed on the surface making this material not yet suitable for photocatalytic application. At the moment my attempt to obtain high surface area sample had not success, nevertheless the preparation of a high surface area N-ZT sample could lead to interesting material for photocatalysis. For this reason further trials have to be performed.

1.3. Cerium doped - $ZrTiO_4$.

1.3.1. Structural, morphological and optical characterization.

XRD analysis was performed on the Ce doped-$ZrTiO_4$ powders (Cex-ZT where x is the Ce molar ratio) in comparison to that of pristine $ZrTiO_4$ (ZT) and the corresponding XRD patterns are reported in Figure 45A.

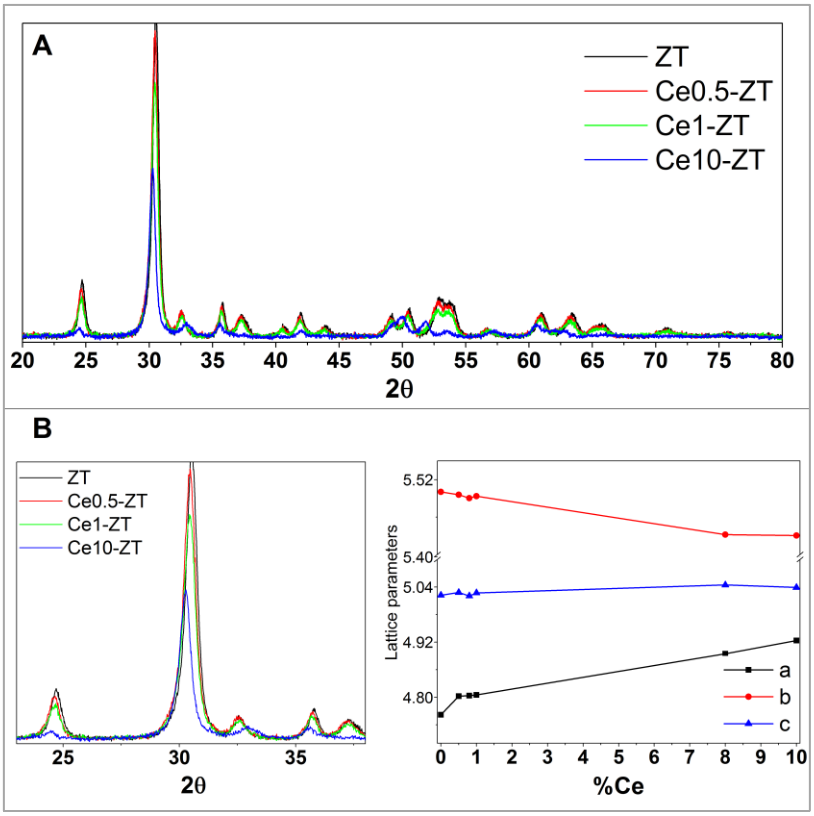

Figure 45. Panel A: XRD patterns of pristine ZT (black line), Ce0.5-ZT (red line), Ce1-ZT (green line) and Ce10-ZT (blue line). Panel B: On the left an enlargement of the XRD patterns reported in A. On the right the lattice parameters obtained from Rietveld refinement of XRD patterns of samples with different percentages of cerium in ZT matrix.

All the peaks of the diffraction pattern correspond to those of $ZrTiO_4$. No segregation of cerium oxide is observed even in the case of the sample with 10% of Ce. This, in principle, suggests that cerium ions are able to enter in the $ZrTiO_4$ matrix and form a solid solution. A further proof of this phenomenon is the progressive change of the lattice parameters obtained from a Rietveld refinement of the XRD patterns of the materials containing different amount of cerium (Figure 45B and Table 6). The higher the amount of cerium in the sample, the larger the lattice parameters deviation from that of the pure sample. This applies particularly for the parameters a and b.

This change of lattice parameter is confirmed by theoretical calculation (performed by the group of Prof. Pacchioni). In the structure of $ZrTiO_4$, modelled as in Section 1.1.5., a dopant percentage of 6.25% with respect to all the metal ions and of 12.5% with respect to Zr ions has been computed. In this model the Ce atoms were inserted both as substitutional to one Zr atom (Ce_{subZr}-$ZrTiO_4$) or substitutional to one Ti atom (Ce_{subTi}-$ZrTiO_4$). The percentage differences of the computed cell parameters (Å) with respect to that of calculated pure $ZrTiO_4$ (see Table 2) are reported in Table 6 and are compared with the difference between experimental lattice parameter of Ce-ZT and pristine ZT samples. The calculated values are strictly in accordance with the trend obtained for the experimental ones. To conclude, XRD and DFT calculation provide evidence about insertion of Ce in the lattice of zirconium titanate.

	ZT	**Ce0.5-ZT**	**Ce0.8-ZT**	**Ce1-ZT**	**Ce8-ZT**	**Ce10-ZT**
S_{BET} [m^2/g]	62	61	51	61	50	72
a [Å]	4.76187	4.80234	4.80376	4.80527	4.8947	4.92342
b [Å]	5.5005	5.496	5.49043	5.49343	5.43196	5.43035
c [Å]	5.02198	5.028	5.02202	5.02703	5.0443	5.03903

	Expt					**Calc (Ce6.25)**	
	Ce0.5	**Ce0.8**	**Ce1**	**Ce8**	**Ce10**	**Ce_{subZr}**	**Ce_{subTi}**
Δ%a	0.84	0.87	0.90	2.71	3.28	1.13	1.66
Δ%b	-0.08	-0.18	-0.13	-1.26	-1.29	-0.38	-0.26
Δ%c	0.12	0.01	0.10	0.44	0.34	0.11	0.88

Table 6. Top: BET surface area and lattice parameters (Å) obtained from Rietveld refinement of sample with different percentages of cerium. Bottom Expt: Measured cell parameters difference (Δ= Ce-ZT–ZT) of cerium doped materials compared to pristine zirconium titanate (expressed in %). Calc: Calculated cell parameter difference for a given cerium composition with respect to calculated pristine $ZrTiO_4$.

The specific surface area of the samples were measured by N_2 physisorption (B.E.T) and the values are reported in Table 6.

The samples exhibit specific surface area between 50 m^2/g and 70 m^2/g. The insertion of Ce atoms in the ZT matrix, thus, basically doesn't affect the specific surface area of the samples.

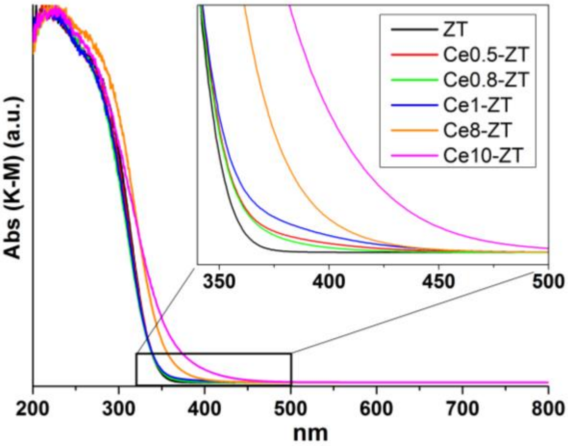

Figure 46. UV-Visible Diffuse Reflectance Spectra of Ce-ZT powders.

	E_g(eV)
ZT	3.8
Ce0.5-ZT	3.8
Ce0.8-ZT	3.8
Ce1-ZT	3.8
Ce8-ZT	3.7
Ce10-ZT	3.7

Table 7. Band gap energy of Ce-ZT samples

The optical absorption in the UV and visible region of Ce-ZT materials is shown in Figure 46 and the optical band gap energy evaluated by the Tauc's plot method for a direct transition of the Ce-ZT samples are reported in Table 7. For low amount of Ce (from 0.5% to 1%) the UV-Visible spectra differs from that of bare ZT sample only for a tail from 350 nm to 450 nm that lends a light yellow color of the powders. For higher loading (8%-10%) a small but appreciable red shift of the band gap with respect to the bare $ZrTiO_4$ is observable. Anyhow in all samples the energy edge remains in the UV region and the responsible of the yellow color of the solid is the tail in the visible region.

In order to have a more precise description of Ce-$ZrTiO_4$ systems and to understand the origin of the visible light optical absorption, the band structure of a Ce-$ZrTiO_4$ (6.25% atoms) system has been computed by the research group of prof. Pacchioni. As previously mentioned the Ce atoms were inserted both as substitutional for one Zr atom (Ce_{subZr}-$ZrTiO_4$) or substitutional for one Ti atom (Ce_{subTi}-$ZrTiO_4$). In both cases, the 4f empty states of cerium atoms lie very high in energy at about 0.5 eV below the conduction band, in the energy range of 4.1-4.4 eV (Figure 47). However, the calculated band gap of $ZrTiO_4$ is overestimated of about 21% (i.e. 0.9 eV, see Section 1.1.5.). Applying this correction, the empty 4f states result lowered and would lie at about 3.2-3.5 eV, according to what reported for Ce-ZrO_2 system.[123]

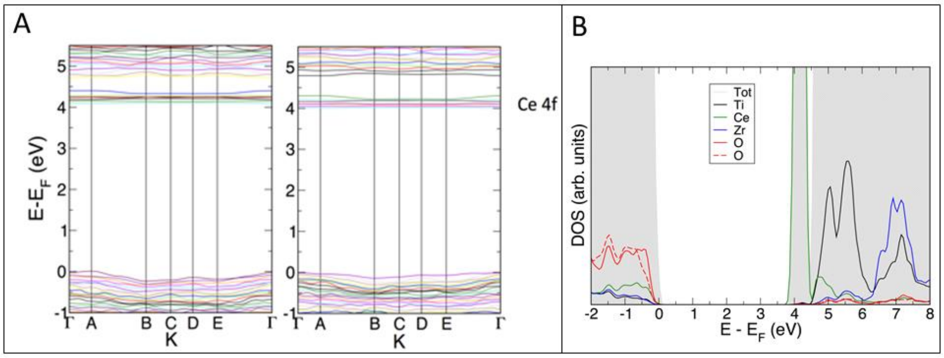

Figure 47. Panel A: Band structures of the Ce_{subZr}-$ZrTiO_4$ (left) and Ce_{subTi}-$ZrTiO_4$ (right). Panel B: TDOS and PDOS of Ce_{subZr}-$ZrTiO_4$ structure.

The results of this calculation do not allow to explain the optical absorption tail in the visible range. This computational approach, however, is not totally reliable if electronic transitions are involved. Hence, in order to obtain a more rigorous description of the band structure when electronic transitions are involved, the calculation of transition energy levels between different charge states for a defective system has been performed using the Charge Transition Levels method. Through this method it is possible to calculate with more accuracy the position of the defect levels generated by the optical excitation from the VB of the material and thus, in this case, the energy related to the transformation of a mid-gap Ce^{4+} ion to Ce^{3+}. The transition level $\varepsilon[(q+1)/q]$ is defined as the Fermi level for which the formation energies of defects in the charge states q+1 (in this case Ce^{4+}) and q (Ce^{3+}) are equal. For Ce_{subZr}-$ZrTiO_4$ (Figure 48) this transition, that involves the excitation of one electron from the VB to a Ce ion, occurs at 2.32 eV. This result is now in agreement with the experimental observed absorption in the visible range of the Ce doped materials.

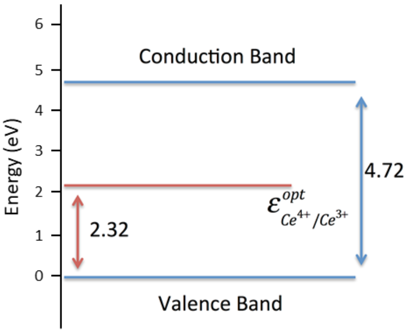

Figure 48. Optical transition levels for $ZrTiO_4$ systems doped with a single Ce atom. The position of Ce^{3+} states is reported.

The TEM images reported in Figure 49 illustrate the morphology of a Ce10-ZT sample. The particles are similar in terms of size and shape to that of pristine ZT (Figure 21). They present spherical aspect, slightly elongated in one direction and form big aggregates. The average particle size is about 15 nm.

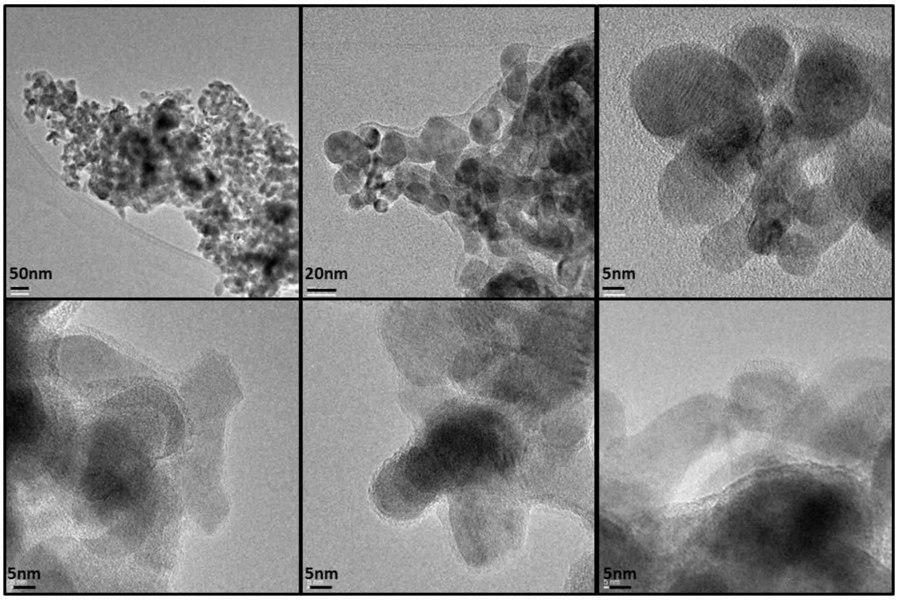

Figure 49. TEM images of Ce10-ZT sample.

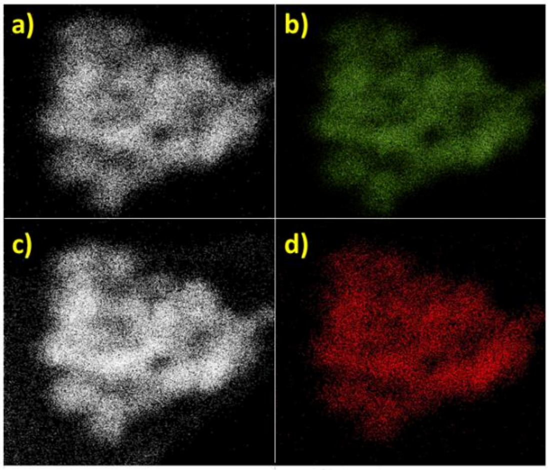

Figure 50. EDX maps of Ce10-ZT sample. Zirconium (a), Titanium (b), Oxygen (c) and Cerium (d) atoms distribution.

The EDX maps reported in Figure 50 show that the chemical composition is homogeneous in all parts of the Ce10-ZT sample that shows a good spatial dispersion of Zr, Ti, O and Ce atoms without segregation of single oxide phases (TiO_2, ZrO_2 or CeO_2). This evidence is a further confirmation of the insertion of cerium atoms in the ZT matrix.

1.3.2. Surface properties of Ce-$ZrTiO_4$: O_2 adsorption.

After an activation process performed in order to clean the surface and fully oxidize the sample (thermal reduction for 30 minutes at 573 K under vacuum followed by oxidation for one hour at the same temperature in O_2 atmosphere), the Ce0.5-ZT sample was investigated by EPR spectroscopy both in vacuum and under oxygen atmosphere. Surprisingly the EPR spectrum recorded in oxygen atmosphere at 77 K is not a flat line as expected for a fully oxidized sample but shows the presence of an intense EPR signal. Figure 51 reports the spectrum obtained for the Ce0.5-ZT sample under 2 mbar of O_2. This signal, observable for all Ce-ZT materials, is similar to that reported for the CeO_2/TiO_2 mixed oxides and assigned to superoxide O_2^- anions adsorbed on Ce^{4+} cations.[122,191] In other words the activated sample adsorbs oxygen in the form of superoxide.

The superoxide signal completely disappears removing the oxygen by pumping at room temperature and appears again if a new dose of oxygen is re-adsorbed. This indicates that oxygen is adsorbed forming superoxide species in a totally reversible way.

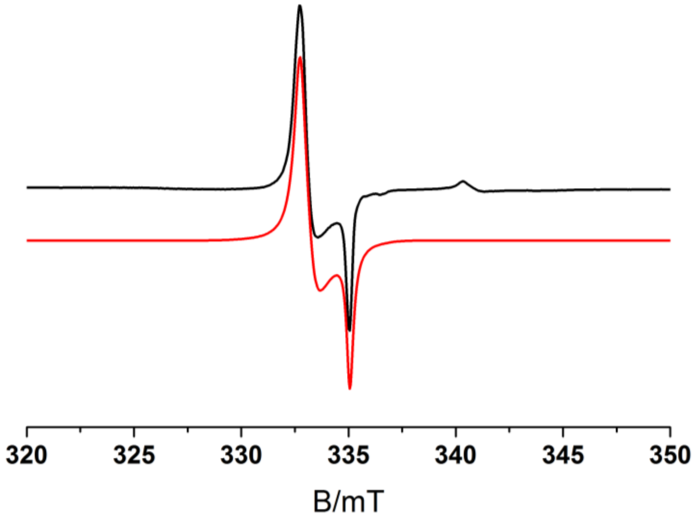

Figure 51. Experimental (black spectrum) and simulated (red spectrum) EPR spectra of Ce0.5-ZT contacted with O_2 after activation of the sample. Spectrum recorded at 77 K with a microwave power of 10 mW.

This peculiar reactivity must be related to the reversible transition of surface Ce ions from reduced (Ce^{3+}) to oxidized (Ce^{4+}) states. This hypothesis implies that Ce^{3+} centers are present at the surface even after the oxidative activation treatment. The observed phenomenon is described by equation 21 that outlines the existence of a (reversible) equilibrium at the solid/O_2 interface.

$$Ce^{3+} + O_{2\ (gas)} \leftrightarrows Ce^{4+}/O_2^{-} \qquad (21)$$

The experimental spectrum reported in Figure 51 was simulated using the following **g** tensor elements: g_z = 2.0256, g_y = 2.0229 and g_x = 2.0118. These *g* values are different from those observed in the case of superoxide on bare CeO_2 and recorded upon O_2 adsorption after thermal annealing ($g_{//}$ = 2.034 and $g_{\perp}$ = 2.010).[192] Moreover the formation of O_2^- on pre-reduced CeO_2 is not reversible at room temperature. In the case of Ce-$ZrTiO_4$, we are, thus, facing an original phenomenon that has been observed in few case only in the past and that could have interesting implications in term of catalytic properties of the system.

A further characterization of the reversibly adsorbed superoxide species at the Ce-$ZrTiO_4$ surface comes from the spectrum recorded using ^{17}O enriched oxygen. The hyperfine structure, due to the nuclear spin (I = 5/2) of the ^{17}O isotope, indeed, provides indications about the structure of the adsorbed O_2^- and about the spin density distribution. Figure 52 reports the spectrum obtained for the Ce0.5-ZT sample under 10^{-2} mbar of O_2 enriched with ^{17}O (99% atoms). The hyperfine structure, due to the prevailing presence of the ^{17}O–^{17}O isotopomer, is based on a 11-line structure centered at *g* = 2.0229 and separated by A_y = 7.6 mT (A_x and A_z are approximately zero). The structure of this signal clearly indicates the presence of two magnetically equivalent oxygen atoms in the superoxide species adsorbed on Ce^{4+}, thus, the O_2^- complex is a symmetric side-on adduct as reported in Figure 53.

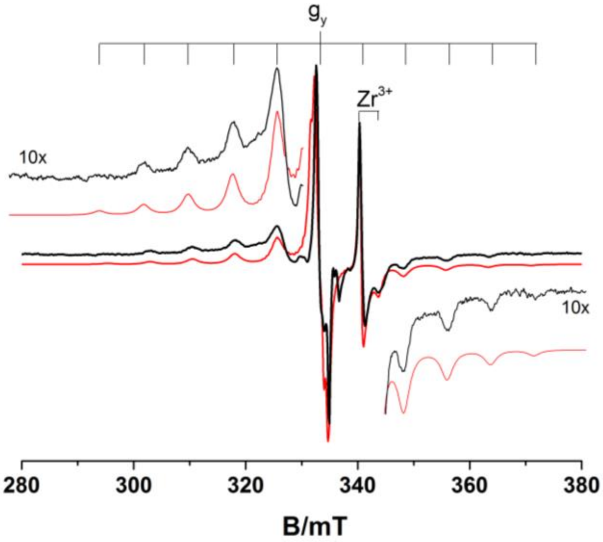

Figure 52. Experimental and simulated EPR spectra of Ce0.5-ZT sample contacted with $^{17}O_2$ (99% atoms).

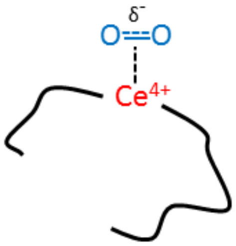

Figure 53. Side-on superoxide complex.

In order to understand the adsorption ability of the materials and to perform a quantitative analysis of the amount of adsorbed O_2^-, EPR spectra of Ce0.5-ZT and Ce10-ZT samples have been recorded using increasing oxygen pressure. The integrated area of each EPR signal has been compared with that of a standard solution of 2,2-Di(4-tert-octylphenyl)-1-picrylhydrazyl (DPPH) in cyclohexane in order to estimate the number of O_2^- radical ions adsorbed on the material. In Figure 54 the number of moles of adsorbed oxygen per gram of sample is reported as a function of oxygen pressure.

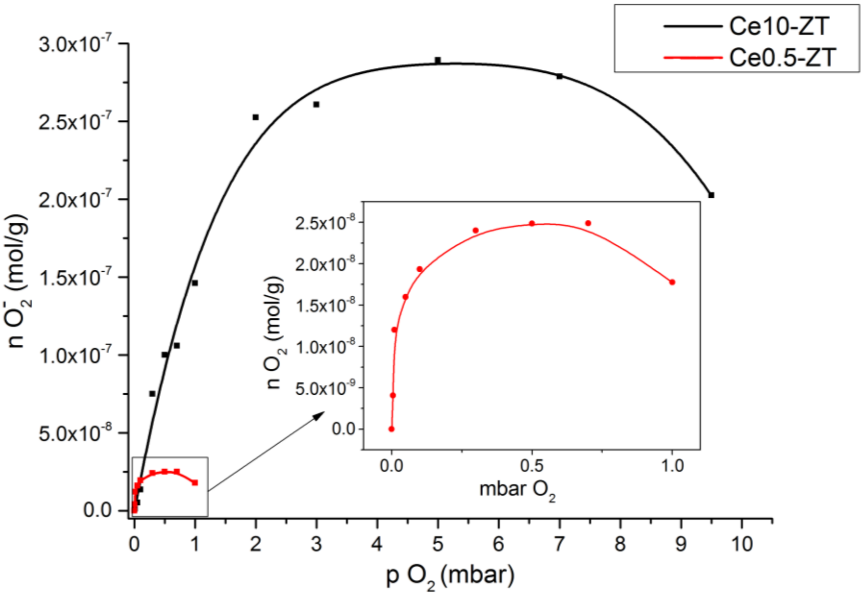

Figure 54. EPR-derived adsorption isotherms of O_2^- on Ce10-ZT (black line) and Ce0.5-ZT (red line) samples. The adsorbed amount has been evaluated via double integration of the superoxide EPR spectra.

Examining the results of Figure 54 (a sort of EPR-adsorption-isotherm) it shows up that in the case of Ce10-ZT the whole adsorption is almost ten times higher than that of Ce0.5-ZT, indicating that the amount of adsorbed oxygen is related to the amount of Ce atoms present in the material. In both samples the amount of adsorbed O_2 increases with increasing the oxygen pressure until reaching a plateau. After that the adsorbed amount apparently decreases since the EPR signal is affected by the dipolar broadening due to increased oxygen pressure. From this point the integration of the EPR signal is no longer representative of the true amount of adsorbed O_2.

The results obtained for Ce0.5-ZT reproduce a Langmuir adsorption model because they can be linearized using the equation (Figure 55):

$$\frac{p}{n} = \frac{1}{K_{eq} n_m} + \frac{p}{n_m} \quad (22)$$

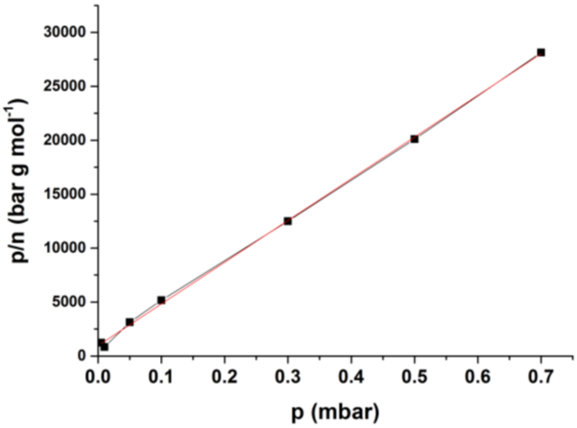

Figure 55. Linearization according to Langmuir isotherm of Ce0.5-ZT sample.

Where n_m is the number of moles adsorbed at full coverage, K_{eq} is the equilibrium constant, p is the pressure and n is the number of adsorbed moles.

From the linearization it is also possible to obtain the maximum amount of adsorbed oxygen on 1 g of sample (n_m) and the adsorption equilibrium constant (K_{eq}). In the case of Ce0.5-ZT sample these values are $n_m = 2.59 \cdot 10^{-8}$ mol and $K_{eq} = 40.4$ respectively.

The Gibbs free energy of formation using the equation 23 is -2.4 kJ/mol

$$\Delta G^0 = -RT\ln K_{eq} \quad (23)$$

The negative value of ΔG^0 confirms that the formation of superoxide species is a spontaneous process. Its low absolute value is in agreement with the reversibly of the phenomenon.

O_2 adsorption on Ce10-ZT doesn't follow a Langmuir adsorption model since its isotherm can't be linearized according to equation 22. Langmuir's model involves the presence of a unique family of isolated, non interacting adsorption sites. The non-Langmuir trend of the Ce10-ZT isotherm could be due to the presence of various families of sites (heterogeneity of the surface) and/or to the occurrence of interactions between the adsorbed molecules on Ce^{4+} sites.

1.3.3. Photoformation and reactivity of charge carriers followed by EPR.

Since the optical absorption spectra of Ce-ZT samples (Figure 46) show absorptions in the visible range, the effects of irradiation with both visible and UV-Visible light of Ce-ZT samples have been followed by EPR. Surprisingly, for all samples the visible (cut-off 400 nm) irradiation doesn't cause any change in the EPR spectra indicating that a charge separation in this conditions doesn't occurs. The results are not reported here for sake of brevity since the all spectra show no appreciable variation from the background. On the other hand, as in the case of bare ZT sample, the irradiation with UV-Visible of Ce-ZT samples causes a charge separation in the material.

Figure 56 reports the EPR spectra of Ce0.5-ZT irradiated with UV-Visible polychromatic light. The spectrum of the sample under vacuum in the dark (Figure 56a) exhibits the same feature of that of pristine ZT sample (Figure 28a), i.e. it contains tiny amount of Zr^{3+} defects already before irradiation. Upon UV-Visible irradiation (Figure 56b) on the right-hand side of the spectrum the signals of Zr^{3+} and Ti^{3+} increase indicating the trapping of photoexcited electrons. At lower field the signal belonging to trapped holes (O^- ions) arises.

After a thaw−freeze treatment (lamp off, heating at room temperature, and cooling again at 77 K) (Figure 56c), the majority of holes and electrons recombine since the spectrum is similar to that observed before irradiation, although a small fraction of holes are still appreciable. This behavior exactly reproduces that of pristine ZT sample.

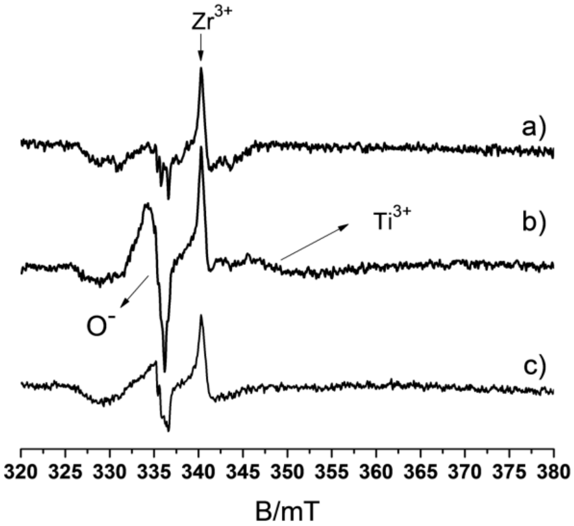

Figure 56. EPR spectra showing the effect of UV−Visible irradiation of Ce0.5-ZT in vacuum: (a) sample in the dark; (b) after UV−Visible irradiation; (c) sample after a thaw−freeze treatment (lamp off, heating at RT and cooling again at 77 K). All the spectra were recorded at 77 K and with a microwave power of 10 mW.

In conclusion the absorption tails in the visible region of the UV-Visible optical spectra are not sufficient to lead to a charge carriers separation. Nevertheless the photoformation of charge carriers upon UV-Visible light, typical of pristine ZT material, is maintained in Ce-ZT sample.

The reactivity at the surface of photogenerated electrons cannot be testes via EPR irradiating the samples in oxygen atmosphere because of the before described peculiar behavior of the Ce-ZT samples in presence of gaseous oxygen. The ability of surface hole transfer was, instead, tested via EPR upon irradiation in H_2 atmosphere (see Section 3.1. of Material and Method chapter for more details). While the visible irradiation doesn’t cause any change in the EPR spectra the effect on the EPR spectra of the UV-Visible irradiation in H_2 atmosphere of Ce0.5-ZT sample is reported in Figure 57. By irradiation under H_2 (Figure 57b),

Ti^{3+} and Zr^{3+} centers are formed by both electron trapping and hole reactivity so that no recombination can occur upon rising the temperature. Upon thaw−freeze treatment (Figure 57c), in fact, the spectrum in Figure 57b remains unaffected. This result reported for Ce0.5-ZT, and reproducible for all sample of Ce-ZT, indicates that the UV photogenerated holes are able to reach the surface of the materials and react with molecules adsorbed on the surface.

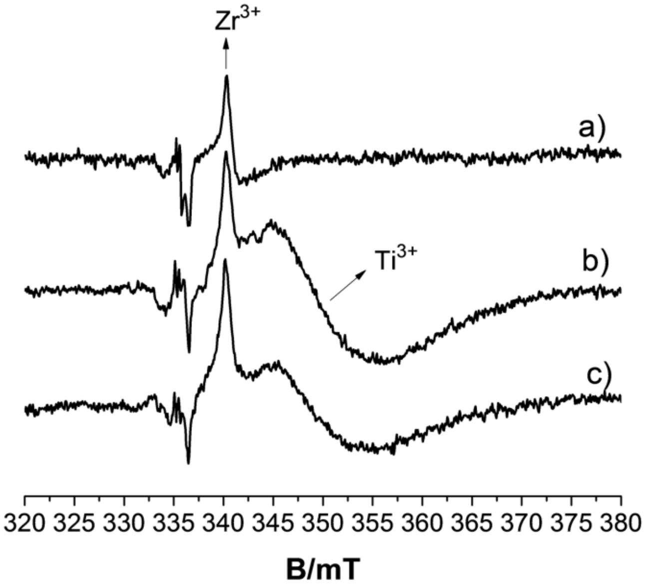

Figure 57. EPR spectra of Ce0.5-ZT sample irradiated in H_2 atmosphere: (a) sample in dark; (c) irradiated with UV−Visible light in H_2 atmosphere; (d) sample after a thaw-freeze treatment (lamp off, heating at RT and cooling again at 77 K). All the spectra were recorded at 77 K and with a microwave power of 10 mW.

1.3.4. Conclusions.

In this part of the work the Ce-doped $ZrTiO_4$ materials with different percentage of cerium atoms have been synthesized and investigated. The solids show yellow color. Combining XRD and DFT calculations it was possible to demonstrate that cerium ions can be inserted in the $ZrTiO_4$ matrix forming a solid solution as in the case of Ce doped-ZrO_2.[123] The presence of cerium in the structure of $ZrTiO_4$ causes the formation of intra band gap states that can localize electrons deriving from the VB of the solid and, thus, are responsible of the absorption in the visible range of the optical spectra (Figure 46). Surprisingly, all the Ce-ZT materials don’t present any activity under only visible light, but are photoactive upon UV-Visible irradiation only, as the pristine ZT material. The holes formed upon UV irradiation reach, at least in part, the surface and are reactive (irradiation under H_2). The same most likely occurs in the case of electrons but it could not in the case of electrons, but it could not be directly demonstrated due to a peculiar property of the material i.e. the direct electron transfer to oxygen in the dark. This property causes the formation of superoxide species in a reversible way by simply contact with oxygen. The reaction is pressure dependent and completely reversible indicating for this solid a behavior typical of an oxygen carrier. For this reason these materials could be in principle good candidates to be employed as oxygen sensors.

1.4. Photoformation of Reactive Oxygen Species (ROS) in solution.

In this section two tests of photoactivity on both pristine and doped ZT materials (ZT, N-ZT and Ce-ZT samples) are described. The photoactivity of these materials has been tested, in this case, following the formation of two different ROS in solution. To test the reductive ability of the solids, the superoxide formation in solution has been monitored following, via spectrophotometric method, the intensity of the absorption of the nitroblue tetrazolium molecules. On the other hand to monitor the oxidative ability, the formation of $OH^{\bullet}$ radicals has been followed by spin trapping technique using DMPO (5,5-dimethyl-pyrroline N-oxide) as spin trap. See Section 3.1 of Materials and Methods chapter for more information.

1.4.1. Superoxide by Nitroblue tetrazolium (NBT).

NBT molecule reacts with the photogenerated superoxide forming a precipitate. For this reason the decrease of absorption intensity of NBT solution, in the UV-Visible spectra, indicates the formation of superoxide species. The higher the absorption decrease, the higher the amount of photogenerated superoxide, thus, the higher the reductive capability of the photocatalyst (see Section 3.1. of Materials and Methods Section).

The test was performed irradiating the pristine and doped ZT samples in NBT solution with UV-Visible light and the results are reported in Figure 58.

It is worthy to note that the pristine ZT sample (Figure 58A(a) and B(a)) is active in the formation of superoxide species in solution upon UV-Visible irradiation. This result is in accordance to what has been observed irradiating the sample in oxygen atmosphere (Section 1.1.4.).

Concerning the N-doped ZT sample (Figure 58A(c)), its photoactivity results definitely lower than that of pristine ZT sample (Figure 58A(a)). However, as previously discussed, this decreased activity seems not due to the presence of nitrogen but, rather, to the low surface area of the sample as indicated by the similar result obtained for a pristine ZT sample prepared with the same method of N-ZT (Figure 58A(b)).

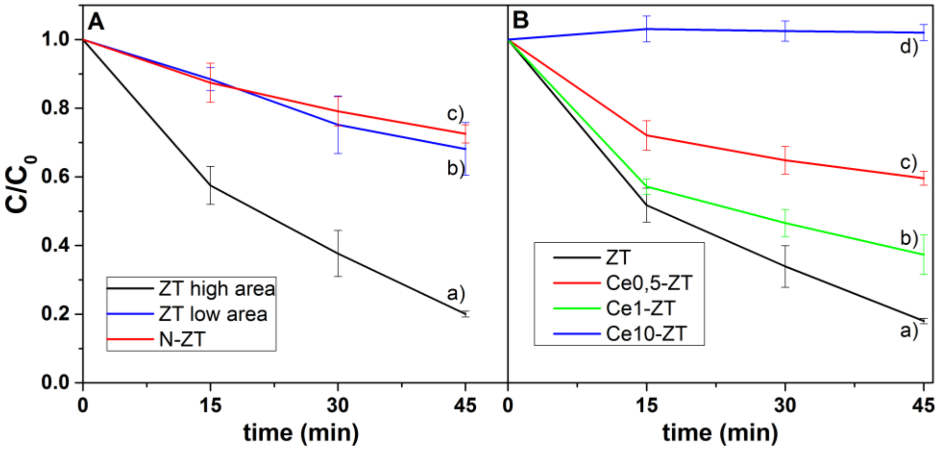

Figure 58. Absorption intensity of NBT upon UV-Visible irradiation of different samples. Panel A: pristine ZT with high surface area (a), pristine ZT prepared with the same synthetic method of N-ZT and exhibiting low surface area (b) and N-ZT (c). Panel B: pristine ZT (a), Ce0.5-ZT (c), Ce1-ZT (b) and Ce10-ZT (d) samples.

As far as the photoactivity of Ce doped ZT samples is concerned (Figure 58B), the presence of cerium atoms in the ZT matrix causes a decrease in the reductive ability with respect to the pristine ZT material under UV-Visible irradiation. In particular Ce1-ZT sample (Figure 58B(b)) is slightly more active than Ce0.5-ZT (Figure 58B(c)) in the formation of superoxide species, but anyhow it remains less active than that of pristine ZT (Figure 58B(a)). Furthermore in presence of a high concentration of cerium, as in case of Ce10-ZT (Figure 58B(d)), the photoformation of superoxide is totally suppressed. A possible explanation of this behavior is that the infra band gap states, related to cerium doping, act as traps of photoexcited electrons generated by UV light which are no more available for reduction reactions.

1.4.2. $OH^{\bullet}$ by Spin trapping technique (DMPO).

As described in Material and Methods chapter, the formation of $OH^{\bullet}$ radicals under irradiation is an indirect evidence of the oxidative ability of the photocatalyst, since hydroxyl radicals arise from the reaction between photoformed holes and water. In order to detect by EPR spectroscopy the $OH^{\bullet}$ radicals, the spin trap DMPO molecule is needed and the intensity of the DMPO/$OH^{\bullet}$ adduct EPR signal is proportional to the amount of photoformed $OH^{\bullet}$ radicals.

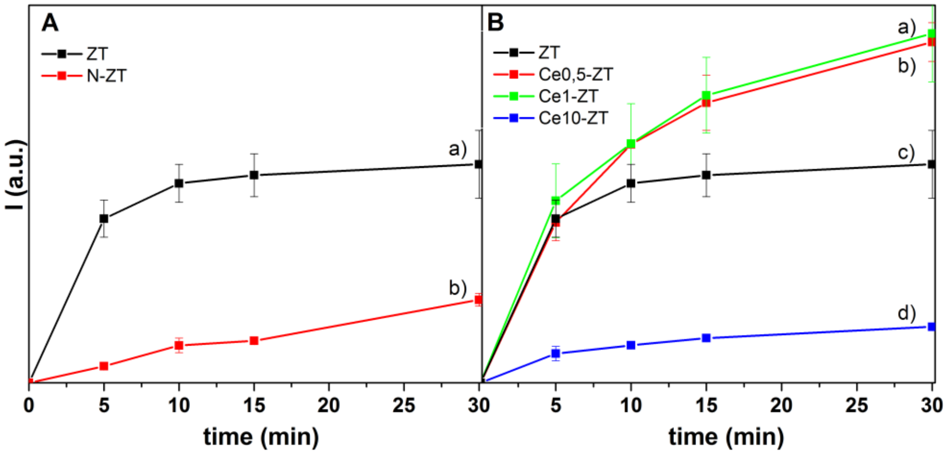

Figure 59. EPR intensity of the spectra of the DMPO/$OH^{\bullet}$ adduct produced by irradiation of a water suspension of different samples with UV-Visible light. Panel A: pristine ZT (a) and N-ZT (b). Panel B: Ce0.5-ZT (a), Ce1-ZT (b), pristine ZT (c) and Ce10-ZT (d) samples.

The EPR intensities of the DMPO/$OH^{\bullet}$ adduct formed upon UV-Visible irradiation of doped and un-doped ZT materials are reported in Figure 59. In the case of N-ZT (Figure 59A) the result strictly reproduces those of previous experiment, namely N-ZT sample exhibits lower photoactivity with respect to pristine ZT sample. It can be assumed that, also in this case, the cause of the decreased photoactivity is the low specific surface area of the doped sample that inhibits the transfer of the holes to the molecules adsorbed on its surface.

Concerning the Ce-doped material (Figure 59B), the results are slightly different with respect to those obtained for the photoformation of superoxide radicals. Also in this case, the Ce10-ZT exhibits lower photoactivity than that of pristine ZT. As opposite, the holes activity ($OH^{\bullet}$ formation) of Ce0.5-ZT and Ce1-ZT samples is increased with respect to that of pristine ZT.

This behavior could be explained considering that the Ce^{4+} 4f empty states, that lie into the band gap of the materials, can act as electron traps. Therefore, for low amount of Ce atoms, the recombination between photogenerated holes and electrons is reduced. The holes, in this way, have an enhanced lifetime and, thus, exhibit high reactivity. However, increasing the amount of Ce atoms in the material and, thus, the 4f states into the band gap, the recombination process prevail, reducing the reactivity of both electrons and holes.

These last two experiments however are useful to demonstrate that the pristine zirconium titanate is active in both electrons and holes transfer under irradiation, though its activity is limited to the UV-Visible light and not observed using visible component only. This is an essential property for the application of this system in photocatalysis.

1.5. Conclusions on zirconium titanate systems.

In this Section of the thesis three different zirconium titanate based systems have been prepared and studied, namely pristine ZT, nitrogen doped-ZT (N-ZT) and cerium doped-ZT (Ce-ZT). Table 8 summarize the photoactivity of the different ZT systems under UV and visible light.

	Charge separation under vacuum		Surface reactivity in O_2 (e^-)		Surface reactivity in H_2 (h^+)		ROS generation in liquid phase (UV-Vis)	
	UV-Vis	vis	UV-Vis	vis	UV-Vis	vis	O_2^-	$OH^\bullet$
ZT	YES	NO	YES	NO	YES	NO	YES	YES
N-ZT	YES	YES	NO	NO	NO	NO	NO	NO
Ce-ZT	YES	NO	–	–	YES	NO	NO	Ce0.5-1 YES Ce10 NO

Table 8. Activity of different zirconium titanate systems under UV and visible light (λ>400nm)

Pristine zirconium titanate turned out to be an interesting material since it exhibits band potentials rather suitable to induce redox photochemical reactions. In particular its conduction band is more negative than that of titanium dioxide and thus a higher reductive potential of photoexcited electrons is expected. Furthermore it is active in generating charge carriers under UV-Visible irradiation and in transferring them to molecules adsorbed on its surface.

The purpose of doping zirconium titanate with heteroatoms would be that of improving the absorption of the material and its photoactivity in the visible range. Both kinds of doped materials, N-ZT and Ce-ZT, show absorption in the visible range of the optical spectra, indicating that the doping influences the optical properties of the pristine material.

In the case of N-ZT the shoulder absorption centered at 430 nm is due to the presence of nitrogen infra band gap states. These states make the N-ZT material photosensitive to some visible frequencies suited to promote electrons from the nitrogen states to the conduction band. The photoactivity of this material, however, is compromise by its low specific surface area that inhibits the transfer of the photogenerated charge transfer to any adsorbed molecules.

Concerning Ce-ZT materials the absorption tail present in the visible region of the optical spectra is due to the presence of Ce 4f states that lie into the band gap of the solids. However the visible light is not capable to induce any charge separation probably because of the recombination process. This result is somehow surprising in that, in the case of Ce doped zirconia, with a similar electron structure, a clear photoactivity in the visible is observed.[123] These Ce-ZT materials show some photoactivity under UV-Visible light only. The activity of Ce-ZT, in particular, is different in the case of reduction (e^-) or oxidation (h^+) reactions and depends on the cerium loading. In the case of reduction reaction (electron transfer to oxygen molecule), all Ce-ZT samples are less active than the pristine ZT sample. This result was also confirmed by hydrogen evolution tests, performed on Ce1-ZT sample under UV-Visible irradiation (performed as described in Section 2.2), in which the photoreduction of proton from water was not satisfactory.

Conversely the oxidative activity of the samples with lower amount of cerium results increased compared to that of pristine ZT, while is demolished in the case of samples with high concentration of dopant. It can be assumed, hence, that few infra band gap cerium states could act as electron traps increasing the hole reactivity, but, in presence of high amount of cerium states, the recombination process are enhanced.

Nevertheless all Ce-ZT samples show a peculiar property that is the formation of absorbed superoxide species in a reversible way by simply contact with oxygen (oxygen carrier activity).

Summarizing the doping of zirconium titanate has not provided any hints in the photoactivity under visible light. However the pristine zirconium titanate remains an interesting material because of its photoactivity under UV light. In addition, its band potentials positions are, theoretically, rather suitable for some redox reactions such as hydrogen evolution reaction (HER). For this reason zirconium titanate material, combined with other co-catalysts, have been employed, as reported in the next section, in HER under UV-Visible illumination.

2. Surface anchoring of (inorganic) hydrogen evolution co-catalysts (HEC) and hydrogen production.

Aim of this PhD project is to find new materials that, in principle, exhibit good reductive properties. For this reason, in the present section the hydrogen evolution tests performed on zirconium titanate and on titania, as reference, will be discussed. However, to test the activity of the various samples in H_2 photoproduction it is convenient to add a co-catalyst to facilitate the H_2 evolution reaction (HER) at the surface. Platinum, as a H_2 evolution co-catalyst, is a natural and well experimented choice for a preliminary investigation while for practical application the selection of different systems containing hearth abundant elements is mandatory. An alternative to platinum as HER co-catalyst, for example, can be represented by copper species. Talking about co-catalysts, in this case, could result ambiguous since copper species evolve during the photoreaction and are not directly involved in the HER. Anyhow the modification of the semiconductor surface with these species leads to an increasing of the semiconductor activity in HER [154,158,164] and thus such copper species can be assimilated to hydrogen evolution co-catalysts.

Therefore, in this part of the work, Pt nanoparticles or copper in different forms have been inserted at the surface of TiO_2 and $ZrTiO_4$ and the resulting materials have been tested in H_2 evolution. Platinum nanoparticles-oxide is a well-known system which provides the best performance in HER, for this reason the modification with platinum was used, in this work, as a comparison for the other modified systems.

In the following paragraphs the structural and optical characterization of the sample modified with Pt and copper, the photocatalytic H_2 evolution tests and a study under illumination of the copper modified samples will be reported.

2.1. Structural and optical characterization.

2.1.1. XRD and DRS characterization of Pt-modified samples.

In order to obtain a preliminarily HER test, the well know HEC constituted by the platinum nanoparticles has been interconnected to $ZrTiO_4$ and to TiO_2.

Figure 60 reports the XRD patterns and the diffuse reflectance UV-Visible spectra of Pt-T and Pt-ZT (where T and ZT represent TiO_2 and $ZrTiO_4$ respectively) in comparison to those of bare T and ZT.

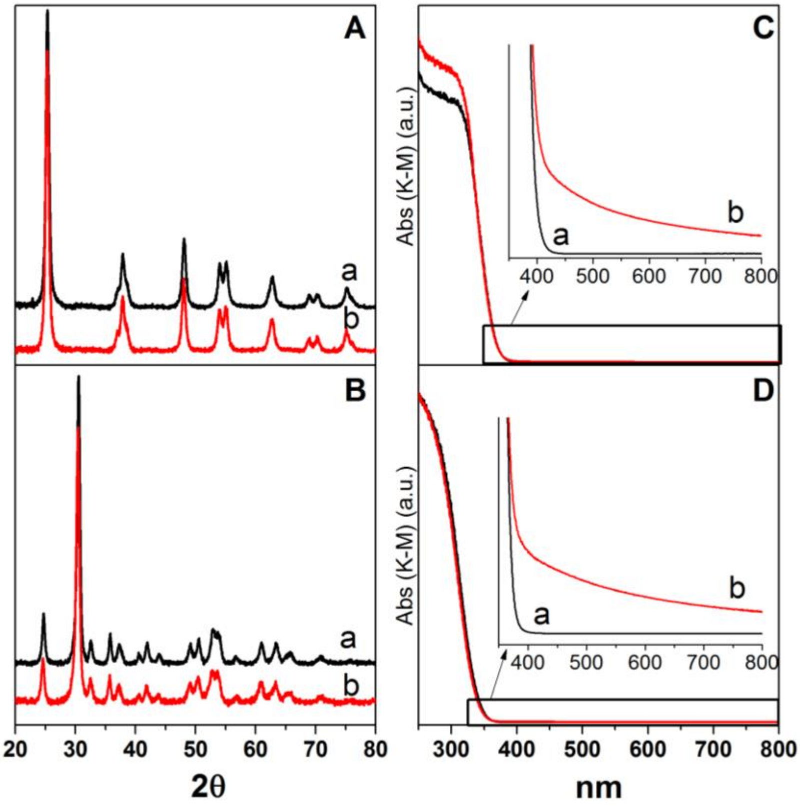

Figure 60. XRD diffractrogams (A and B) and diffuse reflectance UV-Visible spectra (C and D) of the bare oxides (a) and the corresponding Pt modified materials (b). Panels A and C: TiO_2 based samples. Panels B and D: $ZrTiO_4$ based samples.

Anchoring the Pt nanoparticles doesn't influence neither the XRD patterns (Figure 60A and B) nor the surface area of the oxides as indicated in Table 9. The crystallographic structure of the modified materials remains that of bare oxides namely anatase and scrutinyite $ZrTiO_4$ structure. Furthermore, all the XRD patterns don't show any peak ascribable to the Pt nanoparticles. The Dynamic Light Scattering technique reveals that Pt nanoparticles show an average hydrodynamic diameter of 10 nm.

The UV-visible reflectance spectra (Figure 60C and D) of the modified samples differ from those of bare ones only for the presence of an absorption in the whole visible region which is due to the plasmonic effect of the Pt nanoparticles.[193] The band gape edge in the UV region of the pristine oxides is preserved in the modified ones (see Table 9).

Sample	**Support Structure**	**B.E.T. Area (m^2/g)**	**E_g (eV)**
T	100% TiO_2 anatase	66	3.22
Pt-T	100% TiO_2 anatase	66	3.22
Cu^{2+}-T	100%TiO_2 anatase	59	3.21
Cu_2O-T	100%TiO_2 anatase	59	3.21
ZT	100% $ZrTiO_4$ scrutinyite	62	3.81
Pt-ZT	100% $ZrTiO_4$ scrutinyite	61	3.81
Cu^{2+}-ZT	100% $ZrTiO_4$ scrutinyite	58	3.82
Cu_2O-ZT	100% $ZrTiO_4$ scrutinyite	59	3.81

Table 9. Structure, BET specific surface area and energy gap values of TiO_2 and $ZrTiO_4$ modified with various HEC.

2.1.2. XRD, DRS and EPR characterization of Cu-modified samples.

In the last few years different forms of copper were found to be a valid alternative to platinum as HER co-catalyst.[21,24,153-154,160,164,194-195] Copper was thus inserted at the interface of TiO_2 (T) an zirconium titanate (ZT) in two different forms. The first type of material was prepared by a wet impregnation of the oxides starting from a $Cu(NO_3)_2$ solution followed by a calcination in air. In this case copper is mainly present as Cu^{2+} ions dispersed on the surface of the supporting oxide (TiO_2 or $ZrTiO_4$) even though it cannot be excluded the presence of a fraction of Cu^+ in the materials. These materials are labelled as Cu^{2+}-T and Cu^{2+}-ZT. The second type of material prevalently contains Cu_2O nanoparticles anchored on to TiO_2 or $ZrTiO_4$ prepared by a Cu(II) chemical reduction (benedict reaction leading to Cu_2O nanoparticles) followed by deposition on the supporting oxides. In this case the copper, therefore, is mainly in Cu(I) oxidation state. These material are labelled as Cu_2O-T and Cu_2O-ZT.

Figure 61 reports the XRD and the UV-Visible DRS characterization of the two set of Cu modified samples compared with the same data of the corresponding pristine materials. XRD diffractograms indicate that, for both oxidic supports (Figure 61A and B), the procedures adopted for the surface modification with copper do not alter the crystallographic features of the oxide. Also the surface area is not affected by the two modification procedures (Table 9).

It is worth to note that the presence of the additional fraction of copper species can be detected by XRD technique in the case of the materials decorated with the Cu_2O particles only. Both Cu_2O-T and Cu_2O-ZT samples, indeed, show a very weak additional diffraction peak at about $\theta = 36.5°$ due to the (111) reflection of the Cu_2O lattice. This indicates that, even though the Cu loading adopted for the two surface modification procedures is the same (0.5%w/w), the surface distribution of the copper is different in the two kind of materials. In the case of materials prepared via wet impregnation (Cu^{2+}-T and Cu^{2+}-ZT) copper is homogeneously dispersed on the oxides surface, whereas in the case of the Cu_2O-T and Cu_2O-ZT samples it can be assumed the formation of a heterojunction.

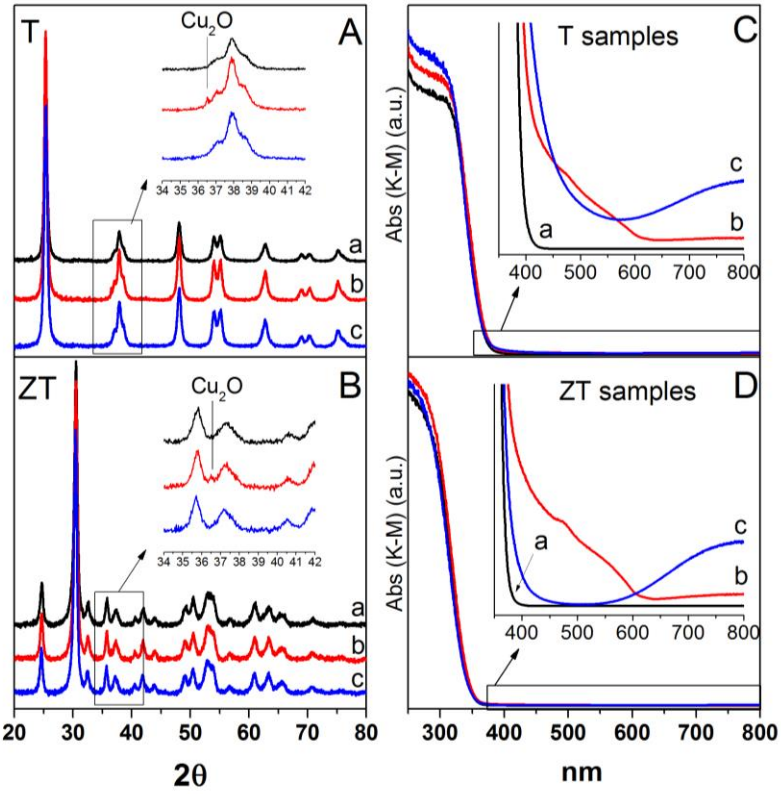

Figure 61. XRD diffractrogams (A and B) and diffuse reflectance UV-Visible spectra (C and D) of the bare oxides and the corresponding Cu modified materials. Panel A and C: a) T, b) Cu_2O-T and c) Cu^{2+}-T. Panel B and D: a) ZT, b) Cu_2O-ZT and c) Cu^{2+}-ZT. The highlighted features which correspond to the (111) reflection of the Cu_2O are also reported in the insets of panel A and B.

The UV-Visible reflectance spectra of all modified samples (Figure 61 C and D) show, beside the band gap transition in the UV region, typical of the two oxides, further absorptions in the visible region. The two surface impregnated samples (Cu^{2+}-T and Cu^{2+}-ZT, spectra C(c) and D(c) respectively) show two new absorptions. The former is in the range of wavelength between 600-800 nm and is related to the d-d transition of Cu(II).[19,22] The second show up in the range between 400-500 nm and can be seen like an absorption partially overlapping the main VB→CB transition. It can be ascribed to the charge transfer from the valence band (VB) of the oxides to the surface Cu(II) species.[159]

The two sample decorated with Cu_2O particles (Cu_2O-T C(b) and Cu_2O-ZT D(b)) show a stronger absorption in the range 400-600 nm typical of Cu_2O particles.[21,130,196] Also in this case in the 600-800 nm region the absorbance is slightly higher than that of the bare materials. This second feature seems suggest that, beside the Cu_2O particles, also a small fraction of Cu(II) is present in these two samples.

Cu^{2+} ions ($3d^9$) bear one unpaired electron and for this reason can be directly monitored by means of the EPR technique.

The EPR spectra of the whole set of copper modified samples recorded at low temperature (77 K) under vacuum are shown in Figure 62.

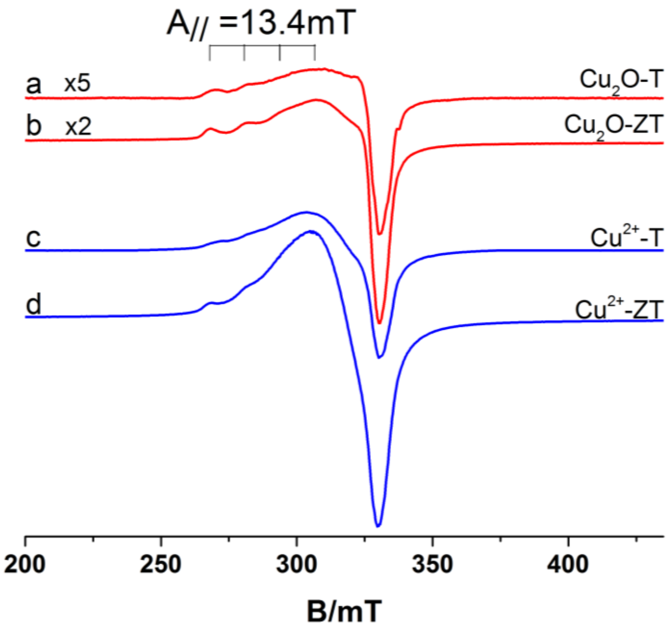

Figure 62. EPR spectra of the Cu modified samples recorded at 77 K under vacuum. a) Cu_2O-T, b) Cu_2O-ZT, c) Cu^{2+}-T and d) Cu^{2+}-ZT.

All samples show EPR signals that appear as the typical fingerprint of Cu^{2+} species. These are more intense in the case of the materials prepared via wet impregnation (Figure 62c and d). A typical Cu^{2+} signal exhibits an axial **g** tensor splitted in 4 hyperfine lines since the Cu nucleus has nuclear spin I=3/2 and the line multiplicity is $n = 2I + 1 = 4$. In all samples the EPR spectrum is characterized by similar spectroscopic features based on the overlap of a broad and asymmetric signal, which dominates the spectrum, with a second Cu(II) species having the hyperfine structure partially resolved in the parallel component ($g_{//}$ = 2.35 and $A_{//}$ = 13.4 mT and non-resolved in the perpendicular one). The first species (broad, unresolved signal) indicates the presence of a family of Cu^{2+} ions mutually interacting with each other via dipolar interaction. These species are probably associated to disordered structures as expected for materials prepared via wet impregnation in mild condition as in the present case.[159] The second kind of paramagnetic species is usually ascribed to isolated Cu(II) ions. Values of the parallel hyperfine coupling constants similar to that found in this case (from 10 to 16 mT), were found also in the case of surface Cu^{2+} species on TiO_2 in an amorphous phase, while, in the case of Cu^{2+} incorporated in the TiO_2 matrix, the A values reported are smaller (8-9 mT).[197-198] The Cu^{2+} ions present in all samples, thus, are traceable to Cu^{2+} species (isolated or mutually interacting) dispersed on the T and ZT surface.

Peculiar is the fact that in Cu_2O modified samples (Figure 62a and b), in principle expected to contain Cu(I) ions only, the presence of Cu(II) ions is also observed. Since the EPR spectrum of bare, unsupported, Cu_2O particles doesn't show any Cu^{2+} signal (data not shown for sake of brevity), it can be inferred that the EPR signals of Cu_2O-T and Cu_2O-ZT samples are not due to Cu^{2+} defects in the Cu_2O nanoparticles, but, rather to a fraction of the starting Cu(I) ions that is unavoidably oxidized during the preparation procedure.

Combining XRD, DR-UV-Visible (Figure 61) and EPR results it can been assumed that the samples prepared by wet impregnation (Cu^{2+}-T, Cu^{2+}-ZT) contain a inhomogeneous dispersion of Cu(II) species on the surface of the oxides supports. At variance, the Cu_2O modified samples exhibit, in addition to a small amount of Cu(II) dispersed on the surface of the supported oxides, small particles of Cu_2O anchored on the main oxide (T or ZT) and , thus, origin a solid-solid interface (heterojunction).

The electronic structure of the modified materials can be modelled according to the schemes reported in Figure 63. Both the modification procedures induce the formation of surface isolated Cu^{2+} species (whose reductive potentials are positioned at +0.16 eV respect to the H_2 potential)[159] more abundant in the case of the solids prepared via wet impregnation. The materials decorated with Cu_2O nanoparticles are also characterized by a Cu_2O/oxide heterojunction.

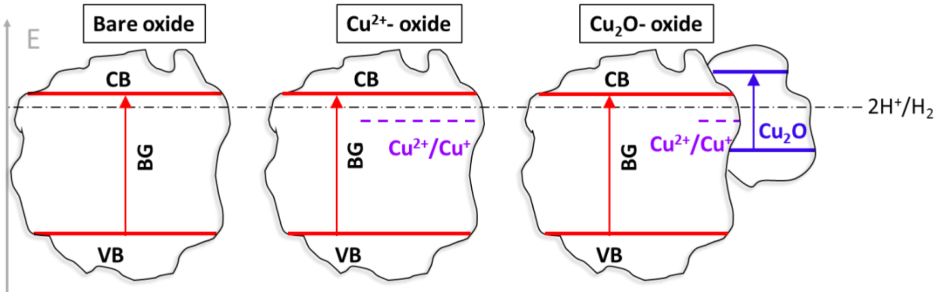

Figure 63. Band structure alignment of bare and Cu modified samples. The case here reported is that of TiO_2 (T). in the case of zirconium titanate (ZT) the situation is analogous.

2.2. Photocatalytic H_2 evolution.

Figure 64 reports the hydrogen evolution rates (mmol g^{-1} h^{-1}) for the whole set of Pt and Cu modified samples compared with the corresponding bare materials. These preliminary tests were performed in the Faculty of Chemistry of Gdansk University and have been adopted as a way to compare the activity of TiO_2 and $ZrTiO_4$ systems and the effect of modifications of the oxides with co-catalysts on H_2 production. Since the experimental setup was not preliminary optimized, the absolute values of H_2 production are here less important.

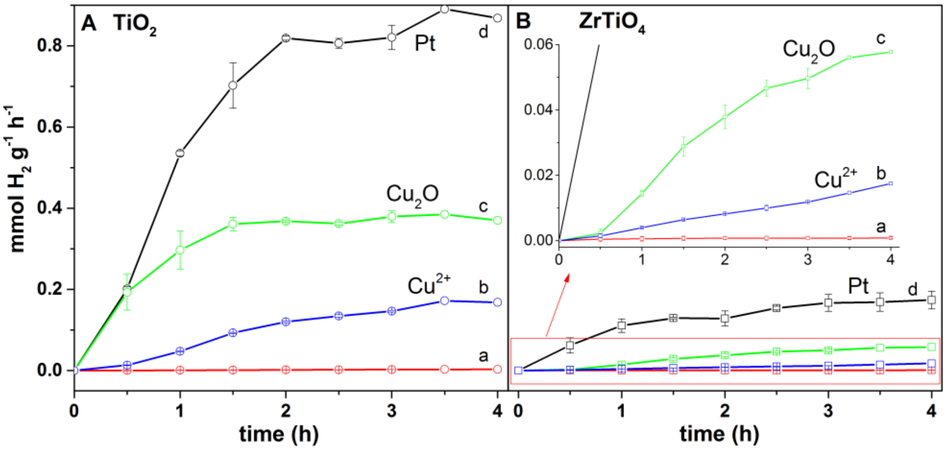

Figure 64. Hydrogen evolution rate (mmol g^{-1} h^{-1}) of different samples. Panel A: TiO_2 based samples. Panel B: $ZrTiO_4$ based samples. a) bare oxides, b) Cu^{2+}-oxides, c) Cu_2O-oxides and d) Pt-oxides.

Analyzing the results in Figure 64 some considerations can be proposed:

- For both the bare oxidic matrices (T and ZT) the H_2 evolution is basically negligible (Figure 64 panel A and B, line a)). In all the other cases the modified TiO_2 samples show a better photocatalytic activity in H_2 evolution with respect to the corresponding $ZrTiO_4$ ones.

  This result could be considered as unexpected considering the slightly more negative potential of the conduction band of $ZrTiO_4$ in comparison to that of TiO_2. That could make this material more inclined to the photoevolution of hydrogen.

- For both TiO_2 and $ZrTiO_4$ systems, the maximum activities are found for the samples modified with Pt (almost 0.9 and 0.2 mmol g^{-1} h^{-1} for Pt-T and Pt-ZT respectively) (Figure 64d panel A and B). Platinum is the best co-catalyst for hydrogen production since it is able, according to some authors,[150-151,199-200] to trap the photogenerated electron, reducing the overpotential for H_2 generation. This modification with platinum was used as reference for other modified systems.
- As far as the modifications with copper are concerned, the presence of copper induces an increase in the photoactivity of the bare oxide. In particular Cu_2O contained materials allows the best performances. As for the Cu modified TiO_2 samples (Cu_2O-T and Cu^{2+}-T) both materials show H_2 evolution after 30 minutes of irradiation. Cu_2O-T however shows the higher evolution already in the starting minutes of irradiation whereas the Cu^{2+}-T sample shows an increase in H_2 evolution rate after 30 minutes. Moreover, after 1.5 hours, the H_2 evolution rate for the Cu_2O-T sample reaches a constant value while the H_2 evolution rate for the Cu^{2+}-T sample still increases in continuous way along the whole experiment. Differently, in the case of the two Cu modified $ZrTiO_4$ samples (Cu_2O-ZT and Cu^{2+}-ZT), both start to generate H_2 only after 30 minutes of irradiation without reaching a plateau.

2.2.1. Conclusions.

The hydrogen evolution tests show that, despite a moderate activity in HER of $ZrTiO_4$ systems, they remain less active than TiO_2 based systems. This observation opens a discussion on some concepts concerning photoactivity and photocatalysis. The only value of band gap energy and flat band potential are not exhaustive in determining the activity properties. The electrochemical potential value is only one of the parameters that is expected to influence the hydrogen evolution. Several other parameters including, for example the e^-- h^+ recombination ability, the density of states in the conduction band, the nature of the surface sites, etc. should be considered for an extended systematic analysis.

Concerning the effect of the different modifications of the oxides, platinum nanoparticles remain the best HER co-catalyst. Nevertheless, the presence of copper on the surface of the oxides influences in positive way the H_2 evolution rate. This occurs especially by anchoring at the surface small particles of Cu_2O which become a good alternative to the expensive Pt co-catalyst.

In other to better understand the mechanism behind the increased photoactivity of the copper modified samples some EPR and DRS experiments under irradiation have been performed. Indeed, as previously described, the Cu^{2+} species are diamagnetic and for this reason can be directly monitored by EPR. The reduced form of copper (Cu^+ and Cu^0), on the contrary, are diamagnetic but can be identified by DRS. Combining EPR and DRS, thus, it can become possible to study the role of the Cu oxidation state changes and the charge separation occurring during the H_2 evolution process. These results will be reported in the next Section.

2.3. Study of Cu oxidation state changes and charge carriers separation during HER.

2.3.1. EPR characterization under irradiation.

Previous studies have shown that Cu(II) centres in TiO_2 can act as electron traps and the same behaviour occurs in the samples investigated in the present work.[19,194,201] Upon UV irradiation in vacuum at 77 K (red spectra in Figure 65) for the whole set of samples the EPR intensity of the Cu(II) species decreases due to the reduction of the paramagnetic Cu^{2+} centres to diamagnetic forms of copper (Cu^{+}/Cu^{0}).

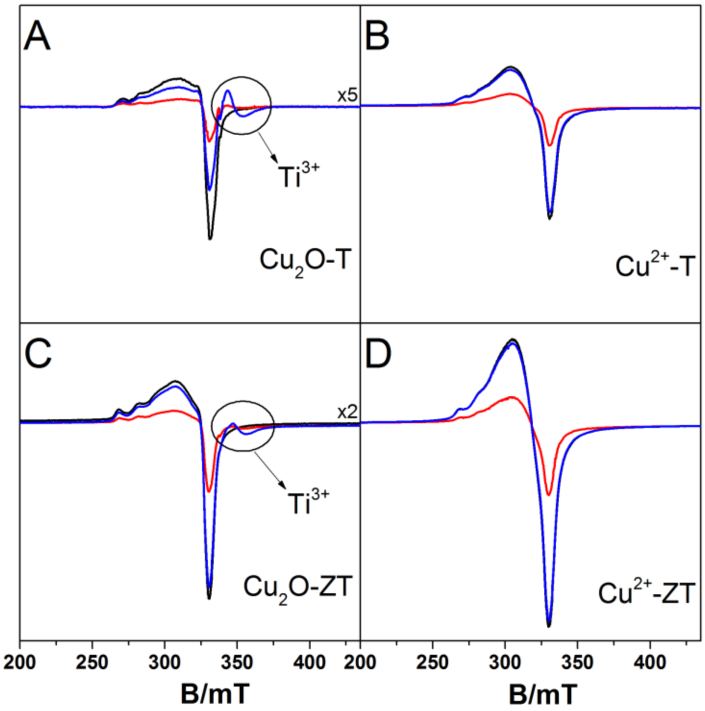

Figure 65. EPR spectra of the as prepared Cu modified samples in dark (black spectra), upon UV-Vis irradiation in vacuum at 77 K (red spectra) and after turning off the light (blue spectra). Panel A and C: Cu_2O modified samples. Panel B and D: Cu^{2+} modified samples. All the spectra were recorded at 77 K with a microwave power of 10 mW.

It is worthy to note that, turning off the irradiation source (blue spectra in Figure 65), the behaviour of the two samples modified with cuprous oxide (Cu_2O-T and Cu_2O-ZT, Figure 65A and C respectively) differs from that of the samples prepared via wet impregnation (Cu^{2+}-T and Cu^{2+}-ZT, Figure 65B and D respectively). In this second case after turning off the light, the Cu(II) EPR intensity is fully recovered and no new signals are photoformed. In the case of Cu_2O-T and Cu_2O-ZT samples, at variance, the starting intensity of the Cu(II) signal is not fully recovered and a new weak signal (g_{average}= 1.93), more intense in the Cu_2O-T sample, appears. This signal is unambiguously ascribed to Ti^{3+} centres. Such difference indicates that the effect on charge carriers separation is remarkably different in the two cases and, in the case of Cu_2O modified samples, a longer lifetime of the separated charge carriers is observed.

In order to better understand the fate of the charge carriers and the role of the Cu species during H_2 evolution, EPR measurements were performed, at regular intervals, during irradiation of samples suspension in a 10% v/v methanol/water solution (same condition of the H_2 evolution test). The irradiation experiment, having a duration of one hour, was stopped at intervals of 5 minutes and an EPR spectrum was recorded after each stop. The EPR spectra of the Cu-containing samples during H_2 evolution are reported in Figure 66. Only three spectra (t = 0, 5 and 30 minutes) are shown for clarity. In the successive figure (Figure 67) the integrated intensities of the EPR signals, of Cu(II) and Ti^{3+} species, monitored in the whole experiment (60 minutes) are reported.

Differently from the case of the irradiation under vacuum, all samples show the formation of Ti^{3+} centres because the methanol, acting as hole scavenger, enhances the life time of the photoformed electrons.

Inspection of Figure 66 and Figure 67 also indicates that, in the case of TiO_2 based samples, after 5 minutes the Cu(II) species completely disappear (Cu_2O-T), whereas, for Cu^{2+}-T, it reaches a minimum in intensity.

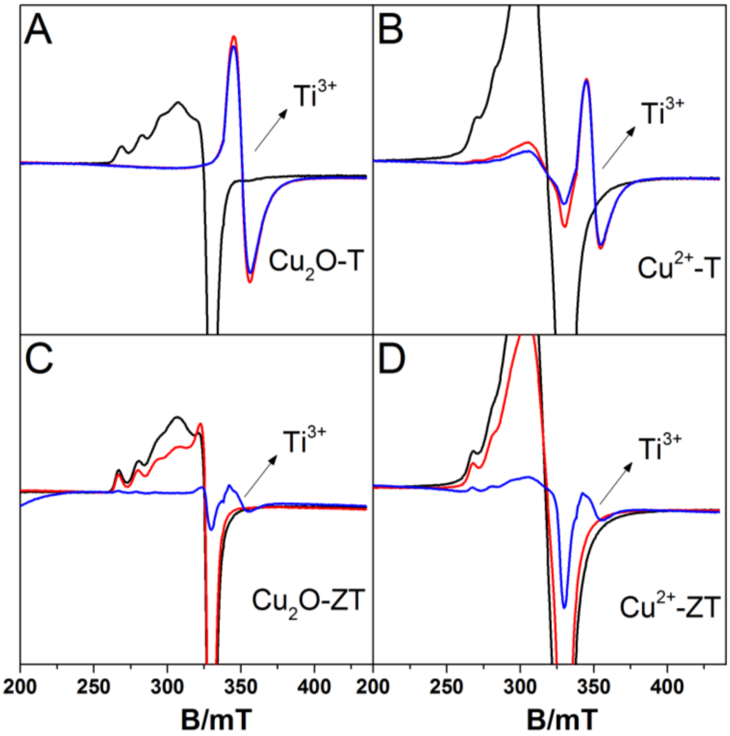

Figure 66. EPR spectra of the as prepared Cu modified samples in methanol/water solution suspension prior irradiation (black spectra), after 5 minutes (red spectra) and after 30 minutes of UV-Visible irradiation at RT (blue spectra). Panel A and C: Cu_2O modified samples. Panel B and D: Cu^{2+}-oxides samples. All the spectra were recorded at 77 K with a microwave power of 10 mW.

In the case of $ZrTiO_4$ based samples the intensity trend of the two paramagnetic species (Cu(II) and Ti^{3+}) is similar to that of the previous case, but shifted of about 5 and 15 minutes later for Cu_2O-ZT and Cu^{2+}-ZT respectively.

As far as Ti^{3+} centers formation is concerned, the kinetic is different comparing the two types of materials (T, ZT). For both Cu_2O-T and Cu^{2+}-T, Ti^{3+} grows after 5 minutes of irradiation in parallel to the Cu(II) decreasing. In the case of the ZT based samples, Ti^{3+} centers show up later when the Cu(II) species tend to its a minimum intensity. In the case of the Cu_2O-ZT Ti^{3+} begins to grow up after 10 minutes of irradiation and for the Cu^{2+}-ZT after 20 minutes of irradiation.

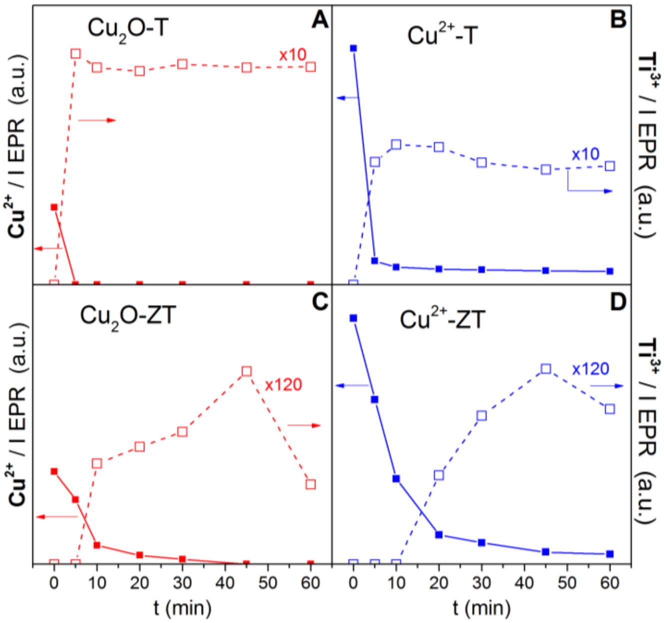

Figure 67. EPR intensities of Cu^{2+} (straight lines) and Ti^{3+} species (dashed lines) at different times of UV-Visible irradiation of Cu_2O-oxides (panels A and C, red lines) and Cu^{2+}-oxides (panels B and D, blue lines) in methanol/water suspension.

Summarizing, during the irradiation in liquid phase, the presence of an hole scavenger (CH_3OH) emphasizes the role of photogenerated electrons. The working photocatalysts is rich of trapped electrons that, firstly, reduce Cu^{2+} ions and only later Ti^{4+} cations to Ti^{3+}. Ti^{3+} centers, in fact, show up only when the Cu(II) are exhausted or reaches a minimum in intensity.

2.3.2. UV-Visible DRS characterization under irradiation.

Figure 68 reports the same experiment shown in Figure 66 which is, in this case, followed by optical spectroscopy. The effect of irradiation on the oxidic materials (bare and Cu-modified), in presence of a methanol/water solution (10% v/v), is shown after 30 and 60 minutes (curves b and c in Figure 68). The presence of the solution causes the onset of two absorption bands, ascribable to the infra-red active groups of the water/methanol solution, centered at about 1000 nm and 1200 nm which will not be further discussed in the following.

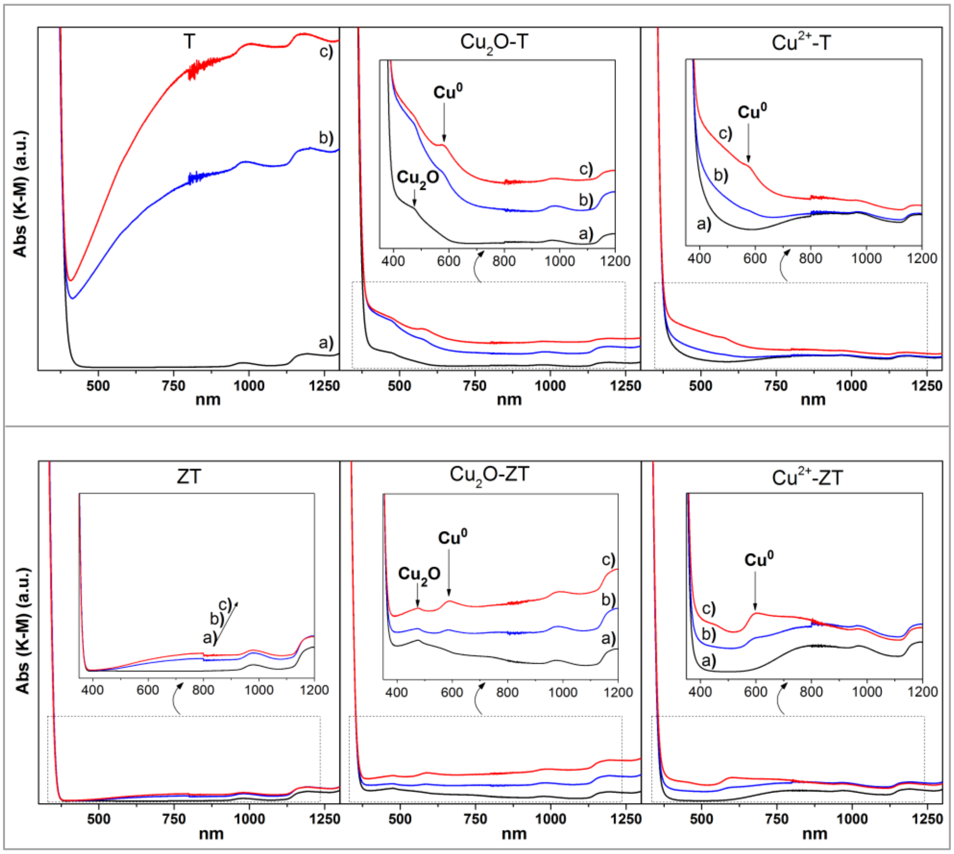

Figure 68. DR-UV-Visible spectra of the different systems in presence of methanol/water solution (10% v/v). a) as prepared samples, b) after 30 minutes of UV-Visible irradiation and c) after 60 minutes of UV-Visible irradiation.

As far as the bare materials (T and ZT in Figure 68) are concerned a continuous absorption in the visible and NIR regions grows along the irradiation process which is due to Ti^{3+} ions formation.[202] Zirconium titanate appears, as it is already known, less reducible than titanium dioxide.

Concerning Cu modified samples the spectra obtained during irradiation are complex due to the presence of copper species in various oxidation states (see Section 2.1.2.). More in detail, in the case of the Cu_2O containing samples (Cu_2O-T and Cu_2O-ZT in Figure 68) the starting spectroscopic features of the Cu_2O particles, in the region between 400 nm and 600 nm, are preserved after irradiation as indicated by the specific absorption at 475 nm. Simultaneously, after 30 minutes of irradiation, a further absorption peak at about 580 nm clearly appears. Such feature correspond to the Surface Plasmonic Resonances (SPR) of metallic copper particles[203-204] and unambiguously indicates that the reduction of the Cu species proceeds until the zero oxidation state. Since the EPR spectra (Figure 66A and C) indicate that the Cu^{2+} species undergo a reduction during irradiation, the formation of metallic copper occurs at the expense of Cu^{2+} species dispersed on the surface of the samples. This implies the migration and the aggregation of isolated Cu species. The process is favored by the reduction to a neutral (Cu(0)) species not affected by the surface electric fields.

In the case of Cu^{2+}-T and Cu^{2+}-ZT samples, after each irradiation step, a new absorption feature arise in the region between 400 nm and 600 nm similar to that reported for the Cu_2O decorated materials. This feature suggests that the reduction of Cu(II) to Cu(I) occurs.[205] This does not necessarily mean that true Cu_2O particles are formed. Most likely the isolated Cu^{2+} species are reduced to similar Cu^{+} ones. Furthermore, it is worth to note that after 60 minutes of irradiation, also in this case, the formation of metallic copper occurs.

A further confirmation of the reduction of Cu(II) to Cu(I) and Cu^0 during the photocatalytic reaction is provided by an "ad-hoc" performed experiment of thermal annealing of the Cu^{2+}-T sample at different temperature under vacuum. In such condition (as previously described) the material undergoes a progressive reduction. The results of consecutive vacuum annealing on EPR and DRS spectra of Cu^{2+}-T sample are reported in Figure 69. Annealing at 373 K (Figure 69 b, red spectra) causes a slight decrease of the Cu(II) EPR signal and, simultaneously, an absorption typical of Cu(I) species[205] grows in the DRS spectra. This behaviour is more accentuated after annealing at 473 K (Figure 69 c, blue spectra). After annealing at 773 K (Figure 69 d, green spectra) the Cu(II) EPR signal completely vanishes and the reduction process of Cu(II) continues until the formation of metallic copper as indicated by the peak at 580 nm in the DRS spectrum. At this temperature, beside the formation of reduced forms of copper, the formation of Ti^{3+} ions also occurs (Figure 69, Panel B).

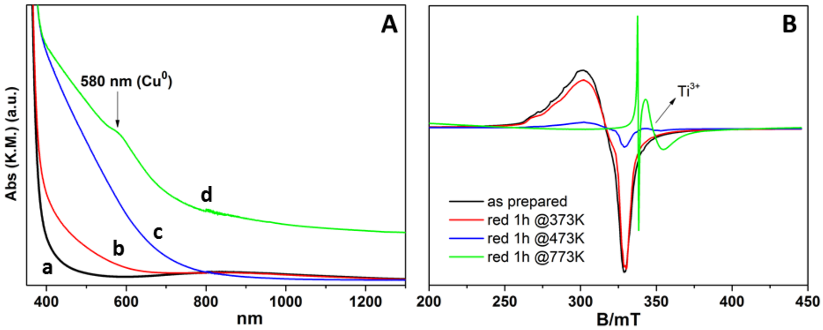

Figure 69. UV-Visible DRS (Panel A) and EPR spectra recorded at 77K (Panel B) of Cu^{2+}-T sample outgassed at room temperature (a, black spectra)and after annealing for 1h under vacuum at 373 K(b, red spectra), 473 K (c, blue spectra) and 773 K (d, green spectra).

To conclude, the combination of the EPR and UV-Visible DRS measurements clearly demonstrates that the irradiation induces a radical transformation of the as prepared materials in more complex systems. In particular, when the Cu containing photocatalysts produce hydrogen and reach a composition nearly constant as a function of time, they are in a reduced state with respect to the starting systems. Metallic Cu aggregates are formed (with reduction and migration of isolated Cu^{2+}) in the case of Cu^{2+}-T and Cu^{2+}-ZT and, likely, in the same way in the case of Cu_2O-doped samples. In the latter case a second phenomenon of Cu_2O particles reduction to Cu(0) cannot be excluded but at least a fraction of the original Cu_2O particles remains unaffected. The working system also contains reduced Ti^{3+} ions which are more abundant in T samples, more reducible than ZT ones.

2.3.3. Charge carriers dynamics during H_2 evolution reaction.

On the basis of the EPR and optical results obtained in Sections 2.3.1 and 2.3.2, the chemical modifications occurring during irradiation at the surface of the catalysts and the hydrogen evolution mechanism can be proposed according to the scheme reported in Figure 70 and Figure 71 respectively.

Since the experimental results suggest that the behavior of the ZT based samples is basically the same observed for the T based samples, although overall less effective, in the following the two sets of material (T and ZT based samples) will be discussed together.

All the investigated Cu-modified samples show, upon irradiation with UV light, an higher hydrogen evolution than the corresponding bare materials and the mechanism operating on the two kinds of modified materials is very likely different in the two cases considering the different chemical nature of the copper in the starting samples (mainly Cu(II) in Cu^{2+}-T/ZT and mainly Cu(I) in Cu_2O-T/ZT).

Concerning the Cu^{2+} containing samples the EPR characterization shows that Cu^{2+} is easily consumed upon irradiation under vacuum (Figure 65) and, even more efficiently, in the operative conditions of the photocatalytic reactions (Figure 66). It is worth to note, furthermore, that the Ti^{3+} ions can be photogenerated only when the Cu(II) amount is reduced to a minimum value (Figure 67). When the reaction reaches a steady state, Cu(II) is nearly absent in the systems. For this reason, the enhanced activity of the Cu^{2+}-T/ZT samples, with respect to the bare materials, has to be ascribed to other copper species forming during the irradiation. The optical spectroscopy experiments indicate, indeed, that reduction of copper to Cu(0) occurs. Therefore, it is possible to suggest that the isolated Cu^{2+} species are progressively photoreduced to form, after migration on the surface, small Cu(0) aggregates (see Figure 70).

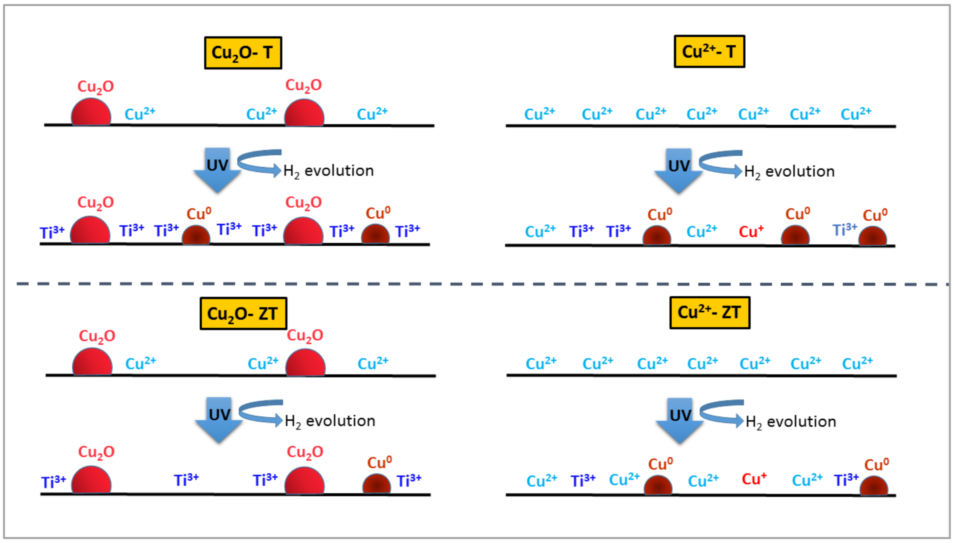

Figure 70. Chemical modifications occurring at the surface of the different Cu modified samples during H_2 evolution reaction.

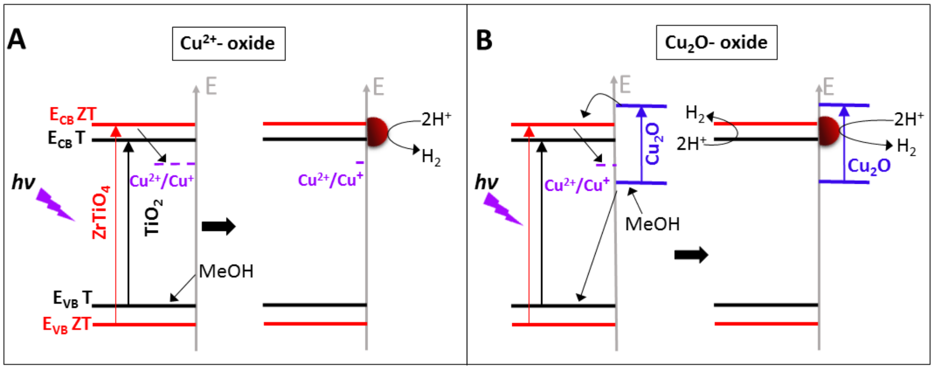

Figure 71. Model of H_2 evolution mechanism occurring on Cu^{2+}-oxides (panel A) and Cu_2O (panel B) oxides respectively. The band position are reported on the basis of the energy values reported in refs 195,206.

This occurs in particular in the case of Cu^{2+}-materials but also in those containing Cu_2O particles that also contain a non-negligible concentration of Cu^{2+}. In the latter case, though a formation of a further amount of Cu(0) particles at the expenses of Cu_2O ones cannot be excluded, a fraction of Cu_2O aggregates remains unaffected at the surface, as indicated by the specific absorption at 475 nm (Figure 68). The Cu^{2+}- and Cu_2O-materials differs therefore, in operative conditions, in terms of the presence of a Cu_2O-oxide interface that is not present in the case of Cu^{2+}-T and Cu^{2+}-ZT systems. This specific composition and the role of Cu_2O are, likely, the reason of the superior activity of these kind of materials with respect to those prepared by wet impregnation and Cu^{2+} surface dispersion.

The mechanism of H_2 evolution in the described photocatalysts can be tentatively discussed on the basis of the previously illustrated composition of the working systems and also considering the electronic energies of the species involved (Figure 71). During H_2 evolution the solids contain negligible amount of Cu^{2+}. This is because cupric ions act as electron traps being at lower energy than the oxide conduction band. Ti^{3+} ions, in fact, are photogenerated only when the Cu(II) amount is reduced to a minimum value. Thus, the formation of metallic copper by reduction of Cu^{2+} under irradiation is the key step to explain the increased catalytic activity of Cu^{2+}-T and Cu^{2+}-ZT materials with respect to the bare oxides (Figure 71A). The role of metallic copper as a co-catalyst for H_2 evolution remain an open question. Cu(0) particles, in fact, are not among the most prominent hydrogenation co-catalysts such as Pt and Pd ones even if they take part to important process such as methanol synthesis from CO and H_2.[207-208] The fact remains, however, that several Authors report that metallic Cu can act as a co-catalyst for hydrogen production.[166-169]

In the case of Cu_2O containing materials, which are more active than those based on Cu^{2+}, a plausible mechanism is as follows. The irradiation causes a charge separation in both the Cu_2O particles and the oxidic supports. Because of the relative position of the band potentials, the electrons transfer from the Cu_2O conduction band to the oxides conduction band occurs (Figure 71B). Simultaneously the photoformed holes in the valence band of T or ZT move to the Cu_2O valence band inhibiting the charge carrier recombination. This mechanism explains the fact that the Ti^{3+} ions formation upon irradiation in vacuum (Figure 65) is observed in this kind of materials and not in the samples prepared via wet impregnation (Cu^{2+}). Summarizing, the synergic effect of the presence of the Cu_2O/oxide heterojunction and metallic copper leads to a H_2 evolution rate definitely higher than that obtained on Cu^{2+}-T and Cu^{2+}-ZT samples that contains copper metal particles only.

2.3.4. Conclusions.

In this Section the photochemistry of the copper containing photocatalysts has been investigated leading to a detailed picture of the composition of the various systems in working conditions. In parallel a possible mechanism of H_2 evolution has been proposed.

The results obtained via the joint use of EPR and UV-Visible DRS spectroscopies clearly indicate that, during the irradiation, all the as prepared solids undergo a chemical transformation and metallic copper is generated. Consequently, the real photocatalyst involved in the H_2 evolution reaction is different from the starting material in particular for the photocatalysts prepared via wet impregnation. Furthermore, in the materials decorated with Cu_2O particles, the charge carriers separation is more efficient because of the presence of an heterojunction which is preserved during the reaction. The better performance in H_2 evolution for this kind of material, should be due to the synergic effect of these two forms of copper (Cu^0 and Cu_2O). A second difference is between T-type and ZT-type materials. In the former case the different reducibility of the TiO_2 matrix favors the presence of higher amounts of photoformed Ti^{3+} in operative conditions. Also this parameter seems to be critical for the photocatalytic activity as the T samples are systematically more active than ZT ones.

3. Hydrogenase-TiO_2 hybrid systems.

The purpose of this chapter is to report about the investigation of hybrid systems formed by the combination of hydrogenase and modified titanias. In this case, the protein has the role of co-catalyst for hydrogen evolution while TiO_2 acts as "producer" of photoelectrons available for the protein. The use of modified titanias arises from the need to extend the photoactivity of the pristine TiO_2 (limited to the UV part of the solar light) to the visible range. These materials, indeed, are doped anatase polymorphs capable of harvesting some visible components of the solar spectrum.

In particular, comparing the results with those of a sample of bare anatase, two kind of modified TiO_2 have been employed: i) N-doped anatase, a yellow material, and ii) a substoichiometric reduced anatase which shows a deep blue color.

In N-doped TiO_2 (N-TiO_2) the presence of nitrogen defects in the lattice of the oxide generates intra band gap energy that origin the yellow color of the powder.[10,12-13,209]

The substoichiometric TiO_2 (rd-TiO_2) is prepared via a particular synthetic route that lead to a partially reduced, blue oxide (TiO_{2-x}) which is stable in air and shows the presence of stable Ti^{3+} ions. The color in this case is due to the tail of a broad absorption centered in the infrared region and typical of reduced titanias.[210-216]

My attention was paid not only to the efficiency of the hydrogenase-TiO_2 materials in hydrogen production but also to the mechanism of interaction of the protein with the solid and to the effect of irradiation on the hybrid materials. All this has been monitored by EPR spectroscopy.

The EPR experiments of the present work have been performed in aqueous solutions containing thionine and triethanolamine (TEOA).

TEOA molecule acts as a buffer and as sacrificial electron donor (or scavenger of the photogenerated holes) for TiO_2.[133] Thionine plays the role of stabilizing the oxidized form of the H-cluster (named H_{ox} state) characterized by a diamagnetic $[4Fe4S]^{2+}$ sub-cluster.[145]

The results of this activity will be organized as follows: firstly the characterization of the oxide supports will be reported. Afterwards the effect of the irradiation on the thionine-TEOA aqueous solution and on the suspension of the various bare supports in the same solution will be described on the basis of the EPR spectra recorded in the absence of the enzyme. Then the same approach will be followed for the suspension containing the hydrogenase/oxide nanohybrids. Finally, the hydrogen production ability under solar irradiation of the three hybrid systems in TEOA solution will be compared.

3.1. Oxide characterization.

XRD analysis was performed on the three distinct support oxides namely: bare TiO_2, N-TiO_2 and rd-TiO_2.

The corresponding XRD patterns are reported in Figure 72A. All the diffraction pattern are characterized by peaks at the same position that correspond to those of the anatase polymorph. However, while TiO_2 and N-TiO_2 exhibit the same linewidth, the pattern of rd-TiO_2 shows much narrower peaks since this oxide possesses significantly larger crystallites. This result is also confirmed by the surface area measurements (BET method), indicating about 80 m^2/g for TiO_2 and N-TiO_2 and about 10 m^2/g for rd-TiO_2.

Figure 72 B compares the diffuse reflectance UV-Visible spectra of TiO_2 (black line), N-TiO_2 (red line) and rd-TiO_2 (blue line) powders.

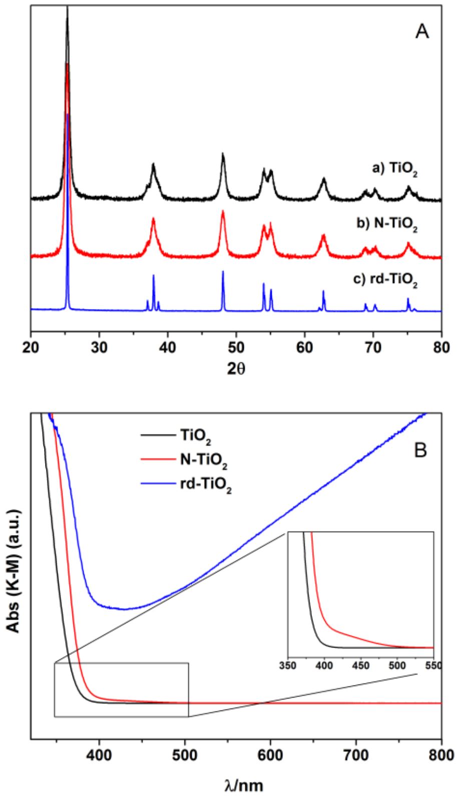

Figure 72. Panel A: X-ray diffraction patterns of a) TiO_2, b) N-TiO_2 and c) rd-TiO_2 powders. Panel B: UV-Visible diffuse reflectance spectra of TiO_2 (black line), N-TiO_2 (red line) and rd-TiO_2 (blue line) powders. In the inset a magnification of the visible absorption of N-TiO_2 and TiO_2 is reported.

The spectra of TiO_2 and N-TiO_2 differ for an absorption shoulder in the visible region centered at about 450 nm and due to intra band gap energy states which are present in the case of N-TiO_2 (magnification in the inset of Figure 72B).[10,12-13]

At variance, the rd-TiO_2 presents a strong continuous absorption in all visible region that is extended also in the NIR and which is typical of substoichiometric materials containing excess electrons localized on Ti^{3+} centers or delocalized in the conduction band.[210] The band gap values, calculated with the Tauc method, are 3.2 eV for TiO_2 and N-TiO_2 and 2.88 eV for rd-TiO_2. These values indicate that the visible absorption and the consequent yellow color of N-TiO_2 sample are due to the absorption shoulder centered at 450 nm and not to a band gap transitions which correspond to UV wavelengths. As opposite the band gap transition of rd-TiO_2 oxide occurs in the visible region.

3.2. Effects of irradiation followed by EPR spectroscopy.

H_2 production upon irradiation of the various hydrogenase-TiO_2 hybrid systems is based on the light-induced charge separation (electrons and holes). While the holes are scavenged by TEOA, the electrons are transferred, via the series of Fe-S-clusters,[139-140] to the active site of the enzyme where the reduction of water protons into molecular hydrogen occurs.

The EPR experiments under irradiation of the hybrid systems are useful to understand the electron transfer between the protein and the support oxides. All the EPR experiments have been performed in a water solution of TEOA and thionine. The latter is needed to stabilize the H_{ox} state of the protein that is the only diamagnetic state of the H-cluster. Hence with the presence of the thionine in the solution we are able to detect the active site of the enzyme by EPR technique.

In order to investigate the photoinduces process on the hybrid system, a preliminary EPR experiments has been performed on the thionine-TEOA solution in order to understand the possible interference of these molecules with the results of the successive experiments involving irradiation of the hybrid systems. For this experiment a water solution of TEOA (25 mM) and thionine (1.39 mM) was prepared, and gradually frozen at 77 K for EPR measurements.

Figure 73 shows the effect of the UV-Visible irradiation of this thionine solution. The spectrum of the as prepared thionine in TEOA solution in dark (Figure 73a) shows a very weak signal centered at $g = 2.005$. This signal however increases upon irradiation (Figure 73b) and disappears by heating the sample at room temperature in dark (Figure 73c). The isotropic signal at $g = 2.005$ is due to the formation of small amounts of the thionine radical cation,[217-218] and is not observed irradiating a solution containing TEOA only. The radical species is stable keeping the sample at 77 K and is destroyed raising the temperature.

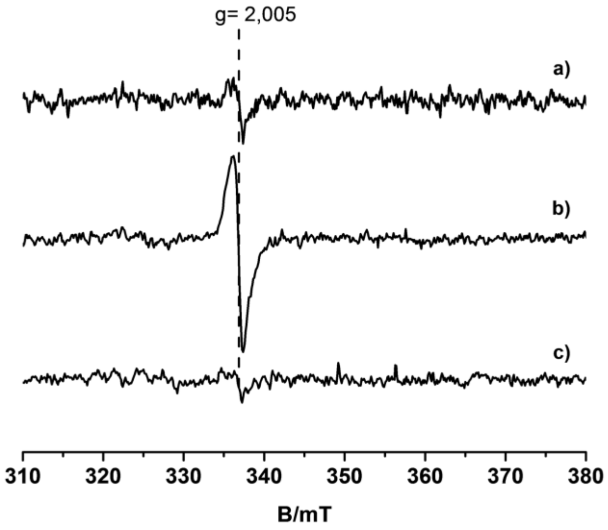

Figure 73. EPR spectra of the thionine - TEOA solution: (a) as prepared solution in dark, (b) under UV-Visible irradiation at 77 K, (c) after thaw-freeze treatment (lamp off, heating at RT and cooling again at 77 K). All spectra are recorded at 77 K and with microwave power of 10 mW.

A second preliminary investigation consists in the EPR study under irradiation of the suspensions of the three solid supports (TiO_2, N-TiO_2, rd-TiO_2) in the absence of the surface anchored protein. This experiment is essential for a comparison with the results of irradiation of the hybrid systems in the same conditions

The samples have been irradiated by UV-Visible light at 77 K. The results are reported in Figure 74 which also reports (spectrum a, for each material) the spectrum of the dry powder prior formation of the suspension.

The TiO_2 powder in air (Figure 74A(a)) is EPR silent, and the spectrum of the as prepared TiO_2 suspension in dark (Figure 74A(b)) shows very weak signals including that at g = 2.005, due to the presence of thionine. The irradiation with UV-Visible light of the suspension (Figure 74A(c)) causes, beside the increase of the thionine radicals signal (marked by an asterisk), the formation of a broader signal centered at *g* = 1.93 and unambiguously due to Ti^{3+} ions in anatase.[30] This experiment indicates that the electrons formed upon irradiation remain in the solid where they are trapped by Ti^{4+} ions which are reduced to Ti^{3+}.[26,31] The formation of the thionine radical ion is a side-effect of the process and will be no longer discussed in the following.

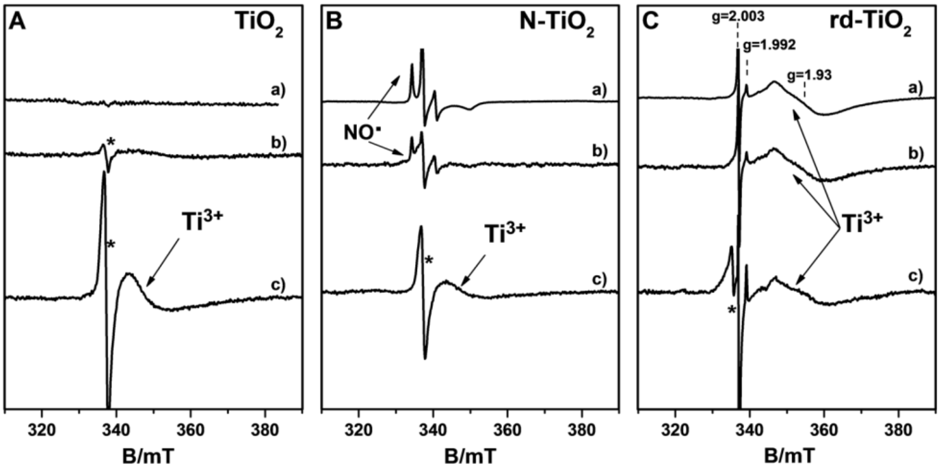

Figure 74. EPR spectra of TiO_2 (A), N-TiO_2 (B) and rd-TiO_2 (C) systems recorded under different conditions. (a) powder material in air, (b) suspension of the powder in TEOA-thionine solution; (c) UV-Visible irradiation of the suspension. The asterisk indicates the signal of the thionine radical cation. All spectra are recorded at 77 K and with microwave power of 10 mW.

The same experiment was performed also for the N-doped and the reduced TiO_2 materials.

In the former case the final result is the same observed for bare TiO_2 that is the formation of Ti^{3+} centers upon irradiation of the suspension (Figure 74B(c)). The spectra before irradiation Figure 74B(a) and Figure 74B(b) are affected by the presence of nitric oxide (NO) which is a byproduct of the N-TiO_2.[13] The NO EPR signal is no more visible after irradiation probably because the NO molecule reacts with the photoformed charge carriers.

In the case of the substoichiometric TiO_2 (rd-TiO2) the spectrum of the powder (Figure 74C(a)) show, beside of an isotropic signal at *g* = 2.003, possibly connected with electron trapped at grain boundaries defects, one narrow signal centered at g = 1.992 ad a broader one centered at g = 1.93 typical of bulk and surface Ti^{3+} ions in anatase respectivelly.[26,30] The suspension of the rd-TiO_2 in TEOA-thionine solution (Figure 74C(b)) maintain the same EPR feature of the powder, while the UV-Visible irradiation (Figure 74C(c)) causes few modification essentially due to the thionine radical cation. Is more difficult, in this case, to appreciate the change in intensity of the broad signal of Ti^{3+} centers because the sample already contains structural Ti^{3+} center prior irradiation.

The same kind of EPR experiments performed on TiO_2 suspensions have been carried, in the same experimental conditions, on the three oxide impregnated with the protein (CpHydA). Figure 75(A), (B) and (C) reports the EPR spectra of TiO_2-CpHydA, N-TiO_2-CpHydA and rd-TiO_2-CpHydA respectively. For the sake of comparison, the first spectrum (a) is always that of the H_{ox} state of CpHydA alone in TEOA-thionine solution.

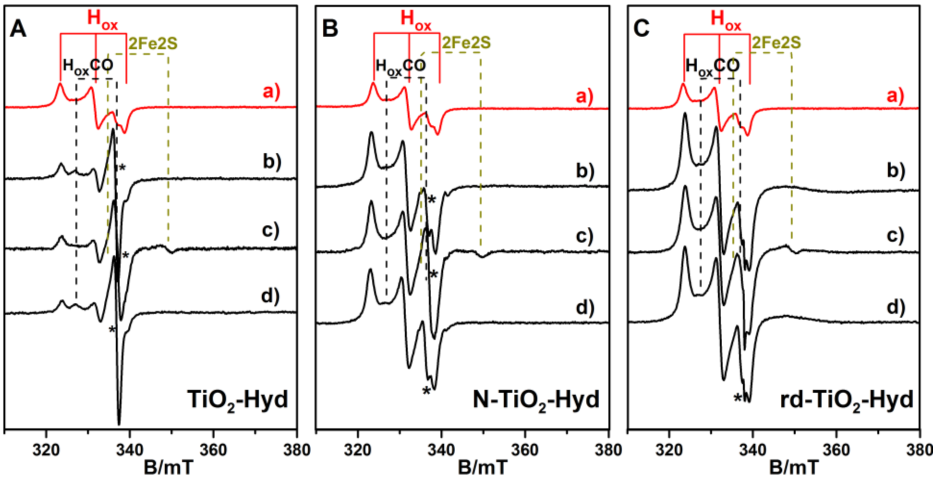

Figure 75. EPR spectra of TiO_2-CpHydA (A), N-TiO_2-CpHydA (B) and rd-TiO_2-CpHydA (C) hybrid systems suspended in TEOA-thionine solution. In all cases the spectrum (a) is that of the CpHydA protein reported for comparison. (b) as prepared oxide-CpHydA hybrid systems in dark; (c) the same system upon irradiation (15 min with UV-Visible light); (d) upon thaw-freeze treatment in dark (lamp off, heating at RT and cooling again at 77 K). The signals marked by an asterisk are due to the presence of the thionine in the solution. All spectra are recorded at 77 K and with microwave power of 10 mW.

The spectra of the first and second hybrid systems and their behavior under irradiation are similar, at least in qualitative terms and will be discussed together.

The EPR spectra of the as prepared oxidized hybrid systems in dark, Figure 75A(b) and Figure 75B(b), are dominated by the signal of H_{ox}, (compare with Figure 75a, red spectrum). In addition a weaker signal of the H_{ox}-CO species is visible. This particular species represents a byproduct, commonly observed in [FeFe]-hydrogenases spectra, due to the decomposition of the protein: the CO ligands, dissociated from damaged H-clusters, probably bind as free CO molecules to intact H-clusters forming the H_{ox}-CO species.[219] The typical g values of CpHydA (H_{ox} state) are g_1 = 2.0892, g_2 = 2.0363 and g_3 = 1.9954 while for H_{ox}-CO the main values are at $g_{//}$ = 2.075 and $g_{\perp}$ = 2.008.[170]

The fact that the spectra observed for the surface-anchored protein strictly correspond to those of the free protein, clearly suggests that the active site is not strongly perturbed by the interaction with the oxide and that it preserves its local geometry and chemical environment (at least the part of the H-cluster that is detectable by EPR) during the impregnation process and the related treatments.

Irradiation of the two hybrid systems (TiO_2, N-TiO_2) with UV-Visible light (Figure 75A(c) and Figure 75B(c)) causes small but significant changes in the EPR spectra. The weak signal due to the H_{ox}-CO species decreases in intensity, in agreement with previous studies,[219-220] while a new small signal, having a component clearly appreciable at g = 1.93, appears. This signal corresponds to that of the reduced $[2Fe2S]^+$ clusters, with is

characterized by g values g_1 = 2.0227 and g_2 = 1.936. This center is peculiar of this type of hydrogenases and it is paramagnetic in reductive conditions.[221-222] This signal is also detectable upon irradiation of the protein alone and thus it is not an evidence of electron transfer from TiO_2 to the protein. The features of this spectrum are stable when the lamp is turned off maintaining the sample at 77 K (data not shown) while, after thaw-freeze (RT-77 K) the signal due to the reduced $[2Fe2S]^+$ disappears and the EPR spectrum becomes the same observed before irradiation.

However the most important feature of the sequence reported in Figure 75A and B is that the broad EPR signal, typical of reduced Ti^{3+} centers in irradiated-TiO_2 and N-TiO_2 suspensions (Figure 74), is not observed upon irradiation of the same samples containing the anchored protein. This is a clear evidence of an electron transfer from TiO_2 to the protein under irradiation. The photoexcited electrons, in this case, are not stabilized by the matrix as Ti^{3+} ions, but are transferred from the oxide to the protein.

In the case of the rd-TiO_2-CpHydA material things are in part different. Also in this case the main features of the spectrum of the as prepared hybrid system (Figure 75C(b)) are those of the H_{ox} state of the protein. In the right side of this spectrum weak signal of Ti^{3+} ions is observed. However this Ti^{3+} signal is clearly less evident than that of rd-TiO_2 in suspension (Figure 74C(b)). This indicates that, upon contact with the protein, the reduced Ti^{3+} centers have been nearly completely scavenged by the protein. In Figure 76 the comparison between the spectrum of the rd-TiO_2 suspension alone and that of the hybrid system rd-TiO_2-CpHydA is reported. It clearly evident that the features of Ti^{3+} in the hybrid system are drastically suppressed. This result is quite amazing if one keeps in mind that the Ti^{3+} centers of rd-TiO_2 are stable in air (i.e. not oxidized by O_2). The electron scavenging ability of the anchored hydrogenase is therefore rather strong.

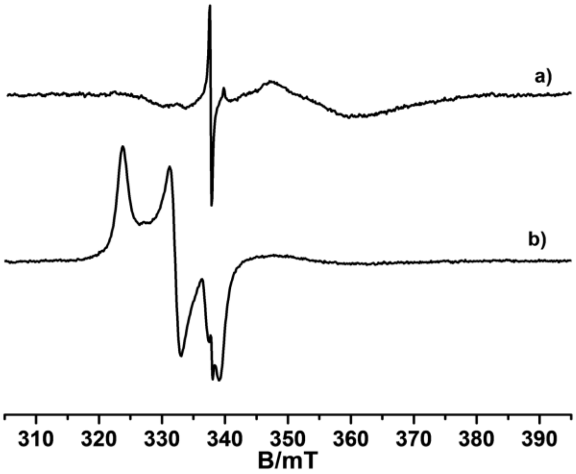

Figure 76. EPR spectra of rd-TiO_2 suspension (a) and rd-TiO_2-CpHydA systems (b). All spectra are recorded in dark at 77 K and with microwave power of 10 mW.

The UV-Visible irradiation of the rd-TiO_2 sample (Figure 75C(c)) has effects similar to those exhibited by the two other samples. In fact the reversible formation of the signal of reduced $[2Fe2S]^+$ clusters (g = 1.936) is observed again.

In all hybrid systems tested upon irradiation a slight decrease of the H_{ox} signal intensity is observed suggesting, for a fraction of the protein, a reduction of the active site to an EPR silent form.

The EPR results can be summarized as follows.

a) Irradiation of a suspension of TiO_2 materials, in the presence of TEOA and thionine, cause the formation of Ti^{3+} centers in the solid since the photogenerated electrons are trapped by Ti^{4+} sites. The holes photogenerated in parallel are annihilated by TEOA. In the case of the rd-TiO_2 sample (which already contains structural Ti^{3+} center even before irradiation) it is more difficult to appreciate the change in intensity of the Ti^{3+} centers.

b) The anchoring of the hydrogenase on oxidic supports doesn't cause any change in the features of active site (H-cluster) of the protein, monitored in terms of EPR spectra of its oxidated form (H_{ox}). Moreover, in the case of rd-TiO_2, the intensity of the Ti^{3+} signal decreases just upon simple contact with hydrogenase suggesting that a large fraction of the excess electrons in the system are scavenged by the protein.

c) Irradiation of titania supported hydrogenase causes a (low) decrease in intensity of the H_{ox} signal and, most important, does not induce the formation of reduced Ti^{3+} centers in the solid, as contrariwise occurs in the case of the bare oxides.

These three facts converge in indicating that the electrons generated by irradiation of the solid are scavenged by the protein and become potentially available for H^+ reduction.

With this in mind the photocatalytic activity of the various hybrids in the production of hydrogen under solar irradiation can now be compared.

3.3. Photocatalytic H_2 evolution.

In order to obtain an evaluation of the photocatalytic activity, the hydrogen evolution of the three TiO_2-based hybrid systems were tested under direct solar light irradiation for 60 minutes in TEOA water solution. The corresponding blank tests were performed in the same condition using the oxide supports only.

Figure 77 reports the H_2 evolution rates of the three TiO_2-CpHydA hybrid systems in comparison with those of the TiO_2 powders alone.

The control experiments performed both in the dark and in the absence of TiO_2 did not show any detectable H_2 production (data not shown).

Figure 6 clearly shows that all the hybrid systems exhibit a significantly higher activity in H_2 evolution with respect to that observed for the TiO_2 powders alone.

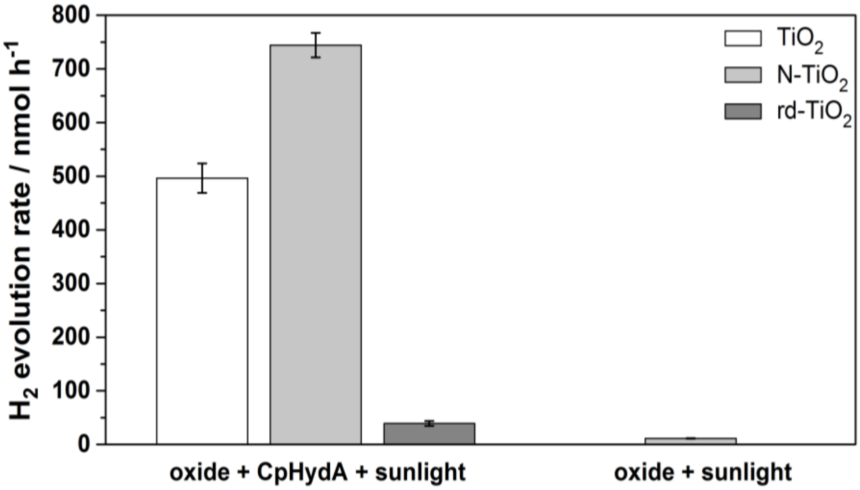

Figure 77. H_2 evolution tests. Different TiO_2 powder systems (1 mg/ml) impregnated with CpHydA (50 nM) or alone in TEOA solutions irradiated with natural sunlight. Left hand side: hybrid systems. Right hand side: only oxide. The error bars refer to triplicate standard deviation.

The amount of H_2 after 1h of solar light exposure for the three different systems (1 mg/ml) are: 496.3 nmol for TiO_2-CpHydA, 744.3 nmol for N-TiO_2-CpHydA and 39.4 nmol for rd-TiO_2-CpHydA while for the TiO_2 system without the protein the amount is not relevant in comparison with the hybrid systems.

The turnover frequency numbers (TOF) for these systems are: 2.8 ± 0.2 s^{-1} (TiO_2-CpHydA); 4.1 ± 0.1 s^{-1} (N-TiO_2-CpHydA) and 0.6 ± 0.1 s^{-1} (rd-TiO_2-CpHydA).

Comparing the activity of the three hybrid systems it is worth to notice that (i) the system based on bare TiO_2 (white) shows an intermediate activity between that of the two colored materials, (ii) the activity of rd-TiO_2 is lower than that of the other materials also taking into account the lower surface area, (iii) N-TiO_2 sample show the better photocatalytic performance. This increased photoactivity with respect to pure TiO_2 is due to the presence of nitrogen intra band gap states in the

TiO_2 band gap that allow to some photons of the visible region contribute to the photoexcitation.

The poor activity of rd-TiO_2, despite its intense blue color, indicates that the simple coloring does not automatically imply a high photoactivity with visible light. The poor activity of the rd-TiO_2 sample could due to the presence of the high defectivity typical of this kind of reduced materials. Defects, in fact, can represent recombination centers detrimental for the photoactivity limiting the number of electron available for the protein.

3.4. Conclusions.

In this part of PhD thesis another type of TiO_2 modification has been investigate with the purpose to make the titania more active in H_2 evolution. Three different TiO_2-hydrogenase hybrid systems have been studied: TiO_2-CpHydA, N-TiO_2-CpHydA and rd-TiO_2-CpHydA.

I was mostly interested in understanding the interaction between the oxidic supports and the protein, hence I have characterized for the first time by EPR spectroscopy the behavior of three different TiO_2-hydrogenase hybrid systems under irradiation.

The EPR experiments have demonstrated that anchoring the enzyme on the TiO_2 powders does not affect the H cluster geometry and the catalytic ability of the protein.

Furthermore, the hydrogenase in the hybrid system is a scavenger of photoexcited electrons under irradiation, in fact, these are no more trapped by Ti^{4+} centers as it occurs in the case of the oxide supports in the absence of the protein. This result is relevant since it definitely shows an electron transfer from the TiO_2 to the anchored hydrogenase allowing the H^+ reduction.

The photocatalytic H_2 production tests have demonstrated that the N-TiO_2-CpHydA sample exhibits the highest activity among the other hybrid systems. This is due to the presence of intra band gap that are available to excite the electrons of the valence band to the conduction band even under visible light. This allows the use of a fraction of photons present in the solar light which are not effective in the case of bare TiO_2.

The photocatalytic activity of these systems, especially that obtained for the N-TiO_2-CpHydA sample, are in good agreement with values observed for other TiO_2-[Fe-Fe]hydrogenase photosensitized with a ruthenium dyes and irradiated with visible light.[133] The comparison of the photocatalytic H_2 evolution between the materials investigated in this work and other systems usually employed for water photosplitting tests is not straightforward, since the operating conditions adopted for tests are, most of the case, different from each other.

Anyway, in terms of photocatalytic H_2 evolution, the present work remains a proof of concept. In spite of a quite modest production of $H_{2,}$ however, the hybrid system could have a strong potential in this field since the functionalization of TiO_2 with the protein sustains an H_2 evolution rate at least one order of magnitude higher than that of the bare TiO_2 powders. Hydrogenases, therefore, though delicate to be handling, offer an interesting alternative as low cost co-catalysts to replace expensive co-catalysts based on expensive noble metals.

Conclusions

General conclusions.

The present thesis reports an investigation on a series of systems that can be considered as modifications of the universally known titanium dioxide matrix. This oxide has been modified in composition introducing substantial amounts of Zr^{4+} ions in its bulk attaining the composition of $ZrTiO_4$ (zirconium titanate). This was done with the main goal of verifying if a modification of the flat band potential of the TiO_2 conduction band (moving it at a more negative value owing to the insertion of Zr ions) is able to improve the reduction capability of the solid in photocatalytic reaction e.g., in particular, of H_2 formation by photoreduction of water. The relatively less known $ZrTiO_4$ matrix was then modified in order to induce a visible light sensitivity in this oxide whose band gap corresponds to ultraviolet energy. Two types of dopant have been used that have attracted increasing interest in photocatalysis in the last period. These are nitrogen (a non metallic impurity) and cerium in the form of tetravalent ions.

The other modifications here explored concerned co-catalysts for hydrogen evolution. Co-catalysts are usually coupled to a photoactive oxide for water photosplitting to decrease the activation energy of hydrogen and oxygen evolution reactions (HEC and OEC respectively). In this work, two different types of HEC co-catalysts were investigated in order to find alternative systems to the well-known (and expensive) catalysts based on Pt supported nanoparticles. In the first case an enzymatic catalyst (Fe-Fe hydrogenase) was anchored at the surface of pristine and modified titanium dioxide powders. In the second one, a variety of copper-based systems were supported on TiO_2 and $ZrTiO_4$ according to two different chemical methods. The two types of preparation have been compared in order to shed light on the role of both cuprous oxide and metallic copper particles in the process of hydrogen evolution.

Although the systems based on zirconium titanate show an appreciable photoactivity upon UV-Visible irradiation and a conduction band energy more negative than that of TiO_2, they remain less active than this classic benchmark of photocatalytic systems in the reaction of hydrogen evolution. This confirms that the flat band potential is just one of the parameters to be considered for understanding the photoactivity and the catalytic performance of different semiconductors. It can be inferred that other properties determining the better qualities of TiO_2 (at least in comparison with $ZrTiO_4$) are its higher reducibility (i.e. the propensity to form reduced Ti^{3+} states) and the higher density of states in the conduction band (based on 3d orbitals of Ti^{4+} and not both 3d and 4d like in the case of zirconium titanate).

The doping of $ZrTiO_4$ with nitrogen and cerium ions was proposed to improve the photocactivity of this matrix in the visible range. Surprisingly the doped materials did not show appreciable activity upon irradiation with visible light only. In the case of N-$ZrTiO_4$, this result was due to its low surface area that inhibits the transfer of the photogenerated charge transfer to any adsorbed molecules. The inactivity of Ce-$ZrTiO_4$ upon visible irradiation was also quite surprising considering that, in the case of Ce doped zirconium dioxide, a system with similar electronic structure, a non-negligible photoactivity in the visible range was observed.[123]

The HER co-catalyst tested in this work, namely hydrogenase and the copper based systems, have proved to be valid alternatives to replace expensive Pt nanoparticles. Indeed, although H_2 evolutions are not comparable to each other since the experimental conditions adopted for tests are different, both the systems have provided an H_2 production rate definitely higher than the bare supporting oxides. The enhanced H_2 evolution on the materials modified with hydrogenases is attributed to an efficient electron transfer from the TiO_2 to the protein. In the case of copper-modified material, instead, this work has demonstrate that, beside the favorable effect of the Cu_2O-oxide heterojunction, the formation of metallic copper during the irradiation is fundamental to reach a good H_2 photoevolution.

References

1. Fujishima A. and Honda K., Electrochemical Photolysis of Water at a Semiconductor Electrode. *Nature* **1972**, *238*, 37-38.

2. Kubacka A., Fernández-García M. and Colón G., Advanced Nanoarchitectures for Solar Photocatalytic Applications. *Chem. Rev.* **2012**, *112*, 1555-1614.

3. Linsebigler A. L., Lu G. and Yates Jr J. T., Photocatalysis on TiO_2 Surfaces: Principles, Mechanisms, and Selected Results. *Chem. Rev.* **1995**, *95*, 735-758.

4. Ireland J. C., Klostermann P., Rice E. and Clark R., Inactivation of Escherichia Coli by Titanium Dioxide Photocatalytic Oxidation. *Appl. Environ. Microbiol.* **1993**, *59*, 1668-1670.

5. Cho M., Chung H., Choi W. and Yoon J., Linear Correlation Between Inactivation of E. Coli and OH Radical Concentration in TiO_2 Photocatalytic Disinfection. *Water Res.* **2004**, *38*, 1069-1077.

6. Nozawa M., Tanigawa K., Hosomi M., Chikusa T. and Kawada E., Removal and Decomposition of Malodorants by Using Titanium Dioxide Photocatalyst Supported on Fiber Activated Carbon. *Water Sci. Technol.* **2001**, *44*, 127-133.

7. Mellott N., Durucan C., Pantano C. and Guglielmi M., Commercial and Laboratory Prepared Titanium Dioxide Thin Films for Self-Cleaning Glasses: Photocatalytic Performance and Chemical Durability. *Thin Solid Films* **2006**, *502*, 112-120.

8. O'regan B. and Graetzel M., A Low-Cost, High-Efficiency Solar Cell Based on Dye-Sensitized. *Nature* **1991**, *353*, 737-740.

9. Kojima A., Teshima K., Shirai Y. and Miyasaka T., Organometal Halide Perovskites as Visible-Light Sensitizers for Photovoltaic Cells. *J. Am. Chem. Soc.* **2009**, *131*, 6050-6051.

10. Livraghi S., Paganini M. C., Giamello E., Selloni A., Di Valentin C. and Pacchioni G., Origin of Photoactivity of Nitrogen-Doped Titanium Dioxide under Visible Light. *J. Am. Chem. Soc.* **2006**, *128*, 15666-15671.

11. Gionco C., Paganini M. C., Chiesa M., Maurelli S., Livraghi S. and Giamello E., Cerium Doped Zirconium Dioxide as a Potential New Photocatalytic Material. The Role of the Preparation Method on the Properties of the Material. *Appl. Catal., A* **2015**, *504*, 338-343.

12. Barolo G., Livraghi S., Chiesa M., Paganini M. C. and Giamello E., Mechanism of the Photoactivity under Visible Light of N-doped Titanium Dioxide. Charge Carriers Migration in Irradiated N-TiO_2 Investigated by Electron Paramagnetic Resonance. *J. Phys. Chem. C* **2012**, *116*, 20887-20894.

13. Livraghi S., Chierotti M., Giamello E., Magnacca G., Paganini M., Cappelletti G. and Bianchi C., Nitrogen-Doped Titanium Dioxide Active in

Photocatalytic Reactions with Visible Light: a Multi-Technique Characterization of Differently Prepared Materials. *J. Phys. Chem. C* **2008**, *112*, 17244-17252.

14. Livraghi S., Elghniji K., Czoska A., Paganini M., Giamello E. and Ksibi M., Nitrogen-Doped and Nitrogen–Fluorine-Codoped Titanium Dioxide. Nature and Concentration of the Photoactive Species and Their Role in Determining the Photocatalytic Activity under Visible Light. *J. Photochem. Photobiol., A* **2009**, *205*, 93-97.

15. Wang Q., Chen C., Ma W., Zhu H. and Zhao J., Pivotal Role of Fluorine in Tuning Band Structure and Visible-Light Photocatalytic Activity of Nitrogen-Doped TiO_2. *Chem. Eur. J.* **2009**, *15*, 4765-4769.

16. Vaiano V., Sacco O., Sannino D., Ciambelli P., Longo S., Venditto V. and Guerra G., N-doped TiO_2/s-PS Aerogels for Photocatalytic Degradation of Organic Dyes in Wastewater under Visible Light Irradiation. *J. Chem. Technol. Biotechnol.* **2014**, *89*, 1175-1181.

17. Vaiano V., Sacco O., Sannino D. and Ciambelli P., Process Intensification in the Removal of Organic Pollutants from Wastewater Using Innovative Photocatalysts Obtained Coupling Zinc Sulfide Based Phosphors with Nitrogen Doped Semiconductors. *J. Cleaner Prod.* **2015**, *100*, 208-211.

18. Reisner E., Solar Hydrogen Evolution with Hydrogenases: From Natural to Hybrid Systems. *Eur. J. Inorg. Chem.* **2011**, *2011*, 1005-1016.

19. Dozzi M. V., Chiarello G. L., Pedroni M., Livraghi S., Giamello E. and Selli E., High photocatalytic hydrogen production on Cu(II) pre-grafted Pt/TiO_2. *Appl. Catal., B* **2017**, *209*, 417-428.

20. Jung M., Hart J. N., Scott J., Ng Y. H., Jiang Y. and Amal R., Exploring Cu Oxidation State on TiO_2 and Its Transformation During Photocatalytic Hydrogen Evolution. *Appl. Catal., A* **2016**, *521*, 190-201.

21. Tamiolakis I., Papadas I. T., Spyridopoulos K. C. and Armatas G. S., Mesoporous Assembled Structures of Cu_2O and TiO_2 Nanoparticles for Highly Efficient Photocatalytic Hydrogen Generation from Water. *RSC Adv.* **2016**, *6*, 54848-54855.

22. Liu Y. X., Wang Z. L. and Huang W. X., Influences of TiO_2 Phase Structures on the Structures and Photocatalytic Hydrogen Production of CuO_x/TiO_2 Photocatalysts. *Appl. Surf. Sci.* **2016**, *389*, 760-767.

23. Hu Q. Q., Huang J. Q., Li G. J., Chen J., Zhang Z. J., Deng Z. H., Jiang Y. B., Guo W. and Cao Y. G., Effective Water Splitting Using CuO_x/TiO_2 Composite Films: Role of Cu Species and Content in Hydrogen Generation. *Appl. Surf. Sci.* **2016**, *369*, 201-206.

24. Chen W. T., Jovic V., Sun-Waterhouse D., Idriss H. and Waterhouse G. I. N., The Role of CuO in Promoting Photocatalytic Hydrogen Production over TiO_2. *Int. J. Hydrogen Energy* **2013**, *38*, 15036-15048.

25. Li G., Dimitrijevic N. M., Chen L., Nichols J. M., Rajh T. and Gray K. A., The Important Role of Tetrahedral Ti^{4+} Sites in the Phase Transformation and

Photocatalytic Activity of TiO_2 Nanocomposites. *J. Am. Chem. Soc.* **2008**, *130*, 5402-5403.

26. Chiesa M., Paganini M. C., Livraghi S. and Giamello E., Charge Trapping in TiO_2 Polymorphs as Seen by Electron Paramagnetic Resonance Spectroscopy. *Phys. Chem. Chem. Phys.* **2013**, *15*, 9435-9447.

27. Scanlon D. O., Dunnill C. W., Buckeridge J., Shevlin S. A., Logsdail A. J., Woodley S. M., Catlow C. R. A., Powell M. J., Palgrave R. G., Parkin I. P., Watson G. W., Keal T. W., Sherwood P., Walsh A. and Sokol A. A., Band Alignment of Rutile and Anatase TiO_2. *Nat. Mater.* **2013**, *12*, 798-801.

28. Linsebigler A. L., Lu G. Q. and Yates J. T., Photocatalysis on TiO_2 Surfaces - Principles, Mechanisms, and Selected Results. *Chem. Rev.* **1995**, *95*, 735-758.

29. Chiesa M., Paganini M. C. and Giamello E., EPR of Charge Carriers Stabilized at the Surface of Metal Oxides. *Appl. Magn. Reson.* **2010**, *37*, 605.

30. Livraghi S., Chiesa M., Paganini M. C. and Giamello E., On the Nature of Reduced States in Titanium Dioxide As Monitored by Electron Paramagnetic Resonance. I: The Anatase Case. *J. Phys. Chem. C* **2011**, *115*, 25413-25421.

31. Livraghi S., Rolando M., Maurelli S., Chiesa M., Paganini M. C. and Giamello E., Nature of Reduced States in Titanium Dioxide as Monitored by Electron Paramagnetic Resonance. II: Rutile and Brookite Cases. *J. Phys. Chem. C* **2014**, *118*, 22141-22148.

32. Panarelli E. G., Livraghi S., Maurelli S., Polliotto V., Chiesa M. and Giamello E., Role of Surface Water Molecules in Stabilizing Trapped Hole Centres in Titanium Dioxide (Anatase) as Monitored by Electron Paramagnetic Resonance. *J. Photochem. Photobiol., A* **2016**, *322*, 27-34.

33. Kumar C. P., Gopal N. O., Wang T. C., Wong M. S. and Ke S. C., EPR Investigation of TiO_2 Nanoparticles with Temperature-Dependent Properties. *J. Phys. Chem. B* **2006**, *110*, 5223-5229.

34. Carp O., Huisman C. L. and Reller A., Photoinduced Reactivity of Titanium Dioxide. *Prog. Solid State Chem.* **2004**, *32*, 33-177.

35. Henderson M. A., A Surface Science Perspective on TiO_2 Photocatalysis. *Surf. Sci. Rep.* **2011**, *66*, 185-297.

36. Ondik H. and McMurdie H. F., Phase Diagrams for Zirconium and Zirconia Systems. *Am. Ceram. Soc. Bull.* **2017**.

37. Gallino F., Di Valentin C. and Pacchioni G., Band Gap Engineering of Bulk ZrO_2 by Ti Doping. *Phys. Chem. Chem. Phys.* **2011**, *13*, 17667-17675.

38. Kisi E. H. and Howard C. In *Crystal Structures of Zirconia Phases and Their Inter-Relation*, Key Eng. Mater., Trans Tech Publ: 1998; pp 1-36.

39. Yamaguchi T., Application of ZrO_2 as a Catalyst and a Catalyst Support. *Catal. Today* **1994**, *20*, 199-218.

40. French R. H., Glass S. J., Ohuchi F. S., Xu Y. N. and Ching W. Y., Experimental and Theoretical Determination of the Electronic-Structure and Optical-Properties of 3 Phases of ZrO_2. *Phys. Rev. B* **1994**, *49*, 5133-5141.

41. Gionco C., Paganini M. C., Giamello E., Burgess R., Di Valentin C. and Pacchioni G., Paramagnetic Defects in Polycrystalline Zirconia: An EPR and DFT Study. *Chem. Mater.* **2013**, *25*, 2243-2253.

42. Occhiuzzi M., Cordischi D. and Dragone R., Intrinsic and Extrinsic Paramagnetic Centers in Zirconia. *J. Phys. Chem. B* **2002**, *106*, 12464-12469.

43. Emeline A. V., Panasuk A. V., Sheremetyeva N. and Serpone N., Mechanistic Studies of the Formation of Different States of Oxygen on Irradiated ZrO_2 and the Photocatalytic Nature of Photoprocesses from Determination of Turnover Numbers. *J. Phys. Chem. B* **2005**, *109*, 2785-2792.

44. Ward D. A. and Ko E. I., Synthesis and Structural Transformation of Zirconia Aerogels. *Chem. Mater.* **1993**, *5*, 956-969.

45. Sayama K. and Arakawa H., Photocatalytic Decomposition of Water and Photocatalytic Reduction of Carbon-Dioxide over ZrO_2 Catalyst. *J. Phys. Chem.* **1993**, *97*, 531-533.

46. Xiao M., Li Y. G., Lu Y. F. and Ye Z. Z., Synthesis of ZrO_2: Fe Nanostructures with Visible-Light Driven H_2 Evolution Activity. *J. Mater. Chem. A* **2015**, *3*, 2701-2706.

47. Kohno Y., Tanaka T., Funabiki T. and Yoshida S., Photoreduction of Carbon Dioxide with Hydrogen over ZrO_2. *Chem. Commun.* **1997**, 841-842.

48. Kohno Y., Tanaka T., Funabiki T. and Yoshida S., Identification and Reactivity of a Surface Intermediate in the Photoreduction of CO_2 with H_2 over ZrO_2. *J. Chem. Soc., Faraday Trans.* **1998**, *94*, 1875-1880.

49. Kubo K., Hosokawa S., Furukawa S., Iwamoto S. and Inoue M., Synthesis of ZrO_2-TiO_2 Solid Solutions by Various Synthetic Methods in the Region of High Zirconium Contents. *J. Mater. Sci.* **2008**, *43*, 2198-2205.

50. Zou H. and Lin Y. S., Structural and Surface Chemical Properties of Sol-Gel Derived TiO_2-ZrO_2 Oxides. *Appl. Catal., A* **2004**, *265*, 35-42.

51. Manriquez M. E., Lopez T., Gomez R. and Navarrete J., Preparation of TiO_2-ZrO_2 Mixed Oxides with Controlled Acid-Basic Properties. *J. Mol. Catal. A: Chem.* **2004**, *220*, 229-237.

52. Brown F. H. and Duwez P., The Zirconia-Titania System. *J. Am. Ceram. Soc.* **1954**, *37*, 129-132.

53. Noguchi T. and Mizuno M., Phase Changes in the ZrO_2-TiO_2 System. *Bull. Chem. Soc. Jpn.* **1968**, *41*, 2895-2899.

54. Yamaguchi O. and Mogi H., Formation of Zirconia Titanate Solid Solution from Alkoxides. *J. Am. Ceram. Soc.* **1989**, *72*, 1065-1066.

55. McHale A. and Roth R. S., Low-Temperature Phase Relationships in the System ZrO_2-TiO_2. *J. Am. Ceram. Soc.* **1986**, *69*, 827-832.

56. Troitzsch U. and Ellis D. J., The ZrO_2-TiO_2 Phase Diagram. *J. Mater. Sci.* **2005**, *40*, 4571-4577.

57. Christoffersen R. and Davies P. K., Structure of Commensurate and Incommensurate Ordered Phases in the System $ZrTiO_4$–$Zr_5Ti_7O_{24}$. *J. Am. Ceram. Soc.* **1992**, *75*, 563-569.

58. Bianco A., Paci M. and Freer R., Zirconium Titanate: from Polymeric Precursors to Bulk Ceramics. *J. Eur. Ceram. Soc.* **1998**, *18*, 1235-1243.

59. Livraghi S., Olivero F., Paganini M. C. and Giamello E., Titanium Ions Dispersed into the ZrO_2 Matrix: Spectroscopic Properties and Photoinduced Electron Transfer. *J. Phys. Chem. C* **2010**, *114*, 18553-18558.

60. Gionco C., Battiato A., Vittone E., Paganini M. C. and Giamello E., Structural and Spectroscopic Properties of High Temperature Prepared ZrO_2-TiO_2 mixed oxides. *J. Solid State Chem.* **2013**, *201*, 222-228.

61. Neppolian B., Wang Q., Yamashita H. and Choi H., Synthesis and Characterization of ZrO_2-TiO_2 Binary Oxide Semiconductor Nanoparticles: Application and Interparticle Electron Transfer Process. *Appl. Catal., A* **2007**, *333*, 264-271.

62. Chang R. C. and Wang I., Surface-Acidity and Basicity of TiO_2-ZrO_2-V_2O_5 - Dehydrogenation and Isomerization of Cyclohexane. *J. Catal.* **1987**, *107*, 195-200.

63. Fling J. and Wang I., Dehydrocyclization of C_6-C_8 *n*-paraffins to Aromatics over TiO_2-ZrO_2 Catalysts. *J. Catal.* **1991**, *130*, 577-587.

64. Arata K., Akutagawa S. and Tanabe K., Epoxide Rearrangement III. Isomerization of 1-Methylcyclohexene Oxide over TiO_2–ZrO_2, $NiSO_4$ and $FeSO_4$. *Bull. Chem. Soc. Jpn.* **1976**, *49*, 390-393.

65. Tanabe K. and Yamaguchi T., Acid-Base Bifunctional Catalysis by ZrO_2 and Its Mixed Oxides. *Catal. Today* **1994**, *20*, 185-197.

66. Liu S. W., Song C. F., Lu M. K., Wang S. F., Sun D. L., Qi Y. X., Xu D. and Yuan D. R., A Novel $TiO_2/Zr_xTi_{1-x}O_2$ Composite Photocatalytic Films. *Catal. Commun.* **2003**, *4*, 343-346.

67. Fresno F., Hernandez-Alonso M. D., Tudela D., Coronado J. M. and Soria J., Photocatalytic Degradation of Toluene over Doped and Coupled $(Ti,M)O_2$ (M = Sn or Zr) Nanocrystalline Oxides: Influence of the Heteroatom Distribution on Deactivation. *Appl. Catal., B* **2008**, *84*, 598-606.

68. Hernández-Alonso M. D., Tejedor-Tejedor I., Coronado J. M., Anderson M. A. and Soria J., Operando FTIR Study of the Photocatalytic Oxidation of Acetone in Air over TiO_2–ZrO_2 Thin Films. *Catal. Today* **2009**, *143*, 364-373.

69. Gnatyuk Y., Smirnova N., Korduban O. and Eremenko A., Effect of Zirconium Incorporation on the Stabilization of TiO_2 Mesoporous Structure. *Surf. Interface Anal.* **2010**, *42*, 1276-1280.

70. Yu J. C., Lin J. and Kwok R. W. M., $Ti_{1-x}Zr_xO_2$ Solid Solutions for the Photocatalytic Degradation of Acetone in Air. *J. Phys. Chem. B* **1998**, *102*, 5094-5098.

71. Hernandez-Alonso M. D., Coronado J. M., Bachiller-Baeza B., Fernandez-Garcia M. and Soria J., Influence of Structural and Surface Characteristics of $Ti_{1-x}Zr_xO_2$ Nanoparticles on the Photocatalytic Degradation of Methylcyclohexane in the Gas Phase. *Chem. Mater.* **2007**, *19*, 4283-4291.

72. Wang J. S., Yu Y. L., Li S., Guo L. M., Wang E. J. and Cao Y. A., Doping Behavior of Zr^{4+} Ions in Zr^{4+}-Doped TiO_2 Nanoparticles. *J. Phys. Chem. C* **2013**, *117*, 27120-27126.
73. Troitzsch U., Christy A. G. and Ellis D. J., The Crystal Structure of Disordered $(Zr,Ti)O_2$ Solid Solution Including Srilankite: Evolution Towards Tetragonal ZrO_2 with increasing Zr. *Phys. Chem. Miner.* **2005**, *32*, 504-514.
74. Newnham R., Crystal Structure of ZrTiO4. *J. Am. Ceram. Soc.* **1967**, *50*, 216-216.
75. Pol S., Pol V., Gedanken A., Spijksma G., Grinblat J., Selvan R. K., Kessler V., Seisenbaeva G. and Gohil S., Synthesis of Nanocrystalline Zirconium Titanate and Its Dielectric Properties. *J. Phys. Chem. C* **2007**, *111*, 2484-2489.
76. Kim D.-S., Park D.-H., Kim G.-D. and Choi S.-Y., Dielectric Properties of $ZrTiO_4$ Thin Films Synthesized by Sol-Gel Method. *Met. Mater. Int.* **2004**, *10*, 361-365.
77. Lessing P., Yang Z., Miller G. and Yamada H., Corrosion of Metal Oxide Ceramics in Molten Lithium-Potassium Carbonates. *J. Electrochem. Soc.* **1988**, *135*, 1049-1057.
78. Park Y., $Zr_{0.98}Sn_{0.02}TiO_4$ Single Crystal in a Low Electric Field: Birefringence, Dielectric, and Synchrotron X-Ray Studies. *Phys. Rev. B* **2000**, *62*, 8794-8801.
79. Leoni M., Viviani M., Battilana G., Fiorello A. M. and Viticoli M., Aqueous Synthesis and Sintering of Zirconium Titanate Powders for Microwave Components. *J. Eur. Ceram. Soc.* **2001**, *21*, 1739-1741.
80. Bianco A., Gusmano G., Freer R. and Smith P., Zirconium Titanate Microwave Dielectrics Prepared Via Polymeric Precursor Route. *J. Eur. Ceram. Soc.* **1999**, *19*, 959-963.
81. Chang D. A., Lin P. and Tseng T. Y., Optical Properties of $ZrTiO_4$ Films Grown by Radio-Frequency Magnetron Sputtering. *J. Appl. Phys.* **1995**, *77*, 4445-4451.
82. Hsu C.-H. and Lin S.-Y., Characterization of $ZrTiO_4$ Thin Films Prepared by Sol-Gel Method. *Mater. Sci. Semicond. Process.* **2013**, *16*, 1262-1266.
83. Cosentino I. C., Muccillo E. N. S. and Muccillo R., Development of Zirconia-Titania Porous Ceramics for Humidity Sensors. *Sens. Actuators, B* **2003**, *96*, 677-683.
84. Dondi M., Matteucci F. and Cruciani G., Zirconium Titanate Ceramic Pigments: Crystal Structure, Optical Spectroscopy and Technological Properties. *J. Solid State Chem.* **2006**, *179*, 233-246.
85. Devi K. B., Singh K. and Rajendran N., Sol-Gel Synthesis and Characterisation of Nanoporous Zirconium Titanate Coated on 316L SS for Biomedical Applications. *J. Sol-Gel Sci. Technol.* **2011**, *59*, 513-520.
86. Navio J. and Colòn G., Heterogeneous Photocatalytic Oxidation of Liquid Isopropanol by TiO_2, ZrO_2 And $ZrTiO_4$ Powders. *Stud. Surf. Sci. Catal.* **1994**, *82*, 721-728.

87. Navio J., Colon G. and Herrmann J., Photoconductive and Photocatalytic Properties of $ZrTiO_4$. Comparison with the Parent Oxides TiO_2 and ZrO_2. *J. Photochem. Photobiol., A* **1997**, *108*, 179-185.

88. Navio J., Hidalgo M., Roncel M. and De la Rosa M., A Laser Flash Photolysis Study of the Photochemical Activity of a Synthesised $ZrTiO_4$: Comparison with Parent Oxides, TiO_2 and ZrO_2. *Mater. Lett.* **1999**, *39*, 370-373.

89. Manrìquez M., Lòpez T., Aguilar D. and Quintana P., Phase Structure and Thermal Evolution in Mixed Oxide TiO_2-ZrO_2 Powders Obtained by the Sol-Gel Process. In *Emerging Fields in Sol-Gel Science and Technology*, Springer: 2003; pp 254-264.

90. Bingham S. and Daoud W. A., Recent Advances in Making Nano-sized TiO_2 Visible-light Active through Rare-earth Metal Doping. *J. Mater. Chem.* **2011**, *21*, 2041-2050.

91. Wang X., Li J.-G., Kamiyama H., Katada M., Ohashi N., Moriyoshi Y. and Ishigaki T., Pyrogenic Iron(III)-Doped TiO_2 Nanopowders Synthesized in RF Thermal Plasma: Phase Formation, Defect Structure, Band Gap, and Magnetic Properties. *J. Am. Chem. Soc.* **2005**, *127*, 10982-10990.

92. Diebold U., The Surface Science of Titanium Dioxide. *Surf. Sci. Rep.* **2003**, *48*, 53-229.

93. Di Valentin C., Pacchioni G. and Selloni A., Theory of Carbon Doping of Titanium Dioxide. *Chem. Mater.* **2005**, *17*, 6656-6665.

94. Umebayashi T., Yamaki T., Itoh H. and Asai K., Band Gap Narrowing of Titanium Dioxide by Sulfur Doping. *Appl. Phys. Lett.* **2002**, *81*, 454-456.

95. Sakthivel S. and Kisch H., Photocatalytic and Photoelectrochemical Properties of Nitrogen-Doped Titanium Dioxide. *ChemPhysChem* **2003**, *4*, 487-490.

96. Xu A. W., Gao Y. and Liu H. Q., The Preparation, Characterization, and Their Photocatalytic Activities of Rare-Earth-Doped TiO_2 Nanoparticles. *J. Catal.* **2002**, *207*, 151-157.

97. Li J. H., Yang X., Yu X. D., Xu L. L., Kang W. L., Yan W. H., Gao H. F., Liu Z. H. and Guo Y. H., Rare Earth Oxide-Doped Titania Nanocomposites with Enhanced Photocatalytic Activity towards the Degradation of Partially Hydrolysis Polyacrylamide. *Appl. Surf. Sci.* **2009**, *255*, 3731-3738.

98. Asahi R., Morikawa T., Irie H. and Ohwaki T., Nitrogen-Doped Titanium Dioxide as Visible-Light-Sensitive Photocatalyst: Designs, Developments, and Prospects. *Chem. Rev.* **2014**, *114*, 9824-9852.

99. Chavillon B., Cario L., Renaud A., Tessier F., Chevire F., Boujtita M., Pellegrin Y., Blart E., Smeigh A., Hammarstrom L., Odobel F. and Jobic S., P-Type Nitrogen-Doped ZnO Nanoparticles Stable under Ambient Conditions. *J. Am. Chem. Soc.* **2012**, *134*, 464-470.

100. Wu K., Jiang J., Tang K., Gu S., Ye J., Zhu S., Lu K., Zhou M., Xu M., Zhang R. and Zheng Y., Influences of the Type of Dopant and Substrate on Ferromagnetism in ZnO:Mn. *J. Magn. Magn. Mater.* **2014**, *355*, 51-57.

101. Yang X., Wolcott A., Wang G., Sobo A., Fitzmorris R. C., Qian F., Zhang J. Z. and Li Y., Nitrogen-Doped ZnO Nanowire Arrays for Photoelectrochemical Water Splitting. *Nano Lett.* **2009**, *9*, 2331-2336.

102. von Wenckstern H., Schmidt H., Brandt M., Lajn A., Pickenhain R., Lorenz M., Grundmann M., Hofmann D. M., Polity A., Meyer B. K., Saal H., Binnewies M., Börger A., Becker K. D., Tikhomirov V. A. and Jug K., Anionic and Cationic Substitution in ZnO. *Prog. Solid State Chem.* **2009**, *37*, 153-172.

103. Suzuki T. M., Saeki S., Sekizawa K., Kitazumi K., Takahashi N. and Morikawa T., Photoelectrochemical Hydrogen Production by Water Splitting over Dual-Functionally Modified Oxide: p-Type N-doped Ta_2O_5 Photocathode Active under Visible Light Irradiation. *Appl. Catal., B* **2017**, *202*, 597-604.

104. Livraghi S., Barbero N., Agnoli S., Barolo C., Granozzi G., Sauvage F. and Giamello E., A Multi-Technique Comparison of the Electronic Properties of Pristine and Nitrogen-Doped Polycrystalline SnO_2. *Phys. Chem. Chem. Phys.* **2016**, *18*, 22617-22627.

105. Ogale S. B., Dilute Doping, Defects, and Ferromagnetism in Metal Oxide Systems. *Adv. Mater.* **2010**, *22*, 3125-3155.

106. Elfimov I. S., Rusydi A., Csiszar S. I., Hu Z., Hsieh H. H., Lin H. J., Chen C. T., Liang R. and Sawatzky G. A., Magnetizing Oxides by Substituting Nitrogen for Oxygen. *Phys. Rev. Lett.* **2007**, *98*, 137202.

107. Gallino F., Di Valentin C., Pacchioni G., Chiesa M. and Giamello E., Nitrogen Impurity States in Polycrystalline ZnO. A Combined EPR and Theoretical Study. *J. Mater. Chem.* **2010**, *20*, 689-697.

108. Garces N. Y., Wang L. J., Giles N. C., Halliburton L. E., Cantwell G. and Eason D. B., Molecular nitrogen (N_2^-) acceptors and isolated nitrogen (N^-) acceptors in ZnO crystals. *J. Appl. Phys.* **2003**, *94*, 519-524.

109. Livraghi S., Czoska A. M., Paganini M. C. and Giamello E., Preparation and Spectroscopic Characterization of Visible Light Sensitized N Doped TiO_2 (Rutile). *J. Solid State Chem.* **2009**, *182*, 160-164.

110. Takeuchi M., Shimizu Y., Yamagawa H., Nakamuro T. and Anpo M., Preparation of the Visible Light Responsive N^{3-}-Doped WO_3 Photocatalyst by a Thermal Decomposition of Ammonium Paratungstate. *Appl. Catal., B* **2011**, *110*, 1-5.

111. Vemuri R. S., Noor-A-Alam M., Gullapalli S. K., Engelhard M. H. and Ramana C. V., Nitrogen-Incorporation Induced Changes in the Microstructure of Nanocrystalline WO_3 Thin Films. *Thin Solid Films* **2011**, *520*, 1446-1450.

112. Albanese E., Di Valentin C., Pacchioni G., Sauvage F., Livraghi S. and Giamello E., Nature of Paramagnetic Species in Nitrogen-Doped SnO_2: A Combined Electron Paramagnetic Resonance and Density Functional Theory Study. *J. Phys. Chem. C* **2015**, *119*, 26895-26903.

113. Sun X., Long R., Cheng X., Zhao X., Dai Y. and Huang B., Structural, Electronic, and Optical Properties of N-doped SnO_2. *J. Phys. Chem. C* **2008**, *112*, 9861-9864.

114. Zhu H., Li J., Chen K., Yi X., Cheng S. and Gan F., Nature of Charge Transport and p-Electron Ferromagnetism in Nitrogen-Doped ZrO_2: An Ab Initio Perspective. *Sci. Rep.* **2015**, *5*, 8586.

115. Wang X., Yu J. C., Chen Y., Wu L. and Fu X., ZrO_2-Modified Mesoporous Nanocrystalline $TiO_{2-x}N_x$ as Efficient Visible Light Photocatalysts. *Environ. Sci. Technol.* **2006**, *40*, 2369-2374.

116. Qiu X. F., Zhao Y. X. and Burda C., Synthesis and Characterization of Nitrogen-Doped Group IVB Visible-Light-Photoactive Metal Oxide Nanoparticles. *Adv. Mater.* **2007**, *19*, 3995-3999.

117. Gionco C., Paganini M. C., Agnoli S., Reeder A. E. and Giamello E., Structural and Spectroscopic Characterization of CeO_2-TiO_2 Mixed Oxides. *J. Mater. Chem. A* **2013**, *1*, 10918-10926.

118. Silva A. M. T., Silva C. G., Drazic G. and Faria J. L., Ce-doped TiO_2 for Photocatalytic Degradation of Chlorophenol. *Catal. Today* **2009**, *144*, 13-18.

119. Xu J. J., Ao Y. H. and Fu D. G., A Novel Ce, C-Codoped TiO_2 Nanoparticles and Its Photocatalytic Activity under Visible Light. *Appl. Surf. Sci.* **2009**, *256*, 884-888.

120. Tong T. Z., Zhang J. L., Tian B. Z., Chen F., He D. N. and Anpo M., Preparation of Ce-TiO_2 Catalysts by Controlled Hydrolysis of Titanium Alkoxide Based on Esterification Reaction and Study on Its Photocatalytic Activity. *J. Colloid Interface Sci.* **2007**, *315*, 382-388.

121. Xu Y. H., Chen H. R., Zeng Z. X. and Lei B., Investigation on Mechanism of Photocatalytic Activity Enhancement of Nanometer Cerium-Doped Titania. *Appl. Surf. Sci.* **2006**, *252*, 8565-8570.

122. Gionco C., Giamello E., Mino L. and Paganini M. C., The Interaction of Oxygen with the Surface of CeO_2-TiO_2 Mixed Systems: an Example of Fully Reversible Surface-to-Molecule Electron Transfer. *Phys. Chem. Chem. Phys.* **2014**, *16*, 21438-21445.

123. Gionco C., Paganini M. C., Giamello E., Burgess R., Di Valentin C. and Pacchioni G., Cerium-Doped Zirconium Dioxide, a Visible-Light-Sensitive Photoactive Material of Third Generation. *J. Phys. Chem. Lett.* **2014**, *5*, 447-451.

124. Ran J. R., Zhang J., Yu J. G., Jaroniec M. and Qiao S. Z., Earth-Abundant Cocatalysts for Semiconductor-Based Photocatalytic Water Splitting. *Chem. Soc. Rev.* **2014**, *43*, 7787-7812.

125. Hara M., Nunoshige J., Takata T., Kondo J. N. and Domen K., Unusual Enhancement of H_2 Evolution by Ru on TaON Photocatalyst under Visible Light Irradiation. *Chem. Commun.* **2003**, 3000-3001.

126. Sayed F. N., Jayakumar O. D., Sasikala R., Kadam R. M., Bharadwaj S. R., Kienle L., Schurmann U., Kaps S., Adelung R., Mittal J. P. and Tyagi A. K., Photochemical Hydrogen Generation Using Nitrogen-Doped TiO_2-Pd Nanoparticles: Facile Synthesis and Effect of Ti^{3+} Incorporation. *J. Phys. Chem. C* **2012**, *116*, 12462-12467.

127. Yu J. G., Qi L. F. and Jaroniec M., Hydrogen Production by Photocatalytic Water Splitting over Pt/TiO_2 Nanosheets with Exposed (001) Facets. *J. Phys. Chem. C* **2010**, *114*, 13118-13125.

128. Murdoch M., Waterhouse G. I. N., Nadeem M. A., Metson J. B., Keane M. A., Howe R. F., Llorca J. and Idriss H., The Effect of Gold Loading and Particle Size on Photocatalytic Hydrogen Production from Ethanol over Au/TiO_2 Nanoparticles. *Nat. Chem.* **2011**, *3*, 489-492.

129. Onsuratoom S., Puangpetch T. and Chavadej S., Comparative Investigation of Hydrogen Production over Ag-, Ni-, and Cu-Loaded Mesoporous-Assembled TiO_2–ZrO_2 Mixed Oxide Nanocrystal Photocatalysts. *Chem. Eng. J.* **2011**, *173*, 667-675.

130. Bi F., Ehsan M. F., Liu W. and He T., Visible-Light Photocatalytic Conversion of Carbon Dioxide into Methane Using Cu_2O/TiO_2 Hollow Nanospheres. *Chin. J. Chem .* **2015**, *33*, 112-118.

131. Helaili N., Bessekhouad Y., Bouguelia A. and Trari M., Visible Light Degradation of Orange II Using $x$$Cu_yO_z$/$TiO_2$ Heterojunctions. *J. Hazard. Mater.* **2009**, *168*, 484-492.

132. King P. W., Designing Interfaces of Hydrogenase-Nanomaterial Hybrids for Efficient Solar Conversion. *Biochim. Biophys. Acta* **2013**, *1827*, 949-957.

133. Reisner E., Powell D. J., Cavazza C., Fontecilla-Camps J. C. and Armstrong F. A., Visible Light-Driven H_2 Production by Hydrogenases Attached to Dye-Sensitized TiO_2 Nanoparticles. *J. Am. Chem. Soc.* **2009**, *131*, 18457-18466.

134. Morra S., Valetti F., Sadeghi S. J., King P. W., Meyer T. and Gilardi G., Direct Electrochemistry of an [FeFe]-Hydrogenase on a TiO_2 Electrode. *Chem. Commun.* **2011**, *47*, 10566-10568.

135. Nikandrov V. V., Shlyk M. A., Zorin N. A., Gogotov I. N. and Krasnovsky A. A., Efficient Photoinduced Electron-Transfer from Inorganic Semiconductor TiO_2 to Bacterial Hydrogenase. *FEBS Lett.* **1988**, *234*, 111-114.

136. Cuendet P., Rao K. K., Graetzel M. and Hall D. O., Light-Induced H_2 Evolution in a Hydrogenase-TiO_2 Particle System by Direct Electron-transfer or via Rhodium Complexes. *Biochimie* **1986**, *68*, 217-221.

137. Li Q., Meng H., Zhou P., Zheng Y. Q., Wang J., Yu J. G. and Gong J. R., $Zn_{1-x}Cd_xS$ Solid Solutions with Controlled Bandgap and Enhanced Visible-Light Photocatalytic H_2 Production Activity. *ACS Catal.* **2013**, *3*, 882-889.

138. Kim S., Lu D., Park S. and Wang G., Production of Hydrogenases as Biocatalysts. *Int. J. Hydrogen Energy* **2012**, *37*, 15833-15840.

139. Lubitz W., Ogata H., Ruediger O. and Reijerse E., Hydrogenases. *Chem. Rev.* **2014**, *114*, 4081-4148.

140. Vignais P. M. and Billoud B., Occurrence, Classification, and Biological Function of Hydrogenases: An Overview. *Chem. Rev.* **2007**, *107*, 4206-4272.

141. Fontecilla-Camps J. C., Volbeda A., Cavazza C. and Nicolet Y., Structure/Function Relationships of [NiFe]- and [FeFe]-Hydrogenases. *Chem. Rev.* **2007**, *107*, 4273-4303.

142. Lubitz W., Reijerse E. J. and Messinger J., Solar Water-Splitting into H_2 and O_2: Design Principles of Photosystem II and Hydrogenases. *Energy Environ. Sci.* **2008**, *1*, 15-31.

143. Adamska A., Silakov A., Lambertz C., Ruediger O., Happe T., Reijerse E. and Lubitz W., Identification and Characterization of the "Super-Reduced" State of the H-Cluster in [FeFe] Hydrogenase: A New Building Block for the Catalytic Cycle? *Angew. Chem. Int. Ed.* **2012**, *51*, 11458-11462.

144. Silakov A., Kamp C., Reijerse E., Happe T. and Lubitz W., Spectroelectrochemical Characterization of the Active Site of the [FeFe] Hydrogenase HydA1 from *Chlamydomonas Reinhardtii*. *Biochemistry* **2009**, *48*, 7780-7786.

145. Mulder D. W., Ratzloff M. W., Shepard E. M., Byer A. S., Noone S. M., Peters J. W., Broderick J. B. and King P. W., EPR and FTIR Analysis of the Mechanism of H_2 Activation by [FeFe]-Hydrogenase HydA1 from *Chlamydomonas Reinhardtii*. *J. Am. Chem. Soc.* **2013**, *135*, 6921-6929.

146. Bennett B., Lemon B. J. and Peters J. W., Reversible Carbon Monoxide Binding and Inhibition at the Active Site of the Fe-only Hydrogenase. *Biochemistry* **2000**, *39*, 7455-7460.

147. von Abendroth G., Stripp S., Silakov A., Croux C., Soucaille P., Girbal L. and Happe T., Optimized Over-Expression of [FeFe] Hydrogenases with High Specific Activity in *Clostridium Acetobutylicum*. *Int. J. Hydrogen Energy* **2008**, *33*, 6076-6081.

148. Yang J. H., Wang D. G., Han H. X. and Li C., Roles of Cocatalysts in Photocatalysis and Photoelectrocatalysis. *Acc. Chem. Res.* **2013**, *46*, 1900-1909.

149. Khan M. R., Chuan T. W., Yousuf A., Chowdhury M. N. K. and Cheng C. K., Schottky Barrier and Surface Plasmonic Resonance Phenomena Towards the Photocatalytic Reaction: Study of Their Mechanisms to Enhance Photocatalytic Activity. *Catal. Sci. Technol.* **2015**, *5*, 2522-2531.

150. Sreethawong T. and Yoshikawa S., Enhanced Photocatalytic Hydrogen Evolution over Pt Supported on Mesoporous TiO_2 Prepared by Single-Step Sol–Gel Process with Surfactant Template. *Int. J. Hydrogen Energy* **2006**, *31*, 786-796.

151. Naldoni A., D'Arienzo M., Altomare M., Marelli M., Scotti R., Morazzoni F., Selli E. and Dal Santo V., Pt and Au/TiO_2 Photocatalysts for Methanol Reforming: Role of Metal Nanoparticles in Tuning Charge Trapping Properties and Photoefficiency. *Appl. Catal., B* **2013**, *130*, 239-248.

152. Yu J. G., Yue L., Liu S. W., Huang B. B. and Zhang X. Y., Hydrothermal Preparation and Photocatalytic Activity of Mesoporous Au-TiO_2 Nanocomposite Microspheres. *J. Colloid Interface Sci.* **2009**, *334*, 58-64.

153. Gombac V., Sordelli L., Montini T., Delgado J. J., Adamski A., Adami G., Cargnello M., Bernal S. and Fornasiero P., CuO_x-TiO_2 Photocatalysts for H_2 Production from Ethanol and Glycerol Solutions. *J. Phys. Chem. A* **2010**, *114*, 3916-3925.
154. Jung M., Scott J., Ng Y. H., Jiang Y. J. and Amal R., CuO_x Dispersion and Reducibility on TiO_2 and Its Impact on Photocatalytic Hydrogen Evolution. *Int. J. Hydrogen Energy* **2014**, *39*, 12499-12506.
155. Lalitha K., Sadanandam G., Kumari V. D., Subrahmanyam M., Sreedhar B. and Hebalkar N. Y., Highly Stabilized and Finely Dispersed Cu_2O/TiO_2: A Promising Visible Sensitive Photocatalyst for Continuous Production of Hydrogen from Glycerol:Water Mixtures. *J. Phys. Chem. C* **2010**, *114*, 22181-22189.
156. Lee S. S., Bai H. W., Liu Z. Y. and Sun D. D., Optimization and an Insightful Properties-Activity study of Electrospun TiO_2/CuO Composite Nanofibers for Efficient Photocatalytic H_2 Generation. *Appl. Catal., B* **2013**, *140*, 68-81.
157. Sreethawong T. and Yoshikawa S., Comparative Investigation on Photocatalytic Hydrogen Evolution over Cu-, Pd-, and Au-Loaded Mesoporous TiO_2 Photocatalysts. *Catal. Commun.* **2005**, *6*, 661-668.
158. Xu S. P. and Sun D. D., Significant Improvement of Photocatalytic Hydrogen Generation Rate over TiO_2 with Deposited CuO. *Int. J. Hydrogen Energy* **2009**, *34*, 6096-6104.
159. Irie H., Kamiya K., Shibanuma T., Miura S., Tryk D. A., Yokoyama T. and Hashimoto K., Visible Light-Sensitive Cu(II)-Grafted TiO_2 Photocatalysts: Activities and X-ray Absorption Fine Structure Analyses. *J. Phys. Chem. C* **2009**, *113*, 10761-10766.
160. Bandara J., Udawatta C. P. K. and Rajapakse C. S. K., Highly Stable CuO Incorporated TiO_2 Catalyst for Photocatalytic Hydrogen Production from H_2O. *Photochem. Photobiol. Sci.* **2005**, *4*, 857-861.
161. Hou H. L., Shang M. H., Gao F. M., Wang L., Liu Q., Zheng J. J., Yang Z. B. and Yang W. Y., Highly Efficient Photocatalytic Hydrogen Evolution in Ternary Hybrid TiO_2/CuO/Cu Thoroughly Mesoporous Nanofibers. *ACS Appl. Mater. Interfaces* **2016**, *8*, 20128-20137.
162. Yu J., Hai Y. and Jaroniec M., Photocatalytic Hydrogen Production over CuO-Modified Titania. *J. Colloid Interface Sci.* **2011**, *357*, 223-228.
163. Huang L., Peng F. and Ohuchi F. S., "In situ" XPS Study of Band Structures at Cu_2O/TiO_2 Heterojunctions Interface. *Surf. Sci.* **2009**, *603*, 2825-2834.
164. Xi Z. H., Li C. J., Zhang L., Xing M. Y. and Zhang J. L., Synergistic Effect of Cu_2O/TiO_2 Heterostructure Nanoparticle and Its High H_2 Evolution Activity. *Int. J. Hydrogen Energy* **2014**, *39*, 6345-6353.

165. Hirano K., Inoue K. and Yatsu T., Photocatalyzed Reduction of CO_2 in Aqueous TiO_2 Suspension Mixed with Copper-Powder. *J. Photochem. Photobiol., A* **1992**, *64*, 255-258.
166. Montini T., Gombac V., Sordelli L., Delgado J. J., Chen X. W., Adami G. and Fornasiero P., Nanostructured Cu/TiO_2 Photocatalysts for H_2 Production from Ethanol and Glycerol Aqueous Solutions. *ChemCatChem* **2011**, *3*, 574-577.
167. Lv X. J., Zhou S. X., Zhang C., Chang H. X., Chen Y. and Fu W. F., Synergetic Effect of Cu and Graphene as Cocatalyst on TiO_2 for Enhanced Photocatalytic Hydrogen Evolution from Solar Water Splitting. *J. Mater. Chem.* **2012**, *22*, 18542-18549.
168. Tian H., Kang S.-Z., Li X., Qin L., Ji M. and Mu J., Fabrication of an Efficient Noble Metal-Free TiO_2-Based Photocatalytic System Using Cu–Ni Bimetallic Deposit as an Active Center of H_2 Evolution from Water. *Sol. Energy Mater. Sol. Cells* **2015**, *134*, 309-317.
169. Ni D., Shen H., Li H., Ma Y. and Zhai T., Synthesis of High Efficient Cu/TiO_2 Photocatalysts by Grinding and Their Size-Dependent Photocatalytic Hydrogen Production. *Appl. Surf. Sci.* **2017**, *409*, 241-249.
170. Morra S., Mongili B., Maurelli S., Gilardi G. and Valetti F., Isolation and Characterization of a New [FeFe]-Hydrogenase from *Clostridium Perfringens*. *Biotechnol. Appl. Biochem.* **2015**, 1-7.
171. Bernal S., Botana F. J., Calvino J. J., Lòpez-Cartes C., Pérez-Omil J. A. and Rodrìguez-Izquierdo J. M., The Interpretation of HRTEM Images of Supported Metal Catalysts Using Image Simulation: Profile View Images. *Ultramicroscopy* **1998**, *72*, 135-164.
172. Pérez-Omil J. A. Doctoral Thesis. University of Cádiz, Spain, 1994.
173. Lee S. W., Obregon S. and Rodriguez-Gonzalez V., The Role of Silver Nanoparticles Functionalized on TiO_2 for Photocatalytic Disinfection of Harmful Algae. *RSC Adv.* **2015**, *5*, 44470-44475.
174. Berger T., Diwald O., Knozinger E., Napoli F., Chiesa M. and Giamello E., Hydrogen Activation at TiO_2 Anatase Nanocrystals. *Chem. Phys.* **2007**, *339*, 138-145.
175. Siggel A. and Jansen M., $ZrSn_{0.5}Ti_{0.5}O_4$ as a Matrix for Ceramic Colors-Structural Investigations on $ZrTiO_4$ $ZrSn_{0.5}Ti_{0.5}O_4$ *Z. Anorg. Allg. Chem.* **1990**, *582*, 93-102.
176. Butler M. A. and Ginley D. S., Prediction of Flatband Potentials at Semiconductor-Electrolyte Interfaces from Atomic Electronegativities. *J. Electrochem. Soc.* **1978**, *125*, 228-232.
177. Marschall R., Semiconductor Composites: Strategies for Enhancing Charge Carrier Separation to Improve Photocatalytic Activity. *Adv. Funct. Mater.* **2014**, *24*, 2421-2440.
178. Li J. T. and Wu N. Q., Semiconductor-Based Photocatalysts and Photoelectrochemical Cells for Solar Fuel Generation: a Review. *Catal. Sci. Technol.* **2015**, *5*, 1360-1384.

179. Chen X. B., Li C., Gratzel M., Kostecki R. and Mao S. S., Nanomaterials for Renewable Energy Production and Storage. *Chem. Soc. Rev.* **2012**, *41*, 7909-7937.

180. Calatayud M., Markovits A., Menetrey M., Mguig B. and Minot C., Adsorption on Perfect and Reduced Surfaces of Metal Oxides. *Catal. Today* **2003**, *85*, 125-143.

181. Albanese E., Leccese M., Di Valentin C. and Pacchioni G., Magnetic Properties of Nitrogen-Doped ZrO_2: Theoretical Evidence of Absence of Room Temperature Ferromagnetism. *Sci. Rep.* **2016**, *6*, 31435.

182. Anpo M., Che M., Fubini B., Garrone E., Giamello E. and Paganini M. C., Generation of Superoxide Ions at Oxide Surfaces. *Top. Catal.* **1999**, *8*, 189-198.

183. Adamski A., Spałek T. and Sojka Z., Application of EPR Spectroscopy for Elucidation of Vanadium Speciation in VO_x /ZrO_2 Catalysts Subject to Redox Treatment. *Res. Chem. Intermed.* **2003**, *29*, 793-804.

184. Polliotto V., Albanese E., Livraghi S., Indyka P., Sojka Z., Pacchioni G. and Giamello E., Fifty-Fifty Zr-Ti Solid Solution with a TiO_2-Type Structure: Electronic Structure and Photochemical Properties of Zirconium Titanate $ZrTiO_4$. *J. Phys. Chem. C* **2017**, *121,* , 5487-5497.

185. Weckhuysen B. M. and Schoonheydt R. A., Recent Progress in Diffuse Reflectance Spectroscopy of Supported Metal Oxide Catalysts. *Catal. Today* **1999**, *49*, 441-451.

186. Martra G., Gianotti E. and Coluccia S., The Application of UV-Visible-NIR Spectroscopy to Oxides. In *Metal Oxide Catalysis*, Wiley-VCH Verlag GmbH & Co. KGaA: 2009; pp 51-94.

187. Fitzpatrick J. A. J., Manby F. R. and Western C. M., The Interpretation of Molecular Magnetic Hyperfine Interactions. *J. Chem. Phys.* **2005**, *122*, 084312–084324.

188. Di Valentin C., Finazzi E., Pacchioni G., Selloni A., Livraghi S., Paganini M. C. and Giamello E., N-Doped TiO_2: Theory and Experiment. *Chem. Phys.* **2007**, *339*, 44-56.

189. Napoli F., Chiesa M., Giamello E., Fittipaldi M., Di Valentin C., Gallino F. and Pacchioni G., N_2^- Radical Anions Trapped in Bulk Polycrystalline MgO. *J. Phys. Chem. C* **2010**, *114*, 5187-5192.

190. Polliotto V., Albanese E., Livraghi S., Pacchioni G. and Giamello E., The Photoactive Nitrogen Impurity in Nitrogen-doped Zirconium Titanate (N-$ZrTiO_4$): A Combined Electron Paramagnetic Resonance and Density Functional Theory Study. *J. Mater. Chem. A* **2017**, *5*, 13062–13071.

191. Coronado J. M., Javier Maira A., Martínez-Arias A., Conesa J. C. and Soria J., EPR Study of the Radicals Formed upon UV Irradiation of Ceria-based Photocatalysts. *J. Photochem. Photobiol., A* **2002**, *150*, 213-221.

192. Soria J., Martinez-Arias A. and Conesa J. C., Spectroscopic Study of Oxygen Adsorption as a Method to Study Surface Defects on CeO_2. *J. Chem. Soc., Faraday Trans.* **1995**, *91*, 1669-1678.

193. Langhammer C., Yuan Z., Zoric I. and Kasemo B., Plasmonic Properties of Supported Pt and Pd Nanostructures. *Nano Lett.* **2006**, *6*, 833-838.

194. Li G., Dimitrijevic N. M., Chen L., Rajh T. and Gray K. A., Role of Surface/Interfacial Cu^{2+} Sites in the Photocatalytic Activity of Coupled CuO–TiO_2 Nanocomposites. *J. Phys. Chem. C* **2008**, *112*, 19040-19044.

195. Huang Q., Kang F., Liu H., Li Q. and Xiao X. D., Highly Aligned $Cu_2O/CuO/TiO_2$ Core/Shell Nanowire Arrays as Photocathodes for Water Photoelectrolysis. *J. Mater. Chem. A* **2013**, *1*, 2418-2425.

196. Banerjee S. and Chakravorty D., Optical Absorption by Nanoparticles of Cu_2O. *Europhys. Lett.* **2000**, *52*, 468-473.

197. Nosaka Y., Takahashi S., Sakamoto H. and Nosaka A. Y., Reaction Mechanism of Cu(II)-Grafted Visible-Light Responsive TiO_2 and WO_3 Photocatalysts Studied by Means of ESR Spectroscopy and Chemiluminescence Photometry. *J. Phys. Chem. C* **2011**, *115*, 21283-21290.

198. Córdoba G., Viniegra M., Fierro J. L. G., Padilla J. and Arroyo R., TPR, ESR, and XPS Study of Cu^{2+} Ions in Sol–Gel-Derived TiO_2. *J. Solid State Chem.* **1998**, *138*, 1-6.

199. Chen T., Feng Z. H., Wu G. P., Shi J. Y., Ma G. J., Ying P. L. and Li C., Mechanistic Studies of Photocatalytic Reaction of Methanol for Hydrogen Production on Pt/TiO_2 by in Situ Fourier Transform IR and Time-resolved IR Spectroscopy. *J. Phys. Chem. C* **2007**, *111*, 8005-8014.

200. Chiarello G. L., Aguirre M. H. and Selli E., Hydrogen Production by Photocatalytic Steam Reforming of Methanol on Noble Metal-modified TiO_2. *J. Catal.* **2010**, *273*, 182-190.

201. Priebe J. B., Radnik J., Kreyenschulte C., Lennox A. J., Junge H., Beller M. and Brückner A., H_2 Generation with (Mixed) Plasmonic $Cu/Au-TiO_2$ Photocatalysts: Structure–Reactivity Relationships Assessed by in situ Spectroscopy. *ChemCatChem* **2017**, *9*, 1025-1031.

202. Biedrzycki J., Livraghi S., Giamello E., Agnoli S. and Granozzi G., Fluorine- and Niobium-Doped TiO_2: Chemical and Spectroscopic Properties of Polycrystalline n-Type-Doped Anatase. *J. Phys. Chem. C* **2014**, *118*, 8462-8473.

203. Parveen F., Sannakki B., Mandke M. V. and Pathan H. M., Copper Nanoparticles: Synthesis Methods and Its Light Harvesting Performance. *Sol. Energy Mater. Sol. Cells* **2016**, *144*, 371-382.

204. Singh M., Sinha I., Premkumar M., Singh A. K. and Mandal R. K., Structural and Surface Plasmon Behavior of Cu Nanoparticles Using Different Stabilizers. *Colloids Surf., A* **2010**, *359*, 88-94.

205. Soroka I. L., Shchukarev A., Jonsson M., Tarakina N. V. and Korzhavyi P. A., Cuprous Hydroxide in a Solid Form: Does It Exist? *Dalton Transactions* **2013**, *42*, 9585-9594.

206. Graetzel M. and Frank A. J., Interfacial Electron-Transfer Reactions in Colloidal Semiconductor Dispersions. Kinetic Analysis. *J. Phys. Chem.* **1982**, *86*, 2964-2967.

207. Yang R. Q., Yu X. C., Zhang Y., Li W. Z. and Tsubaki N., A New Method of Low-Temperature Methanol Synthesis on Cu/ZnO/Al_2O_3 catalysts from CO/CO_2/H_2. *Fuel* **2008**, *87*, 443-450.

208. Meng F. Z., Zhang Q. D., Yang G. H., Yang R. Q., Yoneyama Y. and Tsubaki N., Structural and Kinetical Studies on the Supercritical CO_2 dried Cu/ZnO Catalyst for Low-Temperature Methanol Synthesis. *Chem. Eng. J.* **2016**, *295*, 160-166.

209. Livraghi S., Votta A., Paganini M. C. and Giamello E., The Nature of Paramagnetic Species in Nitrogen Doped TiO_2 Active in Visible Light Photocatalysis. *Chem. Commun.* **2005**, 498-500.

210. Liu G., Yang H. G., Wang X., Cheng L., Lu H., Wang L., Lu G. Q. and Cheng H.-M., Enhanced Photoactivity of Oxygen-Deficient Anatase TiO_2 Sheets with Dominant {001} Facets. *J. Phys. Chem. C* **2009**, *113*, 21784-21788.

211. Liu X., Gao S., Xu H., Lou Z., Wang W., Huang B. and Dai Y., Green Synthetic Approach for Ti^{3+} Self-Doped TiO_{2-x} Nanoparticles with Efficient Visible Light Photocatalytic Activity. *Nanoscale* **2013**, *5*, 1870-1875.

212. Liu L. and Chen X., Titanium Dioxide Nanomaterials: Self-Structural Modifications. *Chem. Rev.* **2014**, *114*, 9890-9918.

213. Zhang H., Zhao Y., Chen S., Yu B., Xu J., Xu H., Hao L. and Liu Z., Ti^{3+} Self-Doped TiO_x@Anatase Core-Shell Structure with Enhanced Visible Light Photocatalytic Activity. *J. Mater. Chem. A* **2013**, *1*, 6138-6144.

214. Su J., Zou X. and Chen J.-S., Self-Modification of Titanium Dioxide Materials by Ti^{3+} and/or Oxygen Vacancies: New Insights into Defect Chemistry of Metal Oxides. *RSC Adv.* **2014**, *4*, 13979-13988.

215. Zuo F., Wang L., Wu T., Zhang Z., Borchardt D. and Feng P., Self-Doped Ti^{3+} Enhanced Photocatalyst for Hydrogen Production under Visible Light. *J. Am. Chem. Soc.* **2010**, *132*, 11856-11857.

216. Khomenko V. M., Langer K., Rager H. and Fett A., Electronic Absorption by Ti^{3+} Ions and Electron Delocalization in Synthetic Blue Rutile. *Phys. Chem. Miner.* **1998**, *25*, 338-346.

217. Hagen W. R., Wassink H., Eady R. R., Smith B. E. and Haaker H., Quantitative EPR of an S= 7/2 System in Thionine-Oxidized Mofe Proteins of Nitrogenase. A Redefinition of the p-cluster Concept. *Eur. J. Biochem.* **1987**, *169*, 457-465.

218. Katafias A. and Fenska J., Sulfuric Acid Controlled Oxidative Degradation of Azure B and Thionine Dyes by Cerium(IV). *Int. J. Chem. Kinet.* **2011**, *43*, 523-536.

219. Albracht S. P. J., Roseboom W. and Hatchikian E. C., The Active Site of the [FeFe]-Hydrogenase from *Desulfovibrio Desulfuricans*. 1. Light Sensitivity and Magnetic Hyperfine Interactions as Observed by Electron Paramagnetic Resonance. *J. Biol. Inorg. Chem.* **2006**, *11*, 88-101.

220. Kowal A. T., Adams M. W. W. and Johnson M. K., Electron-Paramagnetic Resonance studies of the low-temperature photolytic behavior

of oxidized hydrogenase I from *clostridium-pasteurianum*. *J. Biol. Chem.* **1989**, *264*, 4342-4348.

221. Morra S., Maurelli S., Chiesa M., Mulder D. W., Ratzloff M. W., Giamello E., King P. W., Gilardi G. and Valetti F., The Effect of a C298D Mutation in CaHydA [FeFe]-hydrogenase: Insights into the Protein-Metal Cluster Interaction by EPR and FTIR Spectroscopic Investigation. *Biochim. Biophys. Acta* **2016**, *1857*, 98-106.

222. Mitou G., Higgins C., Wittung-Stafshede P., Conover R. C., Smith A. D., Johnson M. K., Gaillard J., Stubna A., Munck E. and Meyer J., An Isc-Type Extremely Thermostable [2Fe-2S] Ferredoxin from Aquifex Aeolicus. Biochemical, Spectroscopic, and Unfolding Studies. *Biochemistry* **2003**, *42*, 1354-1364.

Appendix

Appendix A: Didactic Activities.

Presentations

- Flash presentation: "Titanium oxide modification for photocatalytic applications: the TiO_2-[Fe-Fe] Hydrogenase hybrid system." – National school "New Materials and Sustainable Energies" – Bressanone (Italy), 14 July 2015.
- Poster: "Protein-support interaction, electron transfer and hydrogen evolution in [FeFe]-hydrogenase-TiO_2 hybrid systems prepared using modified-TiO_2." – EFEPR conference" – Turin (Italy), 4-8 September 2016
- Oral presentation: "*Find a sponsor.*" – Winter school – Bardonecchia (Italy) , 2 February 2016

PhD schools attended

- Summer School "New Materials and Sustainable Energies", Bressanone (Italy), 10-14 July 2015
- Winter school "Molecule@surface", Bardonecchia (To), 31 January -5 February 2016.

Classes, seminars, conferences attended

Graduate school courses

- "Solid state NMR: basics and applications", Università di Torino, April-May 2015.
- "English writing and communication skills", Università di Torino, 16 March-18 April 2015.
- "CRISDI School: Introduction to crystallography", Università di Torino, 25-27 May 2015.

- "CRISDI School: Diffractometric crystallography", Università di Torino, 28-29 May 2015.
- "CRISDI School: Instrumentation used for X-Ray diffraction", Università di Torino, 28-29 May 2015.
- "CRISDI School: X-Ray diffraction methods: polycrystalline", Università di Torino, 9-12 June 2015.
- "CRISDI School: Use TEM-EDS for characterization of inorganic phases", Università di Torino, 15-18 June 2015.
- "CRISDI School: Spectroscopic and combined techniques for structural determination", Università di Torino, 26-29 June 2015.
- "Experimental techniques for gas-solid adsorption studies: comparison between microgravimetric and microcalorimetric techniques", Università di Torino, 19-23 October 2015.
- "Advanced microscopy-techniques for the characterization of materials". Università di Torino, 10-11 December 2015.
- "The Evolution of Heterogeneous, Homogeneous and Enzymatic Catalysis. Key Processes and Scientists." Prof Adriano Zecchina. Università di Torino, 25-28 February 2016.

Seminars

- "Luminescent Ru(II) complexes in liposomes and nano discs: impact of environment on photophysical properties." (Prof. Rosenberg), Torino, 11 November 2014.
- "Metallic Glasses-recent results on formation and properties in general context of glassy systems." (Prof. A. L. Greer), Torino, 25 November 2014.
- "Fundamental interactions at the mineral/liquid interface: a key to address environmental, energetic and medical challenges." (Prof. Raffaella Demichelis), Torino, 16 December 2014.

- “Porous scaffolds for tissue engineering: from polymers to graphene.” (Prof. Marta Cerruti), Torino, 26 February 2015.
- “Catalysis” (Prof. Zecchina), Torino, 16 April 2015.
- “Light and nanomaterials: see, understand and care.” (Prof. Luisa De Cola), Torino, 29 September 2015.

Conference and workshop

- Conference “FIRB Meeting”, Torino, 12-13 February 2015.
- Conference + workshop “Hybrid and Organic Photovoltaics International Conference (HOPV)”, Roma, 10-14 May 2015.
- Workshop “Measure of Z-potential of solid surface.” (Prof. Marta Cerruti), Torino, 14 September 2015.
- Workshop “EPR in catalysis: from model to real system.” Torino, 26-27 November 2015.
- Conference “Italian-French days”, Avignon, 25-26 April 2016.
- Workshop “International workshop on N_2O abatement”, Cracow, 4-6 May 2016.
- Conference “EFERP European Federation of EPR groups 2016”, Torino, 4-8 September 2016.
- NIS Colloquium "Keywords: environment, water, sustainable materials, circular economy. Towards 2018-20 European proposals", Torino 20-21th April 2017.
- National Congress “Società Chimica Italiana XXVI”, Paestum 10-14th September 2017.

Didactic activities:

- Assistance to the laboratory of " Introduction to Inorganic Chemistry". Dott. Stefano Livraghi, Torino, January 2015, 2016, 2017.

Appendix B: Periods Abroad.

- 1 May- 2 June 2016
  TEM investigation of $ZrTiO_4$ based oxides. – Cracow (Poland), Jagellonian University, Chemistry department. Supervisor: Prof. Zbigniew Sojka.
- 1 October- 23 October 2016
  Photocatalytic tests (SFERA project). Title of the project: ”Innovative Oxide materials for the Solar Photocatalytic Degradation. – Almeria (Spain), Plataforma Solar. Supervisor: Prof. Sixto Malato.
- 6 May – 10 June 2017
  Photocatalytic tests of hydrogen evolution. – Gdansk (Poland), Department of Environmental Technology, Faculty of Chemistry, University of Gdansk. Supervisor: Prof. Adriana Zaleska-Medynska

Appendix C: Publications.

1. V. Polliotto, E. Albanese, S. Livraghi, G. Pacchioni, Elio Giamello, "The photoactive nitrogen impurity in nitrogen-doped zirconium titanate (N-$ZrTiO_4$): a combined electron paramagnetic resonance and density functional theory study", *Journal of Materials Chemistry A*, **2017**, 5, 13062–13071.

2. V. Polliotto, E. Albanese, S. Livraghi, P. Indyka, Z. Sojka, G. Pacchioni, E. Giamello, "Fifty−Fifty Zr−Ti Solid Solution with a TiO_2-Type Structure: Electronic Structure and Photochemical Properties of Zirconium Titanate $ZrTiO_4$", *Journal of Physical Chemistry C*, **2017**, 121, 5487−5497.

3. V. Polliotto, S. Morra, S. Livraghi, F. Valetti, G. Gilardi, E. Giamello, "Electron transfer and H_2 evolution in hybrid systems based on [FeFe]-hydrogenase anchored on modified TiO_2.", *International Journal of Hydrogen Energy*, **2016**, 41, 10547 -10556**.**

4. E. G. Panarelli, S. Livraghi, S. Maurelli, V. Polliotto, M. Chiesa, E. Giamello, "Role of surface water molecules in stabilizing trapped hole centres in titanium dioxide (anatase) as monitored by electron paramagnetic resonance.", *Journal of Photochemistry and Photobiology A: Chemistry,* **2016**, 322–323, 27–34.

5. M.C. Paganini, D. Dalmasso, C. Gionco, V. Polliotto, L. Mantilleri, P. Calza "Beyond TiO_2: cerium doped zinc oxide as new photocatalyst for the photodegradation of persistent pollutants." *Chemistry Select*, **2016**, 1, 3377–3383.

6. V. Polliotto, S. Livraghi, Adriana Zaleska-Mendynska, Elio Giamello, "Cu oxidation states and charge carriers separation mechanism during photocatalytic hydrogen evolution on copper modified TiO_2 and $ZrTiO_4$", in preparation.

7. V. Polliotto, S. Livraghi, E. Albanese, G. Pacchioni, E. Giamello, "Oxygen adsorption properties of Cerium doped-$ZrTiO_4$", in preparation.

- <u>V. Polliotto</u>, E. Albanese, S. Livraghi, G. Pacchioni, Elio Giamello, "The photoactive nitrogen impurity in nitrogen-doped zirconium titanate (N-$ZrTiO_4$): a combined electron paramagnetic resonance and density functional theory study", *Journal of Materials Chemistry A*, **2017**, 5, 13062–13071.

Journal of
Materials Chemistry A

PAPER

View Article Online
View Journal | View Issue

Check for updates

Cite this: *J. Mater. Chem. A*, 2017, **5**, 13062

The photoactive nitrogen impurity in nitrogen-doped zirconium titanate (N-$ZrTiO_4$): a combined electron paramagnetic resonance and density functional theory study†

Valeria Polliotto,[a] Elisa Albanese,[b] Stefano Livraghi,*[a] Gianfranco Pacchioni[b] and Elio Giamello[a]

Received 7th April 2017
Accepted 28th May 2017

DOI: 10.1039/c7ta03047a

rsc.li/materials-a

Nitrogen doping represents an important strategy to modulate the optical, magnetic and photochemical properties of oxides for applications spanning from photocatalysis to optoelectronics and spintronics. In this work for the first time zirconium titanate, a material that exhibits many attractive properties, including an excellent dielectric constant, high corrosion resistance, high permittivity at microwave frequencies and excellent temperature stability, has been doped with nitrogen *via* a wet chemistry method. A detailed description of the geometrical and the electronic structure of the dopant centre has been obtained coupling Electron Paramagnetic Resonance (EPR) spectroscopy and density functional theory (DFT) calculations. Insertion of nitrogen impurities into the $ZrTiO_4$ lattice modifies the optical properties causing an appreciable absorption in the visible range. The joint analysis of the EPR evidence and the DFT elaboration indicates that the nitrogen impurities preferentially occupy an interstitial position of the lattice generating intra-band gap states about 1 eV above the valence band edge that are responsible for the visible light absorption. The majority of the intra-band gap states are diamagnetic (N^-) while a minor fraction is paramagnetic ($N^{\bullet}$). These centres are photosensitive in that the ratio between N^- and $N^{\bullet}$ is modified, upon irradiation, because of electron excitation from the intra-band gap states to the conduction band.

1. Introduction

The incorporation of nitrogen impurities into oxides is becoming an important topic in several contexts of materials chemistry research spanning from photocatalysis[1] to optoelectronics[2] and spintronics.[3] The insertion of nitrogen in the oxide lattice, in fact, represents a strategy to modulate the optical, magnetic and photochemical properties of the material.

As to the field of photocatalysis, a lot of effort has been devoted, in the recent past, to dope, with this chemical element, titanium dioxide and several other oxides. In all these cases, the aim of doping was to extend the photoactivity of these materials, which usually are activated by the UV component of light, to the visible wavelength range. In most metal oxides the N impurities, introduced into the solid, usually form intra-band gap states, just above the valence band, from which the electron excitation in the conduction band can be promoted also by visible light.[1,4,5] In spite of the huge number of papers concerning this important research field, some fundamental aspects such as the chemical nature of the dopant centres are still debated.

Incorporation of N atoms into an oxide lattice has also been proposed to be an effective way, with respect to conventional cation substitution, to achieve p-type doping in oxide materials, which is fundamental for optoelectronic applications. In semiconducting oxides the N substitution for O in principle creates an electron deficient state with respect to the lattice O^{2-} introducing one hole per N situated just above the valence band chemical potential.[6]

Doping of nitrogen into tantalum pentoxide (Ta_2O_5), for instance, has been recently reported to have a dual effect. The former is the visible light sensitization of this material for photoelectrochemical hydrogen production by water splitting and the second is a change in electronic structure that turns the material from n-type to p-type.[7]

The possibility of modifying the electronic structure of an oxide and, in particular, of obtaining p-type oxides moving from n-type materials however still presents a highly questionable topic.[8,9] Some of us, for instance, have recently shown that in the case on SnO_2, for which the possibility to obtain a stable p-type SnO_2 would have a huge impact on the fabrication of various kinds of optoelectronic devices, the doped material is still rich

---

[a] *Dipartimento di Chimica, NIS, Università di Torino, Via P. Giuria 7, 10125 Torino, Italy. E-mail: stefano.livraghi@unito.it*

[b] *Dipartimento di Scienza dei Materiali, Università Milano Bicocca, via R. Cozzi 55, 20125 Milano, Italy*

† Electronic supplementary information (ESI) available. See DOI: 10.1039/c7ta03047a

- V. Polliotto, E. Albanese, S. Livraghi, P. Indyka, Z. Sojka, G. Pacchioni, E. Giamello, “Fifty–Fifty Zr–Ti Solid Solution with a TiO_2-Type Structure: Electronic Structure and Photochemical Properties of Zirconium Titanate $ZrTiO_4$”, *Journal of Physical Chemistry C*, **2017**, 121, 5487–5497.

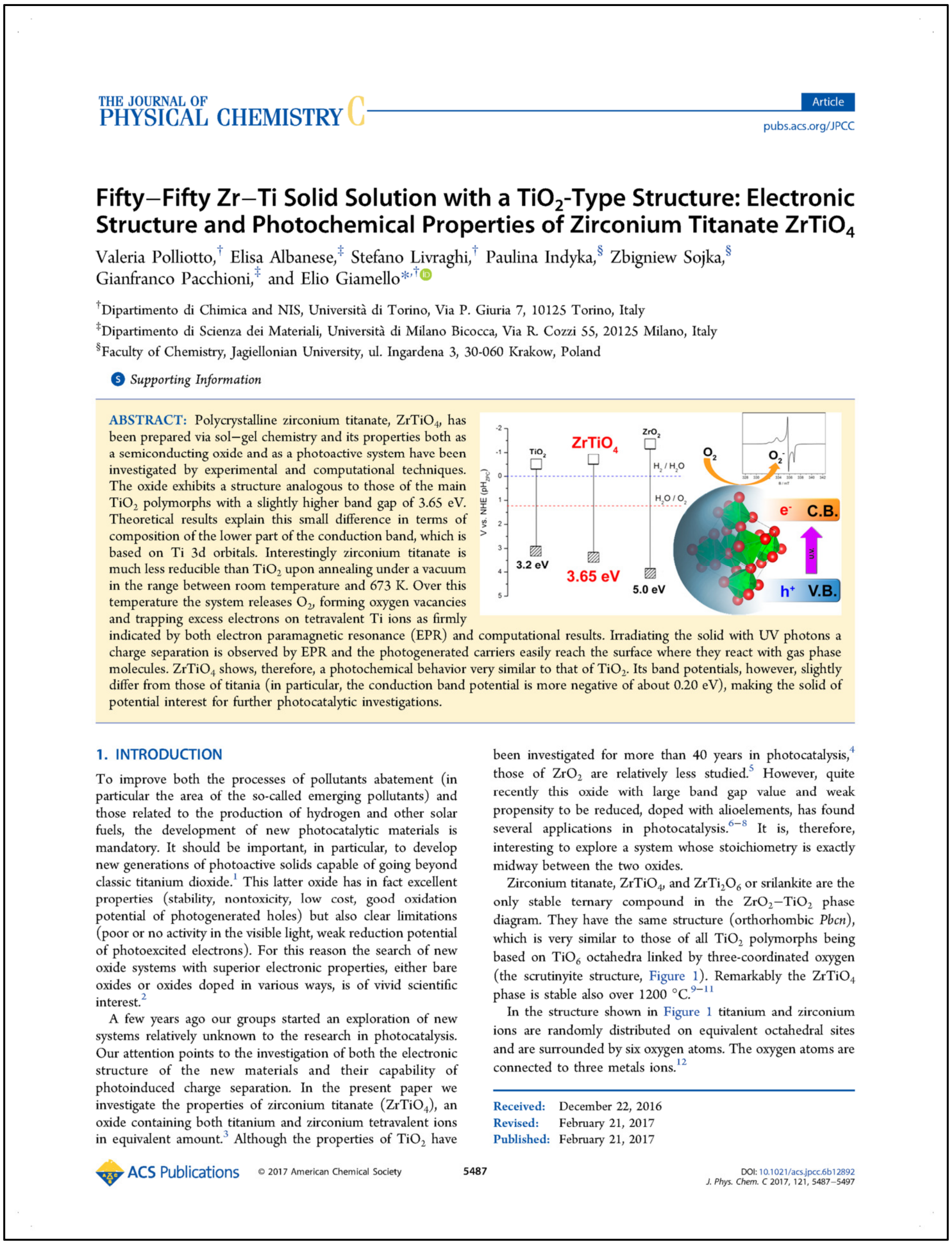

THE JOURNAL OF PHYSICAL CHEMISTRY C
Article
pubs.acs.org/JPCC

Fifty–Fifty Zr–Ti Solid Solution with a TiO_2-Type Structure: Electronic Structure and Photochemical Properties of Zirconium Titanate $ZrTiO_4$

Valeria Polliotto,[†] Elisa Albanese,[‡] Stefano Livraghi,[†] Paulina Indyka,[§] Zbigniew Sojka,[§] Gianfranco Pacchioni,[‡] and Elio Giamello*[,†]

[†]Dipartimento di Chimica and NIS, Università di Torino, Via P. Giuria 7, 10125 Torino, Italy
[‡]Dipartimento di Scienza dei Materiali, Università di Milano Bicocca, Via R. Cozzi 55, 20125 Milano, Italy
[§]Faculty of Chemistry, Jagiellonian University, ul. Ingardena 3, 30-060 Krakow, Poland

Supporting Information

ABSTRACT: Polycrystalline zirconium titanate, $ZrTiO_4$, has been prepared via sol–gel chemistry and its properties both as a semiconducting oxide and as a photoactive system have been investigated by experimental and computational techniques. The oxide exhibits a structure analogous to those of the main TiO_2 polymorphs with a slightly higher band gap of 3.65 eV. Theoretical results explain this small difference in terms of composition of the lower part of the conduction band, which is based on Ti 3d orbitals. Interestingly zirconium titanate is much less reducible than TiO_2 upon annealing under a vacuum in the range between room temperature and 673 K. Over this temperature the system releases O_2, forming oxygen vacancies and trapping excess electrons on tetravalent Ti ions as firmly indicated by both electron paramagnetic resonance (EPR) and computational results. Irradiating the solid with UV photons a charge separation is observed by EPR and the photogenerated carriers easily reach the surface where they react with gas phase molecules. $ZrTiO_4$ shows, therefore, a photochemical behavior very similar to that of TiO_2. Its band potentials, however, slightly differ from those of titania (in particular, the conduction band potential is more negative of about 0.20 eV), making the solid of potential interest for further photocatalytic investigations.

1. INTRODUCTION

To improve both the processes of pollutants abatement (in particular the area of the so-called emerging pollutants) and those related to the production of hydrogen and other solar fuels, the development of new photocatalytic materials is mandatory. It should be important, in particular, to develop new generations of photoactive solids capable of going beyond classic titanium dioxide.[1] This latter oxide has in fact excellent properties (stability, nontoxicity, low cost, good oxidation potential of photogenerated holes) but also clear limitations (poor or no activity in the visible light, weak reduction potential of photoexcited electrons). For this reason the search of new oxide systems with superior electronic properties, either bare oxides or oxides doped in various ways, is of vivid scientific interest.[2]

A few years ago our groups started an exploration of new systems relatively unknown to the research in photocatalysis. Our attention points to the investigation of both the electronic structure of the new materials and their capability of photoinduced charge separation. In the present paper we investigate the properties of zirconium titanate ($ZrTiO_4$), an oxide containing both titanium and zirconium tetravalent ions in equivalent amount.[3] Although the properties of TiO_2 have been investigated for more than 40 years in photocatalysis,[4] those of ZrO_2 are relatively less studied.[5] However, quite recently this oxide with large band gap value and weak propensity to be reduced, doped with alioelements, has found several applications in photocatalysis.[6−8] It is, therefore, interesting to explore a system whose stoichiometry is exactly midway between the two oxides.

Zirconium titanate, $ZrTiO_4$, and $ZrTi_2O_6$ or srilankite are the only stable ternary compound in the ZrO_2–TiO_2 phase diagram. They have the same structure (orthorhombic *Pbcn*), which is very similar to those of all TiO_2 polymorphs being based on TiO_6 octahedra linked by three-coordinated oxygen (the scrutinyite structure, Figure 1). Remarkably the $ZrTiO_4$ phase is stable also over 1200 °C.[9−11]

In the structure shown in Figure 1 titanium and zirconium ions are randomly distributed on equivalent octahedral sites and are surrounded by six oxygen atoms. The oxygen atoms are connected to three metals ions.[12]

Received: December 22, 2016
Revised: February 21, 2017
Published: February 21, 2017

DOI: 10.1021/acs.jpcc.6b12892
J. Phys. Chem. C 2017, 121, 5487−5497

- V. Polliotto, S. Morra, S. Livraghi, F. Valetti, G. Gilardi, E. Giamello, "Electron transfer and H_2 evolution in hybrid systems based on [FeFe]-hydrogenase anchored on modified TiO_2.", *International Journal of Hydrogen Energy*, **2016**, 41, 10547 -10556**.**

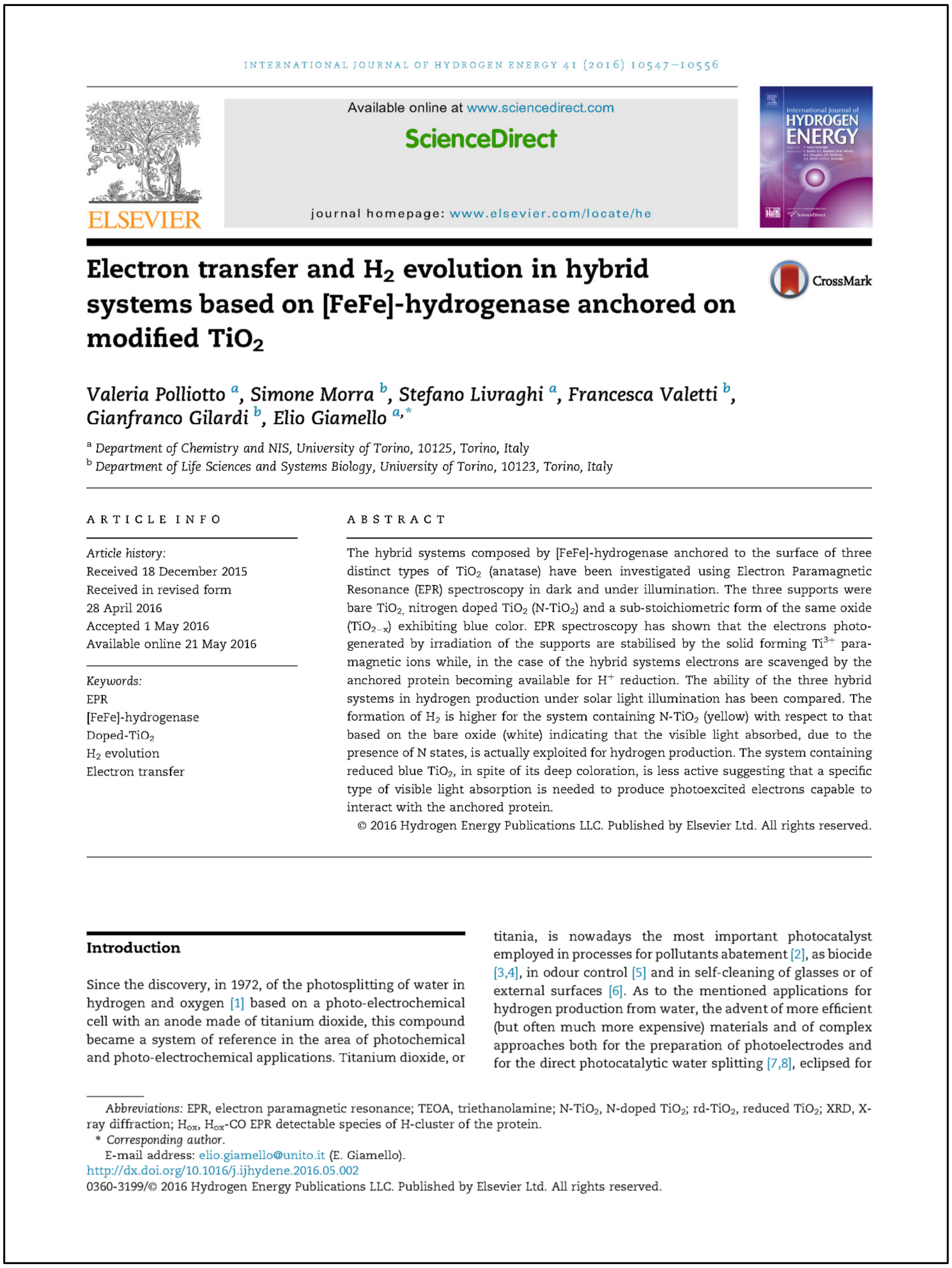

INTERNATIONAL JOURNAL OF HYDROGEN ENERGY 41 (2016) 10547–10556

Electron transfer and H_2 evolution in hybrid systems based on [FeFe]-hydrogenase anchored on modified TiO_2

Valeria Polliotto [a], *Simone Morra* [b], *Stefano Livraghi* [a], *Francesca Valetti* [b], *Gianfranco Gilardi* [b], *Elio Giamello* [a,*]

[a] *Department of Chemistry and NIS, University of Torino, 10125, Torino, Italy*
[b] *Department of Life Sciences and Systems Biology, University of Torino, 10123, Torino, Italy*

ARTICLE INFO

Article history:
Received 18 December 2015
Received in revised form
28 April 2016
Accepted 1 May 2016
Available online 21 May 2016

Keywords:
EPR
[FeFe]-hydrogenase
Doped-TiO_2
H_2 evolution
Electron transfer

ABSTRACT

The hybrid systems composed by [FeFe]-hydrogenase anchored to the surface of three distinct types of TiO_2 (anatase) have been investigated using Electron Paramagnetic Resonance (EPR) spectroscopy in dark and under illumination. The three supports were bare TiO_2, nitrogen doped TiO_2 (N-TiO_2) and a sub-stoichiometric form of the same oxide (TiO_{2-x}) exhibiting blue color. EPR spectroscopy has shown that the electrons photo-generated by irradiation of the supports are stabilised by the solid forming Ti^{3+} paramagnetic ions while, in the case of the hybrid systems electrons are scavenged by the anchored protein becoming available for H^+ reduction. The ability of the three hybrid systems in hydrogen production under solar light illumination has been compared. The formation of H_2 is higher for the system containing N-TiO_2 (yellow) with respect to that based on the bare oxide (white) indicating that the visible light absorbed, due to the presence of N states, is actually exploited for hydrogen production. The system containing reduced blue TiO_2, in spite of its deep coloration, is less active suggesting that a specific type of visible light absorption is needed to produce photoexcited electrons capable to interact with the anchored protein.

Introduction

Since the discovery, in 1972, of the photosplitting of water in hydrogen and oxygen [1] based on a photo-electrochemical cell with an anode made of titanium dioxide, this compound became a system of reference in the area of photochemical and photo-electrochemical applications. Titanium dioxide, or titania, is nowadays the most important photocatalyst employed in processes for pollutants abatement [2], as biocide [3,4], in odour control [5] and in self-cleaning of glasses or of external surfaces [6]. As to the mentioned applications for hydrogen production from water, the advent of more efficient (but often much more expensive) materials and of complex approaches both for the preparation of photoelectrodes and for the direct photocatalytic water splitting [7,8], eclipsed for

---

Abbreviations: EPR, electron paramagnetic resonance; TEOA, triethanolamine; N-TiO_2, N-doped TiO_2; rd-TiO_2, reduced TiO_2; XRD, X-ray diffraction; H_{ox}, H_{ox}-CO EPR detectable species of H-cluster of the protein.

[*] *Corresponding author.*
E-mail address: elio.giamello@unito.it (E. Giamello).

http://dx.doi.org/10.1016/j.ijhydene.2016.05.002

- E. G. Panarelli, S. Livraghi, S. Maurelli, V. Polliotto, M. Chiesa, E. Giamello, "Role of surface water molecules in stabilizing trapped hole centres in titanium dioxide (anatase) as monitored by electron paramagnetic resonance.", *Journal of Photochemistry and Photobiology A: Chemistry,* **2016**, 322–323, 27–34.

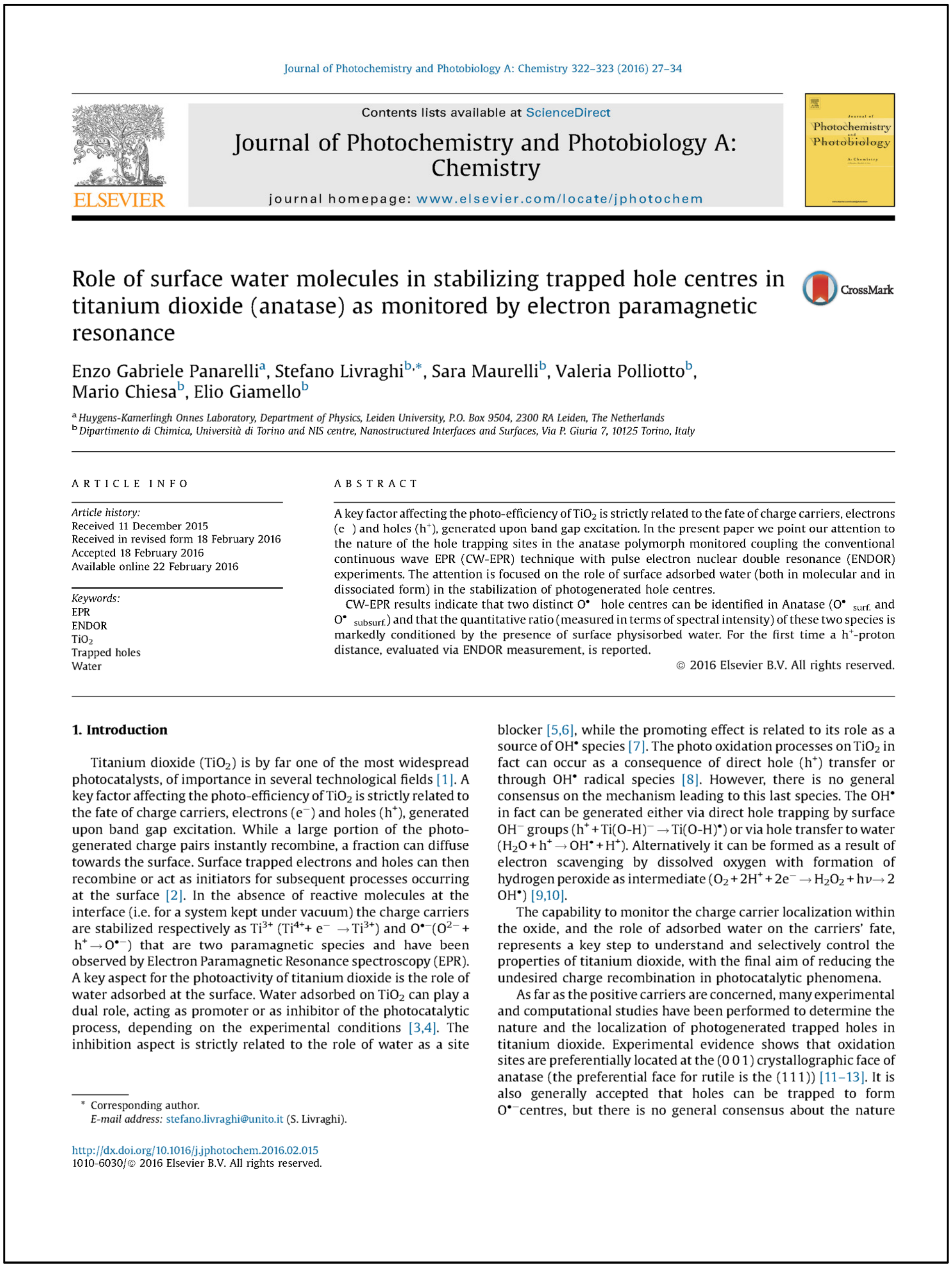

Journal of Photochemistry and Photobiology A: Chemistry 322–323 (2016) 27–34

Contents lists available at ScienceDirect

Journal of Photochemistry and Photobiology A: Chemistry

journal homepage: www.elsevier.com/locate/jphotochem

Role of surface water molecules in stabilizing trapped hole centres in titanium dioxide (anatase) as monitored by electron paramagnetic resonance

Enzo Gabriele Panarelli[a], Stefano Livraghi[b,*], Sara Maurelli[b], Valeria Polliotto[b], Mario Chiesa[b], Elio Giamello[b]

[a] *Huygens-Kamerlingh Onnes Laboratory, Department of Physics, Leiden University, P.O. Box 9504, 2300 RA Leiden, The Netherlands*
[b] *Dipartimento di Chimica, Università di Torino and NIS centre, Nanostructured Interfaces and Surfaces, Via P. Giuria 7, 10125 Torino, Italy*

ARTICLE INFO

Article history:
Received 11 December 2015
Received in revised form 18 February 2016
Accepted 18 February 2016
Available online 22 February 2016

Keywords:
EPR
ENDOR
TiO_2
Trapped holes
Water

ABSTRACT

A key factor affecting the photo-efficiency of TiO_2 is strictly related to the fate of charge carriers, electrons (e) and holes (h^+), generated upon band gap excitation. In the present paper we point our attention to the nature of the hole trapping sites in the anatase polymorph monitored coupling the conventional continuous wave EPR (CW-EPR) technique with pulse electron nuclear double resonance (ENDOR) experiments. The attention is focused on the role of surface adsorbed water (both in molecular and in dissociated form) in the stabilization of photogenerated hole centres.

CW-EPR results indicate that two distinct $O^{\bullet}$ hole centres can be identified in Anatase ($O^{\bullet}{}_{surf.}$ and $O^{\bullet}{}_{subsurf.}$) and that the quantitative ratio (measured in terms of spectral intensity) of these two species is markedly conditioned by the presence of surface physisorbed water. For the first time a h^+-proton distance, evaluated via ENDOR measurement, is reported.

1. Introduction

Titanium dioxide (TiO_2) is by far one of the most widespread photocatalysts, of importance in several technological fields [1]. A key factor affecting the photo-efficiency of TiO_2 is strictly related to the fate of charge carriers, electrons (e^-) and holes (h^+), generated upon band gap excitation. While a large portion of the photogenerated charge pairs instantly recombine, a fraction can diffuse towards the surface. Surface trapped electrons and holes can then recombine or act as initiators for subsequent processes occurring at the surface [2]. In the absence of reactive molecules at the interface (i.e. for a system kept under vacuum) the charge carriers are stabilized respectively as Ti^{3+} ($Ti^{4+} + e^- \rightarrow Ti^{3+}$) and $O^{\bullet -}$ ($O^{2-} + h^+ \rightarrow O^{\bullet -}$) that are two paramagnetic species and have been observed by Electron Paramagnetic Resonance spectroscopy (EPR). A key aspect for the photoactivity of titanium dioxide is the role of water adsorbed at the surface. Water adsorbed on TiO_2 can play a dual role, acting as promoter or as inhibitor of the photocatalytic process, depending on the experimental conditions [3,4]. The inhibition aspect is strictly related to the role of water as a site blocker [5,6], while the promoting effect is related to its role as a source of $OH^{\bullet}$ species [7]. The photo oxidation processes on TiO_2 in fact can occur as a consequence of direct hole (h^+) transfer or through $OH^{\bullet}$ radical species [8]. However, there is no general consensus on the mechanism leading to this last species. The $OH^{\bullet}$ in fact can be generated either via direct hole trapping by surface OH^- groups ($h^+ + Ti(O\text{-}H)^- \rightarrow Ti(O\text{-}H)^{\bullet}$) or via hole transfer to water ($H_2O + h^+ \rightarrow OH^{\bullet} + H^+$). Alternatively it can be formed as a result of electron scavenging by dissolved oxygen with formation of hydrogen peroxide as intermediate ($O_2 + 2H^+ + 2e^- \rightarrow H_2O_2 + h\nu \rightarrow 2\ OH^{\bullet}$) [9,10].

The capability to monitor the charge carrier localization within the oxide, and the role of adsorbed water on the carriers' fate, represents a key step to understand and selectively control the properties of titanium dioxide, with the final aim of reducing the undesired charge recombination in photocatalytic phenomena.

As far as the positive carriers are concerned, many experimental and computational studies have been performed to determine the nature and the localization of photogenerated trapped holes in titanium dioxide. Experimental evidence shows that oxidation sites are preferentially located at the (0 0 1) crystallographic face of anatase (the preferential face for rutile is the (1 1 1)) [11–13]. It is also generally accepted that holes can be trapped to form $O^{\bullet -}$centres, but there is no general consensus about the nature

---

[*] Corresponding author.
E-mail address: stefano.livraghi@unito.it (S. Livraghi).

http://dx.doi.org/10.1016/j.jphotochem.2016.02.015

- M.C. Paganini, D. Dalmasso, C. Gionco, V. Polliotto, L. Mantilleri, P. Calza "Beyond TiO_2: cerium doped zinc oxide as new photocatalyst for the photodegradation of persistent pollutants." *Chemistry Select*, **2016**, 1, 3377–3383.

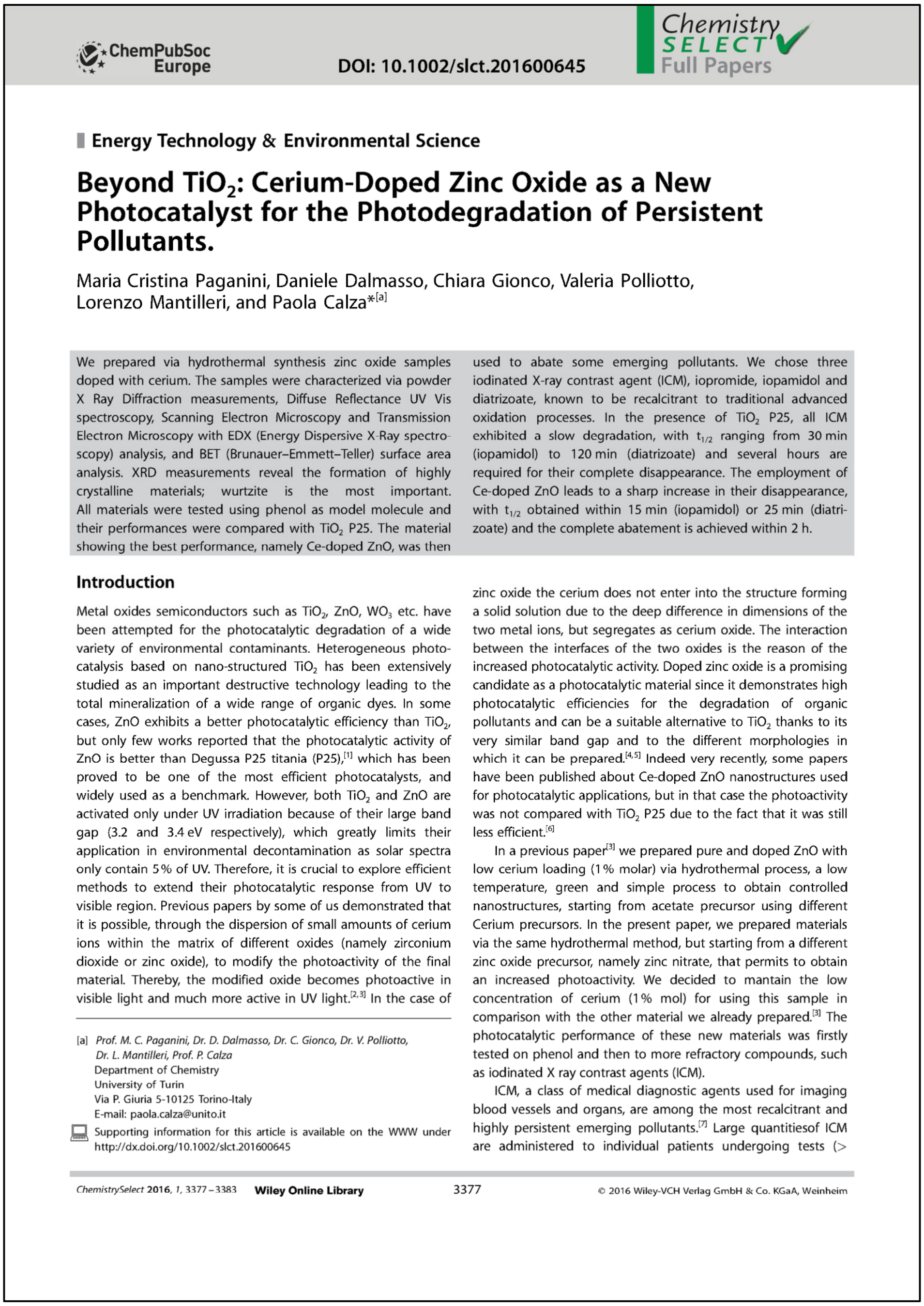

ChemPubSoc Europe
DOI: 10.1002/slct.201600645
Chemistry SELECT Full Papers

Energy Technology & Environmental Science

Beyond TiO_2: Cerium-Doped Zinc Oxide as a New Photocatalyst for the Photodegradation of Persistent Pollutants.

Maria Cristina Paganini, Daniele Dalmasso, Chiara Gionco, Valeria Polliotto, Lorenzo Mantilleri, and Paola Calza*[a]

We prepared via hydrothermal synthesis zinc oxide samples doped with cerium. The samples were characterized via powder X Ray Diffraction measurements, Diffuse Reflectance UV Vis spectroscopy, Scanning Electron Microscopy and Transmission Electron Microscopy with EDX (Energy Dispersive X-Ray spectroscopy) analysis, and BET (Brunauer–Emmett–Teller) surface area analysis. XRD measurements reveal the formation of highly crystalline materials; wurtzite is the most important. All materials were tested using phenol as model molecule and their performances were compared with TiO_2 P25. The material showing the best performance, namely Ce-doped ZnO, was then used to abate some emerging pollutants. We chose three iodinated X-ray contrast agent (ICM), iopromide, iopamidol and diatrizoate, known to be recalcitrant to traditional advanced oxidation processes. In the presence of TiO_2 P25, all ICM exhibited a slow degradation, with $t_{1/2}$ ranging from 30 min (iopamidol) to 120 min (diatrizoate) and several hours are required for their complete disappearance. The employment of Ce-doped ZnO leads to a sharp increase in their disappearance, with $t_{1/2}$ obtained within 15 min (iopamidol) or 25 min (diatrizoate) and the complete abatement is achieved within 2 h.

Introduction

Metal oxides semiconductors such as TiO_2, ZnO, WO_3 etc. have been attempted for the photocatalytic degradation of a wide variety of environmental contaminants. Heterogeneous photocatalysis based on nano-structured TiO_2 has been extensively studied as an important destructive technology leading to the total mineralization of a wide range of organic dyes. In some cases, ZnO exhibits a better photocatalytic efficiency than TiO_2, but only few works reported that the photocatalytic activity of ZnO is better than Degussa P25 titania (P25),[1] which has been proved to be one of the most efficient photocatalysts, and widely used as a benchmark. However, both TiO_2 and ZnO are activated only under UV irradiation because of their large band gap (3.2 and 3.4 eV respectively), which greatly limits their application in environmental decontamination as solar spectra only contain 5% of UV. Therefore, it is crucial to explore efficient methods to extend their photocatalytic response from UV to visible region. Previous papers by some of us demonstrated that it is possible, through the dispersion of small amounts of cerium ions within the matrix of different oxides (namely zirconium dioxide or zinc oxide), to modify the photoactivity of the final material. Thereby, the modified oxide becomes photoactive in visible light and much more active in UV light.[2,3] In the case of zinc oxide the cerium does not enter into the structure forming a solid solution due to the deep difference in dimensions of the two metal ions, but segregates as cerium oxide. The interaction between the interfaces of the two oxides is the reason of the increased photocatalytic activity. Doped zinc oxide is a promising candidate as a photocatalytic material since it demonstrates high photocatalytic efficiencies for the degradation of organic pollutants and can be a suitable alternative to TiO_2 thanks to its very similar band gap and to the different morphologies in which it can be prepared.[4,5] Indeed very recently, some papers have been published about Ce-doped ZnO nanostructures used for photocatalytic applications, but in that case the photoactivity was not compared with TiO_2 P25 due to the fact that it was still less efficient.[6]

In a previous paper[3] we prepared pure and doped ZnO with low cerium loading (1% molar) via hydrothermal process, a low temperature, green and simple process to obtain controlled nanostructures, starting from acetate precursor using different Cerium precursors. In the present paper, we prepared materials via the same hydrothermal method, but starting from a different zinc oxide precursor, namely zinc nitrate, that permits to obtain an increased photoactivity. We decided to mantain the low concentration of cerium (1% mol) for using this sample in comparison with the other material we already prepared.[3] The photocatalytic performance of these new materials was firstly tested on phenol and then to more refractory compounds, such as iodinated X ray contrast agents (ICM).

ICM, a class of medical diagnostic agents used for imaging blood vessels and organs, are among the most recalcitrant and highly persistent emerging pollutants.[7] Large quantitiesof ICM are administered to individual patients undergoing tests (>

---

[a] Prof. M. C. Paganini, Dr. D. Dalmasso, Dr. C. Gionco, Dr. V. Polliotto, Dr. L. Mantilleri, Prof. P. Calza
Department of Chemistry
University of Turin
Via P. Giuria 5-10125 Torino-Italy
E-mail: paola.calza@unito.it

Supporting information for this article is available on the WWW under http://dx.doi.org/10.1002/slct.201600645

Un Grazie sincero a…..

.... Elio, il primo non a caso, perché non avrei potuto avere accanto una guida migliore. Ha saputo aiutarmi e condurmi durante tutto il mio percorso con grande sapienza sia in ambito professionalmente che umano. Vivere questo tempo e apprendere affiancata da chi ha così ampia competenza e altrettanta gentilezza, è stato un onore.

.... Johnny, per avermi aiutata, supportata e sopportata durante questi tre bellissimi anni, nella quotidianità fatta di lavoro e di momenti di risate fatte insieme.

.... Cristina e Mario per i consigli e l'aiuto che mi hanno dato ogni qualvolta erano necessari .

.... The research groups of Prof. Pacchioni, in particular Elisa Albanese, Prof. Adriana Zaleska-Medynska and Prof. Zbigniew Sojka for the useful collaborations.

.... Tutti i ragazzi del laboratorio: Erik, Chiara, Arianna, Riccardo, Ida e Cristina per aver reso i giorni degli esperimenti e i pranzi ricchi di allegria.

.... Lo spumeggiante gruppo di dottorandi : Chiara, Marco, Michi, Luca, Ana, Andrea, Giorgia e Cesare che con la loro esuberanza e spensieratezza hanno reso il tempo condiviso di questi tre anni straordinariamente divertenti.

.... Manu e Maggie, amiche da sempre, per esserci sempre state nei momenti difficili.

.... A mia nonna per avermi ospitato al termine delle serate cittadine….

.... E per ultimi ma non certo per importanza, i miei genitori a cui devo un grazie "particolare e infinito" perché mi hanno dato tutto l'aiuto di cui avevo bisogno… sempre.

Grazie a tutti, avete reso questi anni di dottorato un'esperienza unica ed irripetibile, ricca non solo di nozioni, esperienze, capacità e professionalità, ma anche di affetti intensi e indelebili!